NASA

INTERIM REPORT COVERING TASK I,
INVESTIGATION OF ADVANCED REGENERATIVE
THRUST CHAMBER DESIGNS

by

V. R. Stubbs, H. M. Evensen, E. W. Fraczek,
J. A. Cunningham

Prepared for

NATIONAL AERONAUTICS AND SPACE ADMINISTRATION

Contract NAS 3-7971

Aerojet-General Corporation
Materials Advanced Technology Department
Sacramento, California

INTERIM REPORT COVERING TASK I,

INVESTIGATION OF ADVANCED REGENERATIVE

THRUST CHAMBER DESIGNS

by

V.R. Stubbs, H.M. Evensen,

E.W. Fraczek, and J.A. Cunningham

prepared for

NATIONAL AERONAUTICS AND SPACE ADMINISTRATION

August 1967

Technical Management
NASA-Lewis Research Center
Cleveland, Ohio
Liquid Rocket Technology Program

AEROJET-GENERAL CORPORATION
Materials Advanced Technology Dept.
Sacramento, California

8387T

Report NASA CR 72266

PREFACE

This report was prepared by V. R. Stubbs, H. M. Evenson, E. W. Fraczek, and J. A. Cunningham. The work was performed for NASA-LeRC under Contract NAS 3-7971 for Mr. R. A. Duscha, the NASA-LeRC Project Manager.

The authors wish to acknowledge the contributions by M. F. Judkins for the analysis of the compatibility of tungsten with exhaust products; V. E. Kahle for the investigation of chemical vapor deposition of tungsten, W. J. Lewis and R. J. Kotfila for technical review of materials mechanical and thermal properties data.

The report was reviewed and approved by R. E. Anderson, Supervisor, Nozzle Components Sections; and A. V. Levy, Department Manager, Materials Advanced Technology Department.

Report NASA CR 72266

ABSTRACT

A regenerative thrust chamber design is presented which consists of a refractory metal flame liner, a thermal barrier, nickel inner and outer shells, and integral nickel ribs to form the coolant channels. Potential materials, fabrication methods, and processes are analyzed and the selection of chemical vapor deposited tungsten for the flame liner, plasma-arc sprayed tungsten-zirconia composites for the thermal barrier, and electroformed nickel for the structure is justified on the basis of applicability to the design and the potential for future development. Complete stress and heat transfer studies were performed for the design, and a fabrication analysis was made to confirm the producibility of the overall design.

TABLE OF CONTENTS

Report NASA CR 72266

TABLE OF CONTENTS (cont.)

Report NASA CR 72266

TABLE LIST

Report NASA CR 72266

FIGURE LIST

FIGURE LIST (cont.)

FIGURE LIST (cont.)

I. SUMMARY

This is an interim report covering Task I of Contract NAS 3-7971 for
the design and design analysis of a regeneratively cooled fluorine-hydrogen
thrust chamber employing a refractory flame liner, a thermal barrier, and
electroformed nickel channels. Task II of the contract, to follow NASA review
and approval of this report, consists of the fabrication of one thrust
chamber and its shipment to NASA-Lewis Research Center where experimental eval-
uation will be conducted.

The various technologies used in the thrust chamber design discussed in
this report constitute a new approach to regeneratively cooled chambers. All
the technologies have advanced beyond the laboratory stage but are relatively
new and probably the first integration of these technologies into one unique
design that has the potential of reducing regeneratively cooled thrust chamber
fabrication cost and of reducing the heat flux to the coolant and increasing
chamber life.

The basic elements of this thrust chamber are a flame liner of vapor-
deposited tungsten reinforced with tungsten wire screen, a thermal barrier of
a gradated coating of plasma-arc-sprayed tungsten-zirconia composites, and a
chamber shell of electroformed nickel with integrally formed cooling channels.
Stainless steel coolant inlet and outlet manifolds and attachment flanges are
utilized, and an ablative nozzle extension with a carbon phenolic flame liner
(from an area ratio of 16:1 to 60:1) completes the thrust chamber design.

A complete thermal design study was conducted to establish the channel
size required to maintain coolant velocities at values necessary to maintain
the nickel temperatures at 1400°F maximum and the flame liner at 4600°F maximum.
The thermal resistance of the thermal barrier is 425 $in.^2$-sec-°F/Btu in the
chamber and throat, gradually increasing to 1000 $in.^2$-sec-°F/Btu at an area
ratio of 6 to 1 and 1000 to the exit at area ratio 16 to 1. The engine design

I, Summary (cont.)

and operating parameters can all be met with the exception of the 125 psi pressure drop. It is estimated that the pressure drop will be 213 psi at 760 psia inlet pressure without recovery of the coolant velocity head loss. The complete analysis indicates that the fabrication approach is feasible and the design has sufficient potential for success to justify proceeding with fabrication and testing.

II. INTRODUCTION

Regeneratively cooled thrust chambers usually consist of a bundle of tapered, contoured tubes or channels that are furnace brazed together to form a pressure-tight assembly. This fabrication method requires that a large number of tubes or channels (e.g., 180 tubes in the RL10 engine) must be tapered to provide an exact cross-sectional area at each axial station, and they must be bent to form the correct contour and inside diameter of the chamber, throat, and nozzle. This fabrication method involves tedious, expensive, and time-consuming techniques such as die forming, hand assembly of tubes, and furnace brazing. After the thrust chamber has been brazed, it is often not pressure tight, which is not surprising considering the large number of braze joints, and it must be repaired by hand brazing. Because of the expensive and slow fabrication process, once the thrust chamber design has been fixed, it cannot readily be changed to accommodate new innovations or changes of nozzle contour, nozzle area ratio, or propellants.

Regeneratively cooled thrust chambers have performed well with relatively low thrust/low energy propellants. Tube materials used have an upper temperature limit of about 1700°F and most systems have utilized film cooling to maintain that maximum. Thrust chambers using high energy propellants such as LF_2/LH_2 would require excessive film cooling to maintain reasonable gas-side temperatures unless a means is provided to protect the chamber wall from the very high temperature gases.

Many successes have been evident in applying thermal barriers to regeneratively cooled engines of conventional tube bundle design (notably the X-15) for controlling the gas-side temperature and decreasing the heat flux to the coolant. Researchers have indicated that a combination of heat-resistant coatings with yet untested substitutes for the tube bundle may have great potential of containing the propellant exhaust gases, reducing the heat flux to the coolant and competing in cost with the brazed tube bundle. Of perhaps

II, Introduction (cont.)

prime importance in present mission requirements is multiple-start capability and relatively unlimited life without deterioration of thrust level or efficiency.

The objective of this program was to investigate new fabrication methods and design techniques with the potential for reducing fabrication time or cost, reducing the heat flux to the coolant, and increasing thrust chamber life. The scope of Task I includes design of a thrust chamber, complete heat transfer analysis, stress analysis and fabrication analysis, and submission of the design report to NASA/LeRC. Task II of the program covers completion of detail design and fabrication and thermal shock testing of a thrust chamber.

The subject matter of the report to follow will be divided into five sections, with headings descriptive of the engineering disciplines involved and a concluding section. The Design Analysis Section will integrate the preceding analyses and present the selected thrust chamber design.

The information concerning electroforming of nickel was furnished by Mr. S. Fialkoff and Dr. S. S. Hammer of Camin Laboratories, Inc., Brooklyn, N.Y., who were consultants for Task I of the program. Camin Laboratories will fabricate the channels and structure during Task II of the program.

III.   TASK I--DESIGN AND ANALYSIS

    A.   MATERIAL AND PROCESS SELECTION

        1.   Flame Liner

            a.   Material Selection

                Tungsten was selected for the flame liner material on the basis of its high melting point and its compatibility with high-temperature fluorine propellant combustion species. Batchelor (Reference 1) has reported the investigation of high-temperature, solid-gas reactions of tungsten, tantalum, and the alloy Ta-10W in two series of tests with fluorine-containing atmospheres. In the first test, atmospheres consisted of the individual gases HF, HCl, CO_2, and H_2O and mixtures of H_2/H_2O and CO/CO_2. In the second test, the atmosphere was the combustion products from a fluorocarbon propellant and included HF, $AlF_{1,2}$, and $_3$, CO, H_2, HCl, H_2, H_2O, and CO_2 gaseous species. The results of these tests that are significant to this program are as follows:

                (1)   Tungsten is essentially unaffected up to its melting point by HF and HCl.

                (2)   Tantalum is attacked by HCl and HF.

                (3)   The Ta-10W alloy had reaction characteristics similar to tantalum, but to a lesser extent.

                Thermodynamic calculations have been made to support the above conclusions which indicate that W will not react with HF at 3000°F, 4000°F, and 5000°F. However, tungsten will react with the gas species F. The thrust chamber being designed in this program is for an LF_2/LH_2 mixture ratio (MR) of 12. However, the exhaust gas in the combustion chamber may possibly contain additional fluorine due to poor mixing or injector streaking. To predict tungsten corrosion rates in the presence of a HF, F, H, and H_2 exhaust

III, A, Material and Process Selection (cont.)

gas, calculations of the oxidizing potential of the exhaust gases have been made and compared with empirical data on tungsten oxidation. To compare poor mixing conditons, MR's of 12, 15 and 19 were utilized at a temperature range of 4000 to 5000°F at 400 psi chamber pressure. The only gas composition data available for the expected condition where the chamber temperature was 97.85% of the theoretical combustion flame temperature, were for a mixture ratio of 12. Accordingly, fractions of H_2, H, HF, and F were obtained by plotting corresponding values of these species for adiabatic TC's stagnation temperature at MRs of 12 to 20, sketching the parallel curves for 97.85 (TC Frozen at Area Ratio 1.3) and estimating the mole fractions at mixture ratios of 15 and 19. The curves appear in Figures 1, 2, 3, and 4 and the values are shown in Table I.
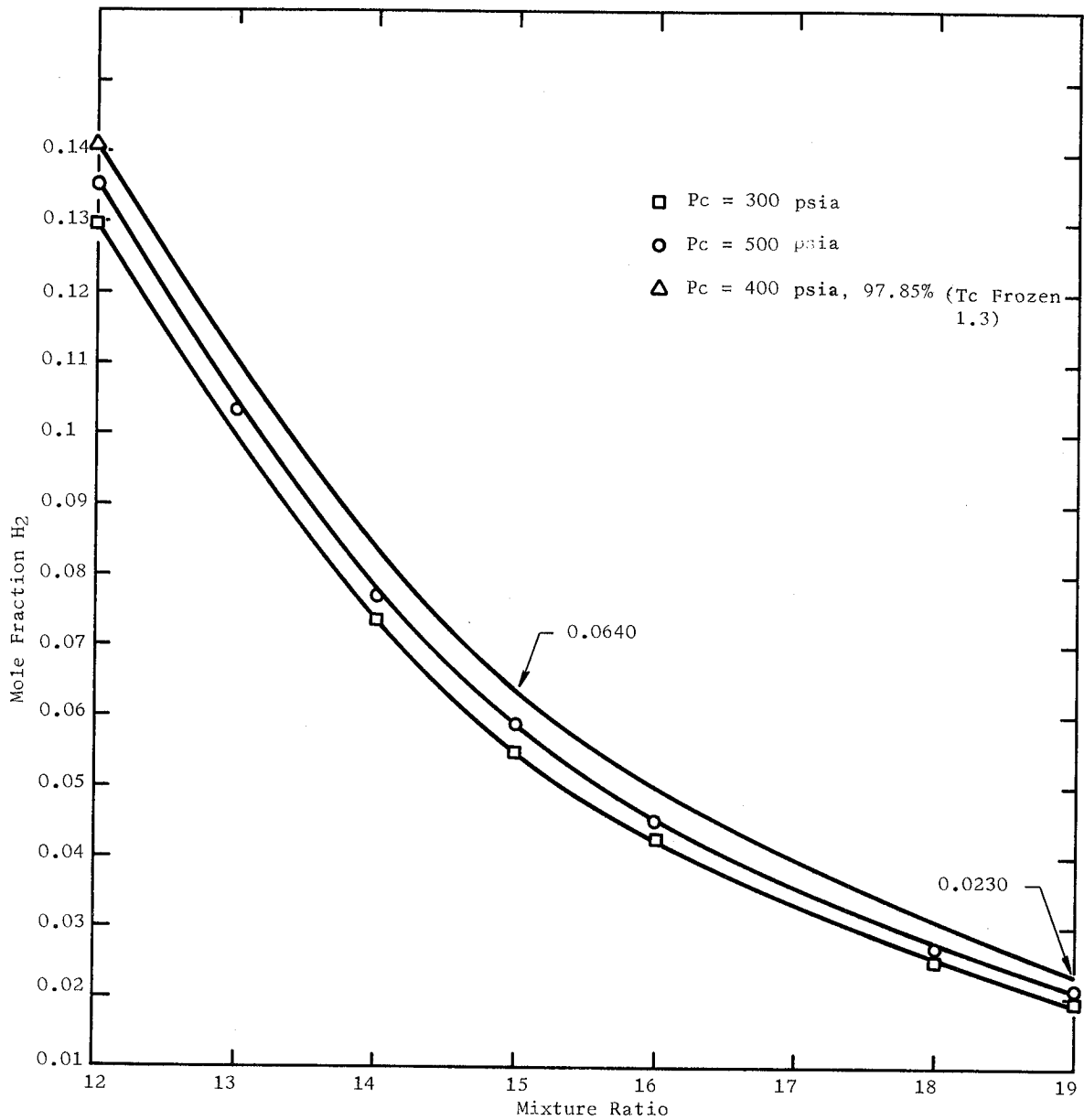
Figure 1. Mole Fraction H_2 vs Mixture Ratio
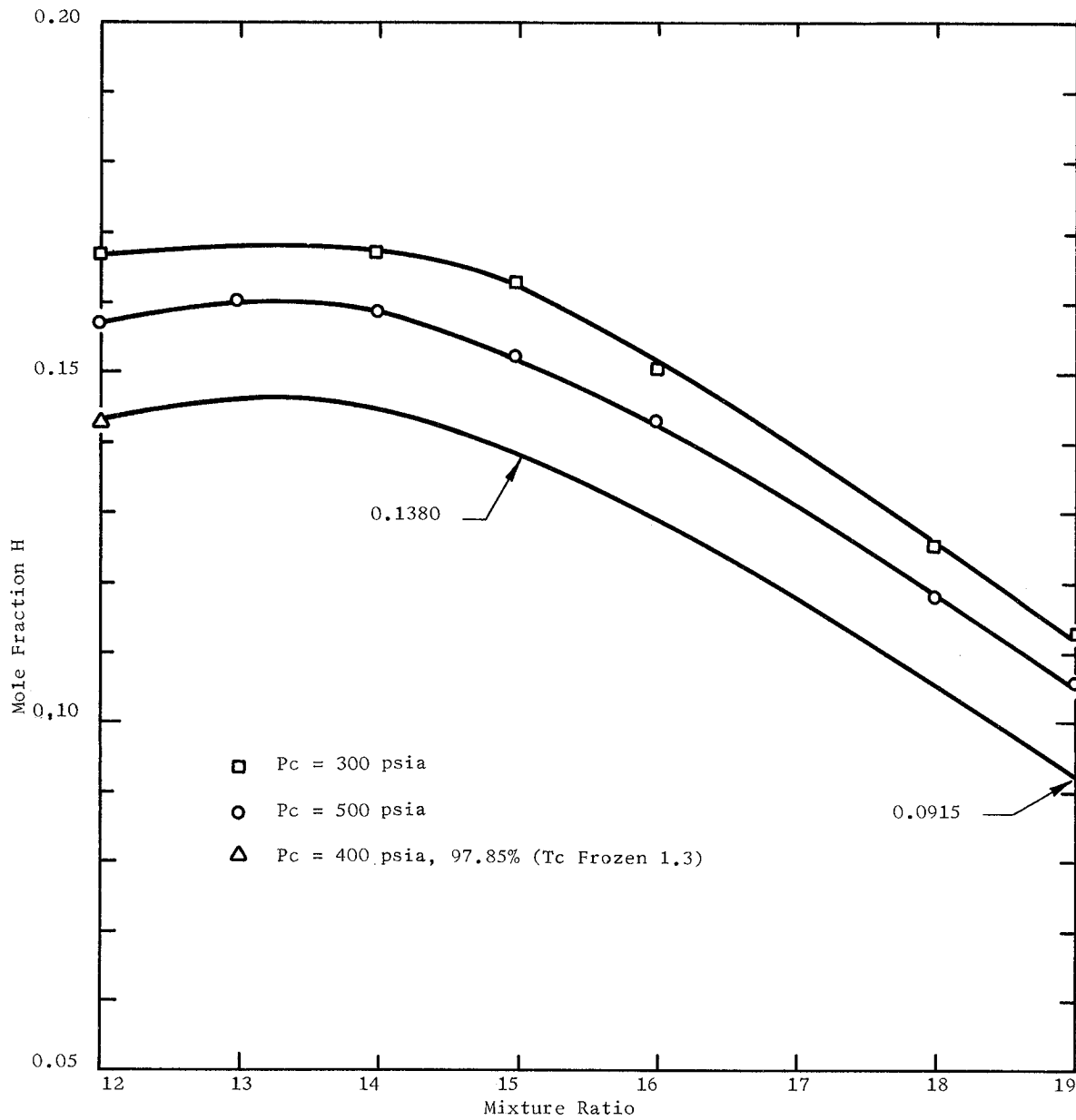
Figure 2. Mole Fraction H vs Mixture Ratio
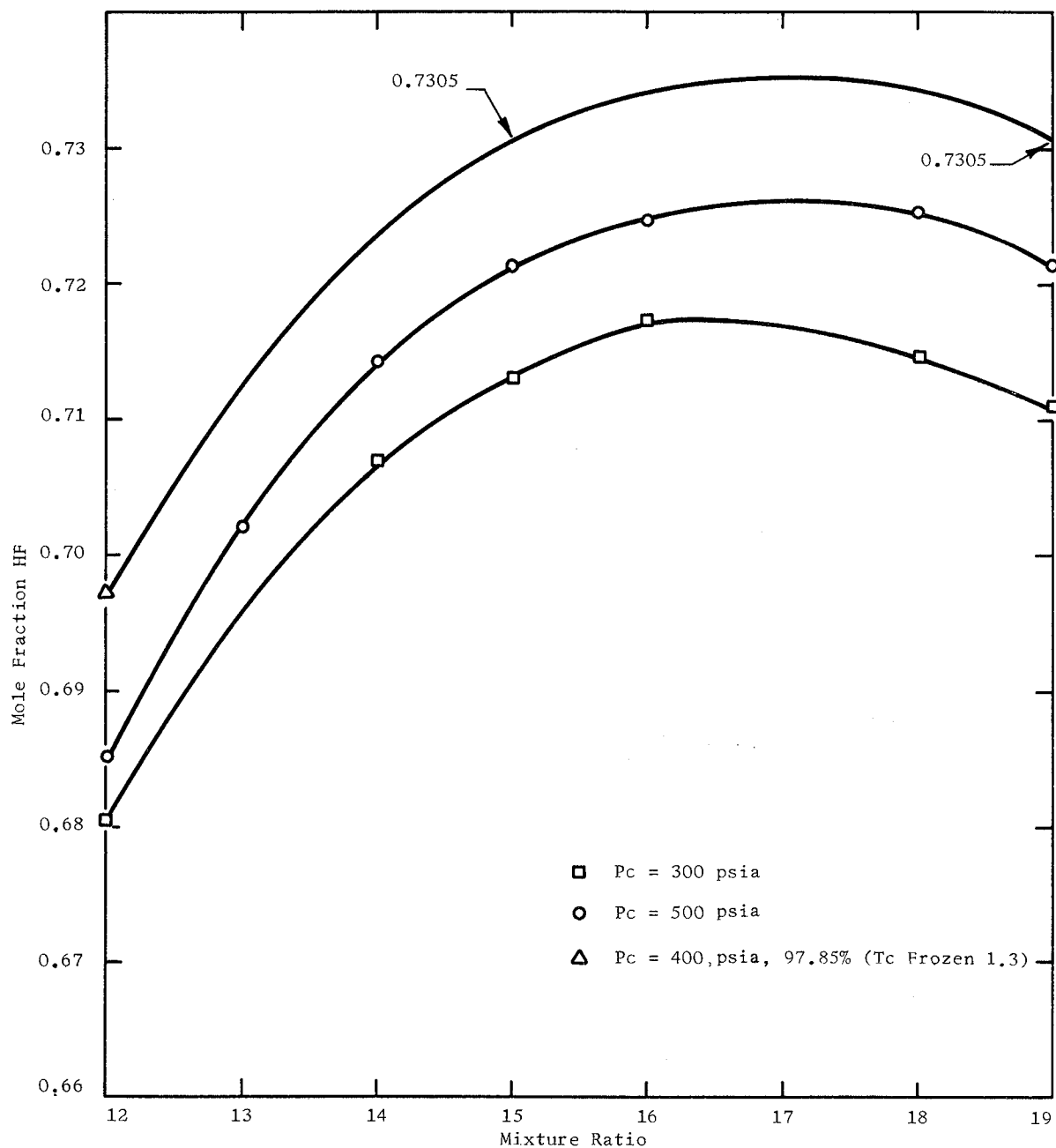
Figure 3.   Mole Fraction HF vs Mixture Ratio
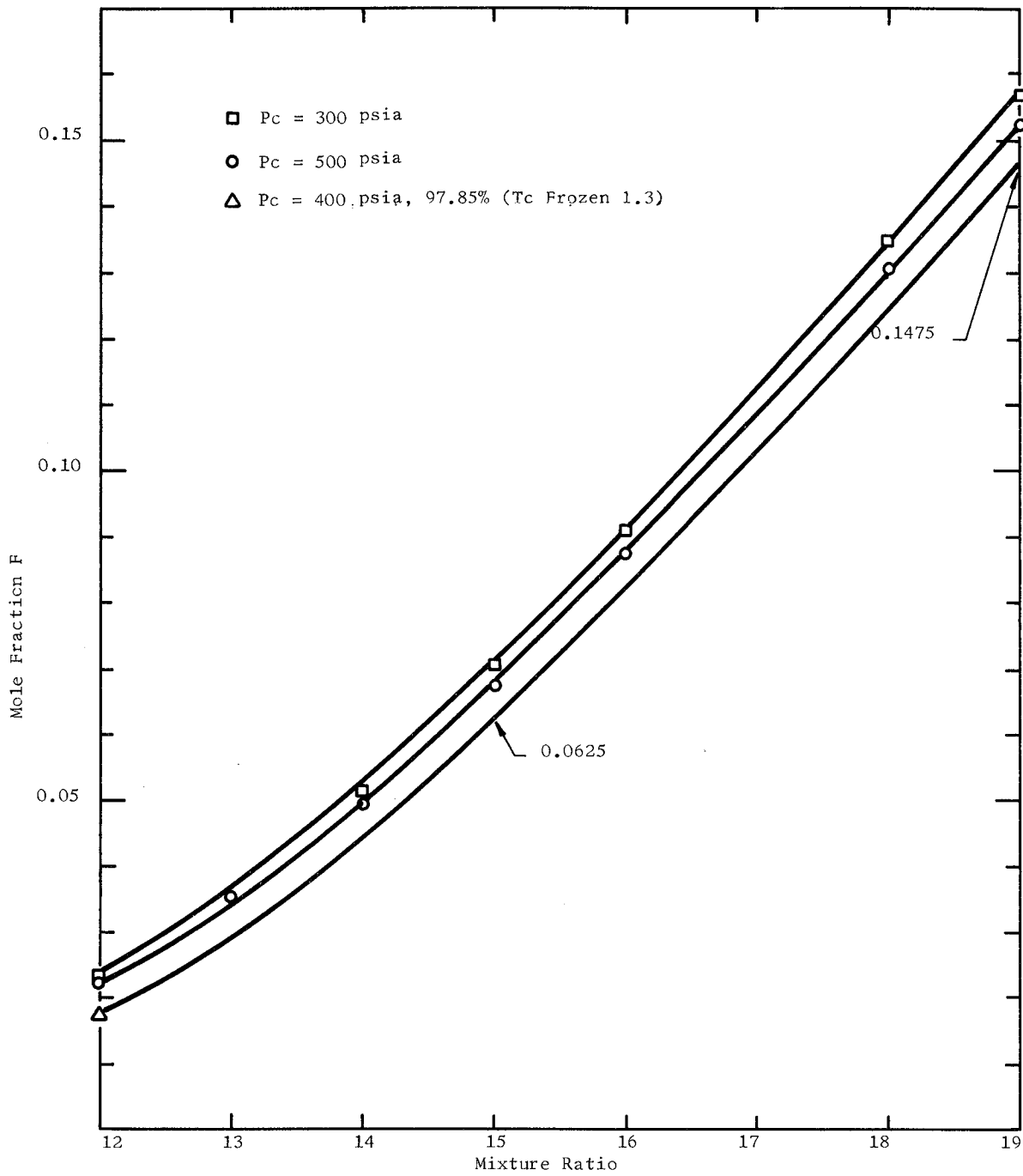
Figure 4. Mole Fraction F vs Mixture Ratio

TABLE I

LF_2/LH_2 EXHAUST GAS COMPOSITION

PC = 400 psia; 97.85% (TC Frozen 1.3)
7654°R

	MR = 12	MR = 15	MR = 19
H_2	0.1413	0.0640	0.0230
H	0.1434	0.1380	0.0915
HF	0.6973	0.7305	0.7305
F	0.0180	0.0625	0.1475

III, A, Material and Process Selection (cont.)

The thermodynamic favorabilities of possible reactions of exhaust gas species with tungsten were determined by means of the JANAF Thermochemical Tables (PB 168370). A reaction is considered probable if the free energy (ΔF, driving force) for the reaction is appreciably negative at the stated temperatures and pressures.

$$\Delta F \text{ reaction } = \Delta F \text{ products } = \Delta F \text{ reactants}$$

At 4400°F (2700°K) the possible reaction between W and the exhaust gas specie, both at one atmosphere pressure and at 400 psia, is indicated by the free energies below:

$$6 \text{ HF} + \text{W} \longrightarrow \text{WF}_6 + 3\text{H}_2 \quad ; \quad \Delta F, 4400°F, 14.7 \text{ psi} = + 165.453$$
$$\Delta F, 4941°F, 400 \text{ psi} = + 153.446$$

$$\text{W} + 6\text{F} \longrightarrow \text{WF}_6 \quad ; \quad \Delta F, 4400°F, 14.7 \text{ psi} = -107.541$$
$$\Delta F, 4400°F, 400 \text{ psi} = -137.56$$
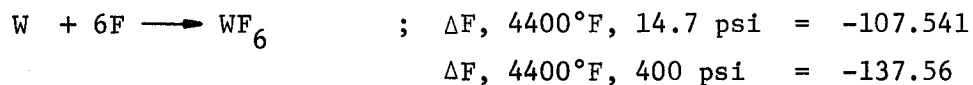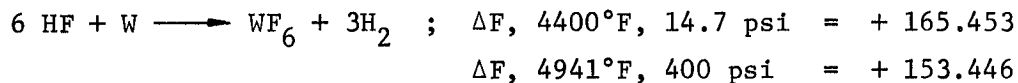
III, A, Material and Process Selection (cont.)

Thus, the only gas specie in the propellant exhaust gas composition of an LF_2/LH_2 propellant which is corrosive to tungsten is predicted to be elemental fluorine (F). From Table I, the mole fraction of F in the worst case, a mixture ratio of 19, is 0.1475.

Although tungsten regression rates with fluorinated propellants have not been measured by actual test firings, it is believed that the reaction of elemental fluorine with tungsten will be similar to that of oxygen with tungsten. Assuming that fluorine will behave (toward tungsten) in an LF_2/LH_2 motor in an analogous fashion to the oxygenic species in solid propellant exhaust gases, the fluorine oxidant value is obtained by ln (1 + 0.1475) = 0.1376. The use of oxidant value to predict regression was developed empirically under other programs.

The measured regression rates of tungsten with designated solid propellants are plotted in Figure 5 versus the oxidant value of the propellant exhaust gas which is the natural logarithm (ln) of the quantity 1 plus the mole fraction of gas specie corrosive to tungsten. It is then clear from Figure 5 that even at a mixture ratio of 19, there should be negligible tungsten regression, since an oxidant value of about 0.16 corresponds to zero regression rate.

b. Process Selection

Chemical vapor deposition was selected as the process that offered the strongest liner and the greatest potential for success at a reasonable cost. Processes that were considered for production of a pure tungsten flame liner are as follows:

(1) Chemical Vapor Deposition
(2) Plasma Arc Deposition
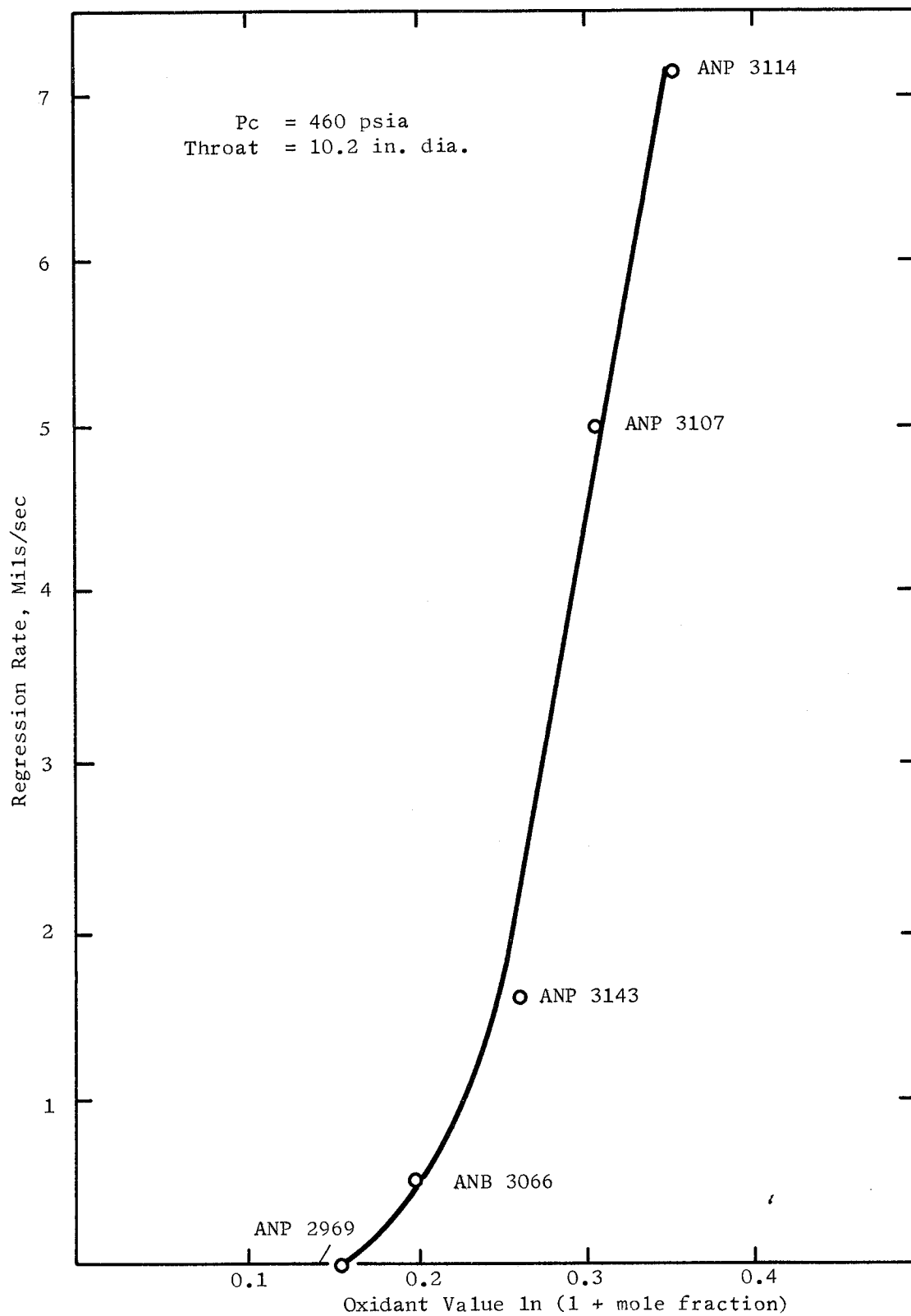
Figure 5. Regression Rate vs Concentration Driving Force
for Tungsten Scaled to 10.2-in.-Diameter Throat,
460 psia Pc

III, A, Material and Process Selection (cont.)

(3) Forming and Welding of Wrought Tungsten

(4) Electrodeposition

(5) Electrophoresis and Slurry

The advantages and disadvantages of each method are discussed below:

(1) Chemical Vapor Deposition

The chemical vapor-deposited (pyrolytic) tungsten process was selected for fabricating the flame barrier because of the deposit's high density and mechanical properties. Since the density of pyrolytic tungsten (99% of theoretical) is higher than that of plasma-arc-sprayed tungsten (83 to 90% of theoretical) the erosion resistance is expected to be better. In addition, pyrolytic tungsten will form a good bond with the tungsten screen reinforcement as shown in Figure 6 and deposit behind and between the wires in the screen without leaving voids. Therefore, it is possible to apply a dense coating which will take advantage of the superior shock resistance of reinforced tungsten.

A disadvantage of the process is that it requires very accurate control of the variables. Obtaining an even coating over a large area can be difficult unless a uniform substrate temperature can be maintained. It is not possible to stop the process before the total thickness is deposited for the purpose of checking thickness. An oxide coating forms on exposure to air and would result in a laminated structure with a weak bond unless the oxide were removed. This can be done by heating in hydrogen to 1850°F for 10 minutes, but is not feasible when graphite is the substrate due to the mismatch of thermal expansion. Thermocouples are located at intervals along the mandrel permitting a continuous temperature check; however, it is usually necessary to make a trial run to determine whether the temperature distribution, as indicated by the thermocouples, results in a uniform thickness
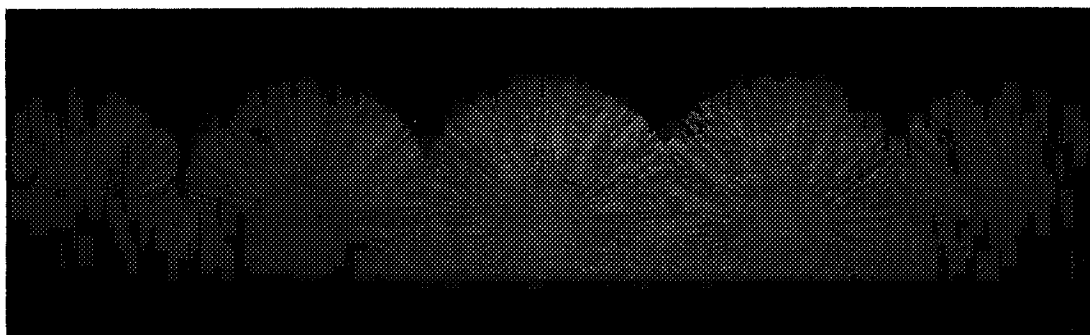
Mag: 15X   Etchant: Murakami's

Figure 6.   Chemical Vapor Deposited Tungsten on 0.030-in.-dia
            Tungsten Wire

III, A, Material and Process Selection (cont.)

of deposit and whether the total run time is adequate to obtain a coating thickness within tolerance. Extreme care must be taken to maintain a minimum temperature differential between the tungsten and the graphite mandrel on cooldown to prevent excessive tensile loading on the tungsten, resulting in cracks. The cooldown period may be as long as 24 hours.

The mechanical properties of tungsten screen reinforced pyrolytic tungsten, pyrolytic tungsten without screen, and Grade A plasma-arc sprayed tungsten without screen are listed in Table II. Testing was performed at room temperature. The testing procedure is described in Ordnance Specification OS 106820 Notice 1. The tensile properties of pyrolytic tungsten at temperatures to 4500°F are shown in Figure 7.

TABLE II

MECHANICAL PROPERTIES OF PYROLYTIC TUNGSTEN
AND GRADE A PLASMA-ARC SPRAYED TUNGSTEN

| | Pyrolytic | | Grade A Plasma-Arc Sprayed Tungsten |
	No Screen	1 layer of 30-Mesh Screen	
Tensile Strength, psi	20,000	20,000	16,900
Flexural Strength, psi	93,600	54,300	30,100
Micro-Impact Properties	45.9	88.9	49.1

The reinforced tungsten specimens contained one layer of 30-mesh screen, which provided wires oriented in the longitudinal direction whose cross-sections were only 1% of the total cross-sectional area. Although the flexural strength of the reinforced samples were lower than that of the non-reinforced pyrolytic tungsten, the reinforced samples did not fail completely but developed a crack on the tensile side only. The samples without screen and the plasma-arc sprayed samples failed completely. The toughness
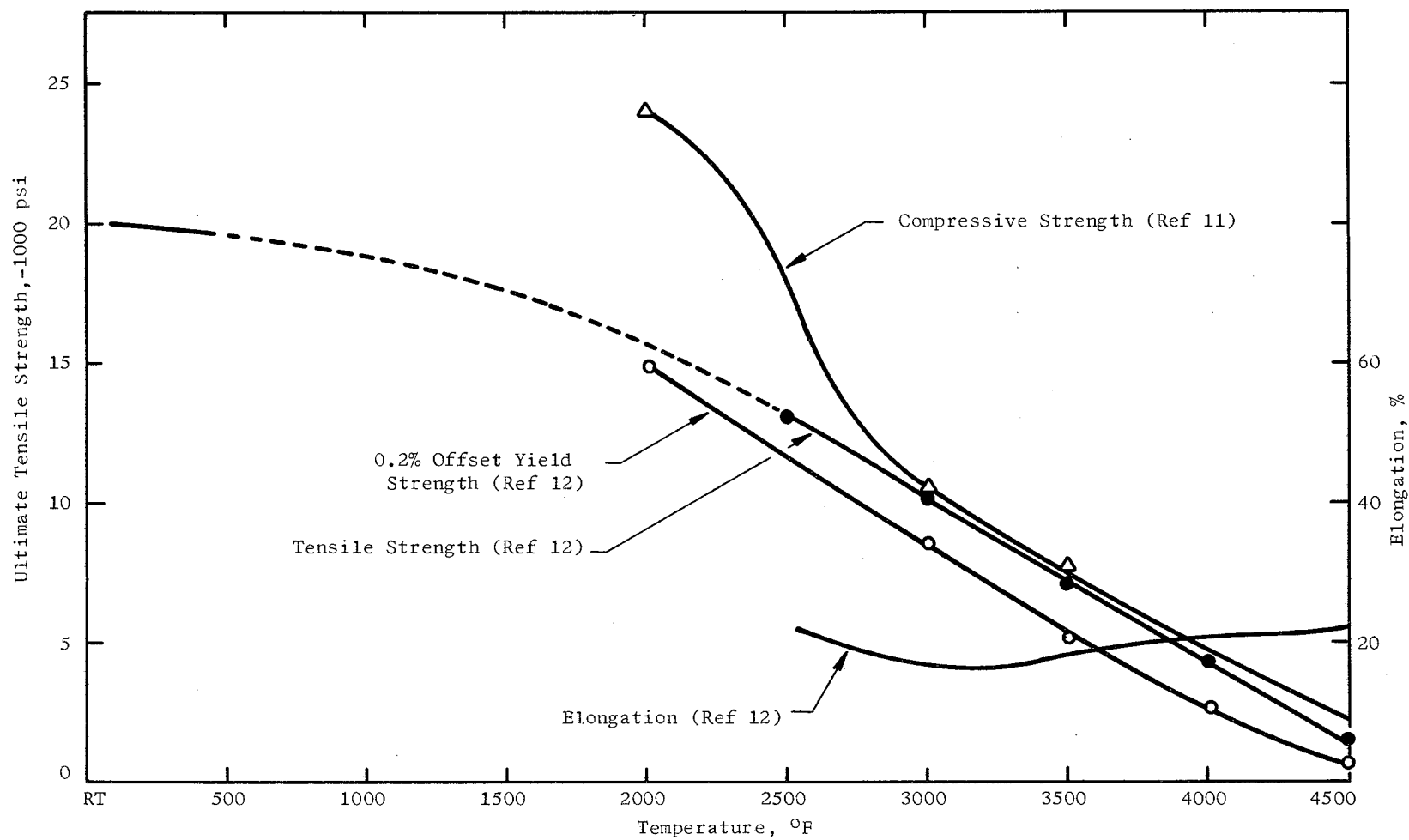
Figure 7. Tensile Properties of Pyrolytic Tungsten

III, A, Material and Process Selection (cont.)

imparted by the screen was also demonstrated by an impact strength of nearly
double the non-reinforced tungsten and plasma-arc sprayed tungsten. The
phenomenon of the reinforced specimen having a lower modulus of rupture than
the non-reinforced material has been observed in other reinforced materials[2].
The following table, extracted from Reference 2, illustrates how the modulus
of the rupture changes with volume percent reinforcing fiber.

TABLE III

ALUMINA-MOLYBDENUM FIBER COMPOSITES

Vol% Fiber	Modulus of Rupture Prior to Thermal Shock (psi)	Modulus of Rupture Following 4 Thermal Shocks (psi)
None	34,300	0
4.2	9,750	9,750
10	12,300	18,100
20	22,900	22,000

In this case, the lower modulus of rupture prior
to thermal shock was attributed to microcracks introduced in the composite by
the fibers. Despite the presence of the microcracks, the postthermal shock
modulus of rupture of the composite was superior to that of the sample with
no fibers.

Another extremely important advantage of incorporating
screen in the vapor deposited tungsten flame liner is that the screen pattern
will reproduce almost without regard to thickness of tungsten deposited, and
will present a grid that will greatly improve the adherence of the plasma-
sprayed tungsten-zirconia to follow. The bond of plasma-sprayed materials to
most substrates is mechanical and relatively weak but improves in proportion

III, A, Material and Process Selection (cont.)

to the roughness and cleanliness of the surface. Previous attempts to roughen a tungsten surface with coarse silicon carbide grit blasting have resulted in a tendency to polish rather than roughen.

Both pure tungsten and tungsten-rhenium alloys were considered for screen reinforcement materials. The ductility of both materials is adequate before recrystallization; however, after recrystallization, the room temperature ductility decreases drastically. Rhenium is added to pure tungsten to inhibit recrystallization and grain growth and, therefore, improve the ductility after a heating cycle. However, over 3000°F, tungsten-rhenium alloys recrystallize and grain growth begins, reducing the room temperature ductility to that of the pure tungsten.

Because the operating temperature of the chamber flame liner will be over 4000°F, both the pure tungsten and the tungsten-rhenium alloy screens will be nearly 100 percent recrystallized after the first firing, and, therefore, will exhibit little difference in ductility or thermal shock resistance. Considering this, it was decided that the additional cost of the tungsten-rhenium wire screen was not justified, and unalloyed tungsten-wire screen will be used.

The screen selected is 0.007 in. x 30 mesh. Parameters for screen size selection are ease of wrapping and fitting to the substrate which requires flexibility, and an opening size permitting complete coverage of the underside of the screen with pyrolytic tungsten before bridging across the opening occurs. The open weave is desirable as noted above, to provide a definite grid for plasma spraying adhesion.

III, A, Material and Process Selection (cont.)

(2) Plasma-Arc Deposition

Aerojet has many years experience in plasma-arc spraying of tungsten, both on regenerative tube thrust chambers and in solid rocket nozzle exit cones and throat inserts where the substrate is graphite. Equipment and controls are available to deposit tungsten to close tolerances. The deposit is approximately 85% dense and does not compare favorably to wrought or vapor-deposited tungsten on the basis of strength. Test results have indicated that a considerable increase in the impact strength of vapor-deposited tungsten can be gained with wire-reinforced tungsten. To make a direct comparison of plasma-sprayed tungsten to vapor-deposited tungsten, with and without screen reinforcement, a 3.0-in.-dia graphite specimen was coated by spraying with approximately 0.010 in. of tungsten. During spraying, it was noted that the deposit builds up as much as 0.020 in. before bridging over to form a continuous coating between wires. Also, voids form under the wires as shown in Figure 8 because the plasma-arc deposits in a line-of-sight manner. A conclusion is that, while tungsten spraying of a tungsten liner on the proposed graphite substrate is a relatively easy task, reinforcement of sprayed tungsten with screen is not practical. Comparisons of plasma-sprayed tungsten physical properties with vapor-deposited tungsten are made in Table II. In case of a major failure in the vapor deposition approach, plasma-arc spraying is the backup method.

(3) Forming and Welding of Wrought Tungsten

Fabrication by conventional forming methods using wrought tungsten sheet would produce a free-standing structure with good strength characteristics. However, both longitudinal and circumferential weld joints would be required and this would make the diametrical and longitudinal contour tolerance difficult to maintain. Shear spinning would eliminate the longitudinal welds; however, circumferential joints would still be required as the size of the thrust chamber exceeds the present capability for fabrication
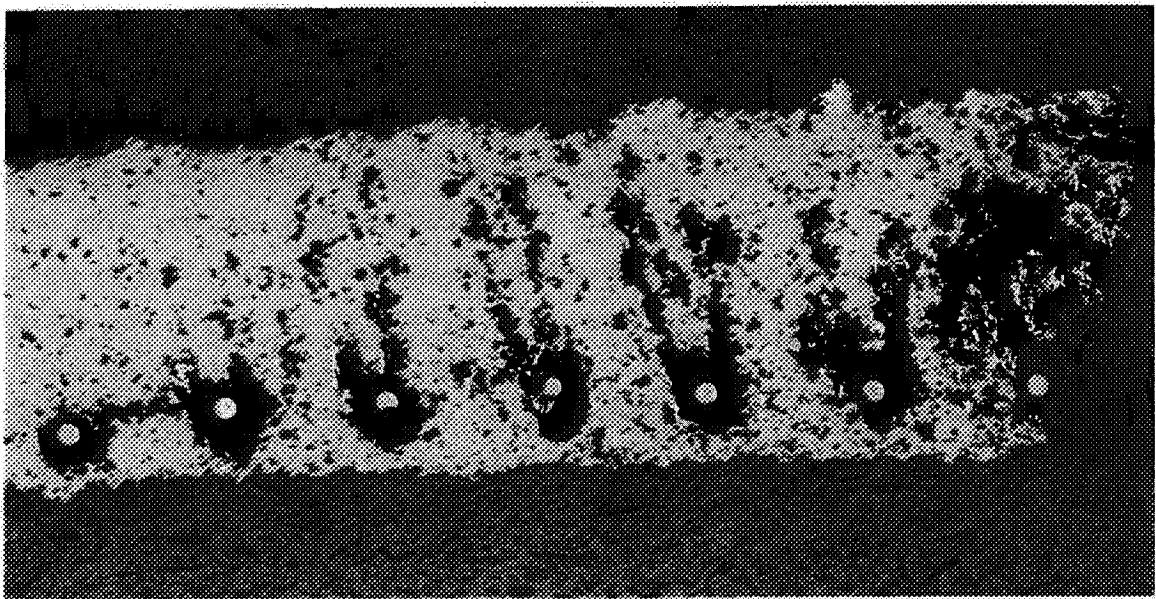
Mag: 15X   Etchant: None

Figure 8. Plasma Arc Sprayed Tungsten Over Tungsten Screen

III, A, Material and Process Selection (cont.)

of tungsten plate preforms for shear spinning. Tooling costs would be high for both the forming and shear spinning methods.

(4) Electrodeposition

Electrodeposition or electroforming of tungsten and other refractories has been performed by Union Carbide Corporation, and they reported obtaining theoretical dense deposits of a columnar grain microstructure. Union Carbide representatives have the general opinion that the process is applicable to the thrust chamber being designed, but present production capacity is limited to components 14.0-in.-dia by 23.0-in.-long. Though the method appeared promising, its investigation was discontinued because of the size limitations.

(5) Electrophoresis and Slurry Methods

Electrophoresis of tungsten has been accomplished on a laboratory scale, but there is no indication in the literature of its application to large-size components. This method consists of suspending particles in an organic dielectric solvent and impressing a current of 50 to 500 v between two electrodes to effect a deposit on the substrate. Such deposits are made up of individual particles loosely bound to each other. A series of postdeposit treatments is required to obtain a dense, well-bonded coating. This is usually accomplished by sintering at 3500°F or above, but with an activated sintering process, sintering at 2200°F may be possible. Temperatures of this magnitude, when applied to a graphite mandrel, would probably cause separation and cracking of the tungsten on cooldown due to unequal thermal expansion. This same problem of relative thermal expansion during sintering was foreseen with slurry coating methods and, therefore, they were eliminated from further considerations.

III, A, Material and Process Selection (cont.)

2.   Thermal Barrier

a.   Material Selection

The selection of a tungsten-zirconia combination as the
thermal barrier material was based on excellent results obtained with this
material on other regeneratively cooled thrust chambers in the Titan and ARES
programs. Molybdenum-zirconia combinations being tested on a current program,
NASA 3-7955, also show considerable promise as shock-resistant thermal barriers.

The properties of plasma-arc sprayed tungsten and plasma-
arc sprayed molybdenum that are significant in thermal barrier calculations
are:

Material	Melting Point	Density, lb/in.^{3}	Thermal Conductivity Btu/hr/ft/°F at 3300°F	Thermal Expansion RT to 3300°F
W	6170	0.593	59	0.93
Mo	4760	0.314	56	1.24

These data indicate that coating thickness to obtain the
same thermal resistance at 3300°F would be approximately the same for molybdenum
or tungsten. However, in tests in which tungsten-zirconia and molybdenum-
zirconia composites were evaluated, the tungsten-based mixture had somewhat
lower thermal conductivity.

Composition	Coating Surface, Temp, °F	Thickness, mils	Thermal Resistance, in.^{2}-sec-°F/ Btu	Thermal Conductivity, Btu/hr/ft/ °F
52% ZrO_2/48% W	3950	78	1310	2.47
51% ZrO_2/49% Mo	4250	106	1500	2.94

III, A, Material and Process Selection (cont.)

A chamber coated with Mo/CrO_2 composite compared to W/ZrO_2 composite would weigh less in proportion to the densities of Mo and W. Some difference in gradation might be required to gradate thermal expansions.

The wall temperature of the thermal barrier coating on the gas side will be 4270°F in the chamber area. Data is not available for the tensile strength of plasma-arc sprayed Mo; however, unalloyed pressed and sintered molybdenum has a tensile strength of 2200 psi[4], which is nearly identical with plasma-sprayed tungsten. The strength of plasma-sprayed molybdenum can be expected to be less than pressed and sintered molybdenum due to porosity inherent in sprayed coatings. While use of molybdenum would bring a weight advantage, lack of complete data for strength at temperature and the more extensive experience gained with tungsten-zirconia coatings favor tungsten-zirconia for the chamber at this time.

b.   Physical Properties

The mechanical properties of various tungsten-zirconia combinations at temperatures above 3000°F are assumed to be similar to that of unalloyed plasma-sprayed tungsten, as shown in Figure 9. The thermal resistance of various tungsten-zirconia combinations is shown in Figure 10. These data developed by Aerojet under other programs[5], indicate that the thermal conductivity coefficients obtained by testing are lower than would be expected by adding the separate conductivity coefficients of the constituents on a volume basis. The reason for the lower conductivity is that the ceramic phase is in the form of platelets perpendicular to the heat flow path. A sprayed mixture of 85% tungsten-15% zirconia (weight percent) 0.072-in.-thick has a thermal resistance of 500 $in.^2$-sec-°F/Btu, which is equivalent either to 0.690 in. of pure wrought tungsten, 0.165 in. of sprayed tungsten, or 0.016 in. of zirconia.
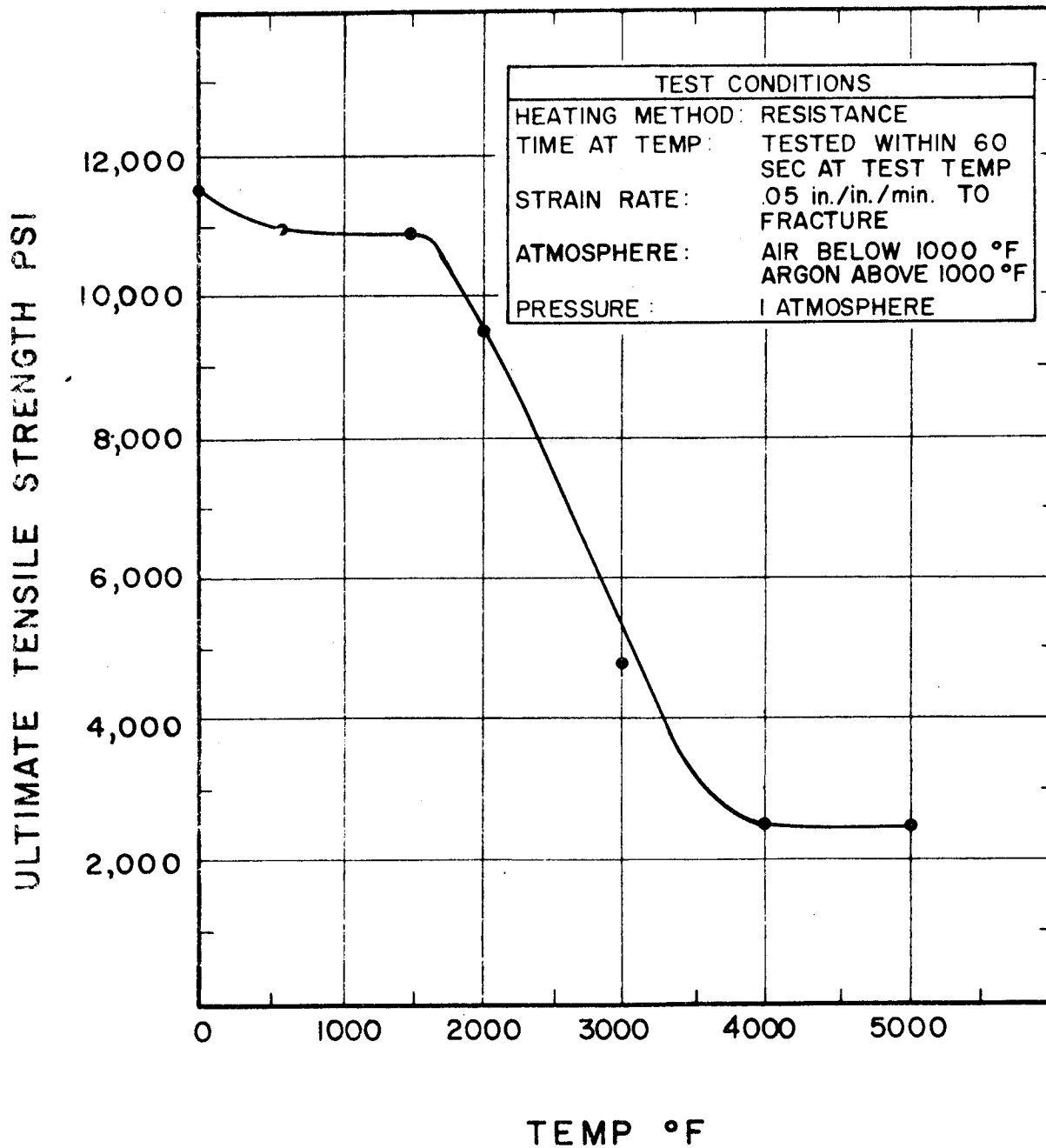
Figure 9. Ultimate Tensile Strength of Grade A Plasma Arc
Sprayed Tungsten (4)
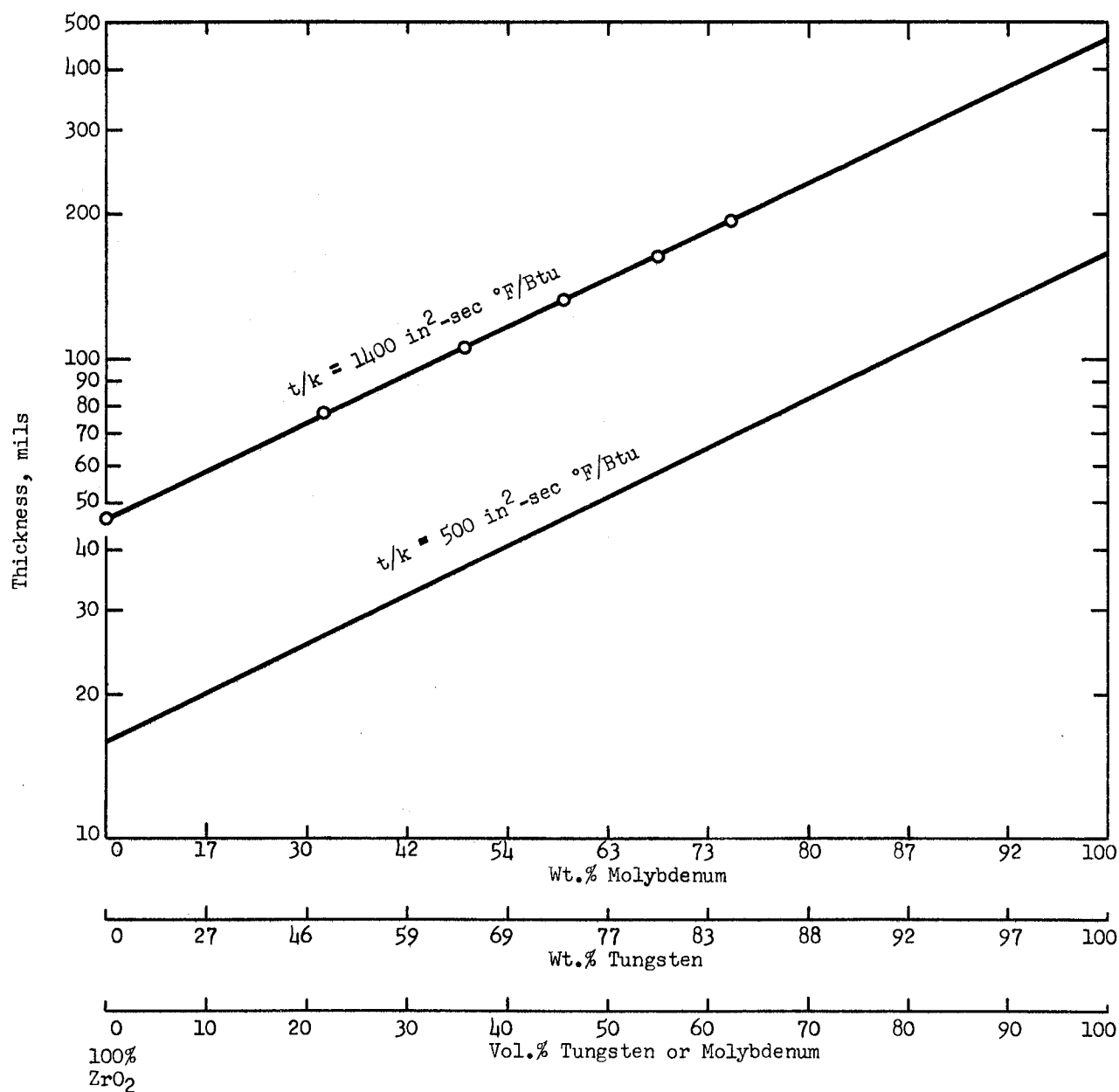
Figure 10. Thermal Resistance of Tungsten-Zirconium Composites as
a Function of Coating Thickness

III, A, Material and Process Selection (cont.)

c. Thermal Expansion

To reduce the stresses at the liner to thermal barrier interface and the thermal barrier to nickel interface due to thermal expansion, the temperature of each layer must be controlled to effect a favorable match of total expansion at the interfaces. Tungsten-zirconia mixtures are reasonably well suited to this purpose. The thermal expansion of the materials involved are shown in Figure 11. The process of gradating the coatings to reduce relative thermal expansion and the resultant stresses is discussed in the Design Section of this report.

d. Process Selection

Plasma-arc spraying was selected as the method for applying the thermal barrier material. Other methods surveyed were vapor deposition, electrophoresis, and slurry. Vapor deposition was not considered because of the high density, high conductivity coating attained. Electrophoresis methods were not considered practical for applying the thermal barrier for the same reason they were eliminated as methods for producing the flame liner. Oxyacetylene spraying is not used because of superior bond strength available in plasma-sprayed coatings.

3. Channels and Structure

a. Process Selection

The selection of electroforming as the process for fabrication of the channels and structure is a key factor in the basic design concept and fabrication approach. The primary advantages of electroforming to form coolant channels, over channels made from shells and spacers and over the conventional brazed tube bundle designs, are: (1) the elimination of
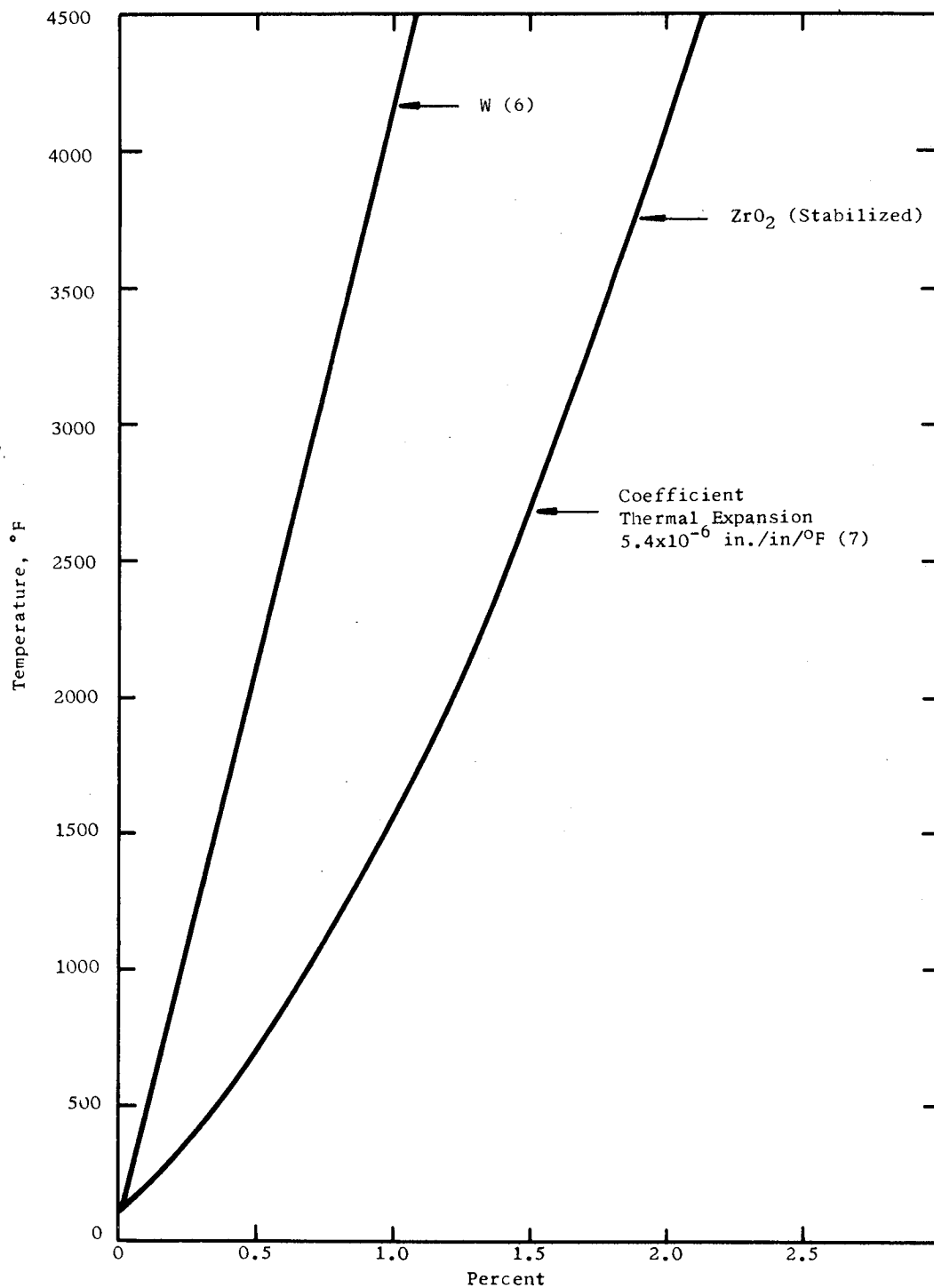
Figure 11.   Percent Thermal Expansion From RT Pressed and Sintered
Tungsten 83.6% Dense, and Stabilized Zirconia

III, A, Material and Process Selection (cont.)

welding or brazing and the costly forming, fitup and distortion problems inher-
ent in these designs; (2) the flexibility in regard to design changes without
tooling changes; and (3) the substitution in effect of machined surfaces and
the closer tolerances obtainable for formed surfaces and forming tolerances.

b.   Material Selection

Pure nickel, stainless steel, hastelloy, and a few other
high-nickel alloy materials are those normally utilized in regenerative-cooled
thrust chambers. Pure nickel was selected for this program not because of
its superiority over the other candidates, but because electroforming was
selected as the fabrication approach and the greatest amount of experience
with electroforming is with nickel.

(1)   Physical and Mechanical Properties of Electroformed
Nickel

The range of properties reported for electroformed
nickel is so great as to make it difficult to determine what properties may be
used for design allowables. J. G. Kura, et al[8] report a range of properties,
as listed below, and includes a review of the principles of electroforming and
the factors contributing to the great range of properties.

Density, lb/in.^{3}	0.321 to 0.327
Modulus of elasticity, lb/in.^{2}	23 to 28 million
Electrical resistivity, micro ohm-cm	7.4 to 10.9
Coefficient of linear expansion (near room temperature) micro in./°F	3.1 to 6.3
Ultimate tensile Strength, lb/in.^{2}	55,000 to 215,000
Yield strength, lb/in.^{2}	32,000 to 128,000
Elongation in 2 in., %	2 to 37

III, A, Material and Process Selection (cont.)

Results of tests performed at Aerojet on two tubular specimens of electroformed nickel and three flat specimens, and test data furnished by Camin Laboratories, Inc., who will do the electroforming for this program, appear in Table IV. Although one source[9] reports ultimate strength at 800°F of 50 to 70 ksi and yield strengths of 30 ksi, it is expected that continuous exposure to 1000 to 1300°F temperature will result in physical properties similar to that of pure wrought nickel. Typical properties of pure nickel over 500°F, as reported by International Nickel Company[10], were used in design calculation and the higher tensile properties characteristic of electroformed nickel (sulfamite solution with stress reducer) were used at 500°F and lower temperatures. Figure 12 shows curves fitted to the data from Table IV and Reference 10.

(2) Electroforming Process Development

Selection of Conductive Intermediate Coating: The electroforming of nickel over a $50W/50ZrO_2$ plasma-sprayed coating is a new technique as far as could be determined. Since zirconia is an insulator, the coating is nonconductive. Camin Laboratories proposed that solving this problem would have to be accomplished by experimentation and that selection of the intermediate coat, if any, would be based on results of shear tests. Results of experiments and tests indicate that plasma-sprayed pure nickel is a satisfactory conductive coat.

Several materials were considered for a conductive coat over the thermal barrier to facilitate nickel plating and the following materials were plasma-arc sprayed on a $50W/50ZrO_2$ substrate: nickel, nichrome, nickel aluminide, silver, and copper. Some difficulty was experienced with coating flat plate specimens as shown in Figure 13. Because of the method of spraying, it was not possible to cool the face of the specimen while spraying. This resulted in total shrinkage of all the passes on cooling,

TABLE IV

MECHANICAL PROPERTIES OF ELECTROFORMED NICKEL

Specimen Number	Temp	Ultimate Tensile Strength, ksi	Yield Strength 0.2% Offset, ksi	Elongation, %
1 (flat)	RT	114.7	89.1	8.0
2 (flat)	RT	115.1	89.3	9.5
3 (flat)	RT	121.0	96.1	6.5
4 (tubular)	RT	94.8	---	---
5 (tubular)	RT	93.5	89.7	---
6 (tubular)	RT	106.5	---	20.0
7 (tubular)	500°F	71.5	---	25.0
8 (tubular)	1000°F	27.6	---	42.0
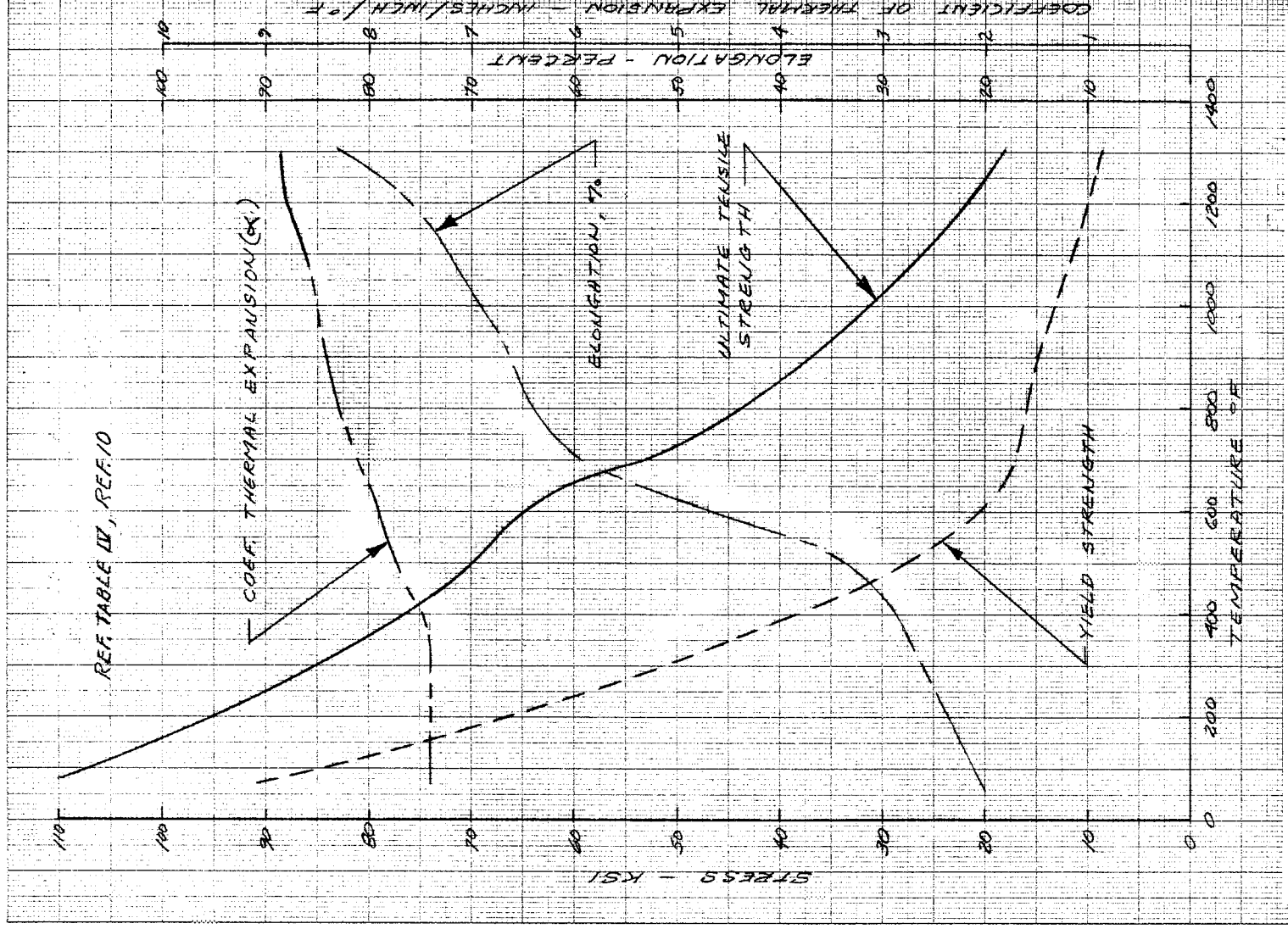
Figure 12. Tensile Properties Electroformed Nickel

Page 33
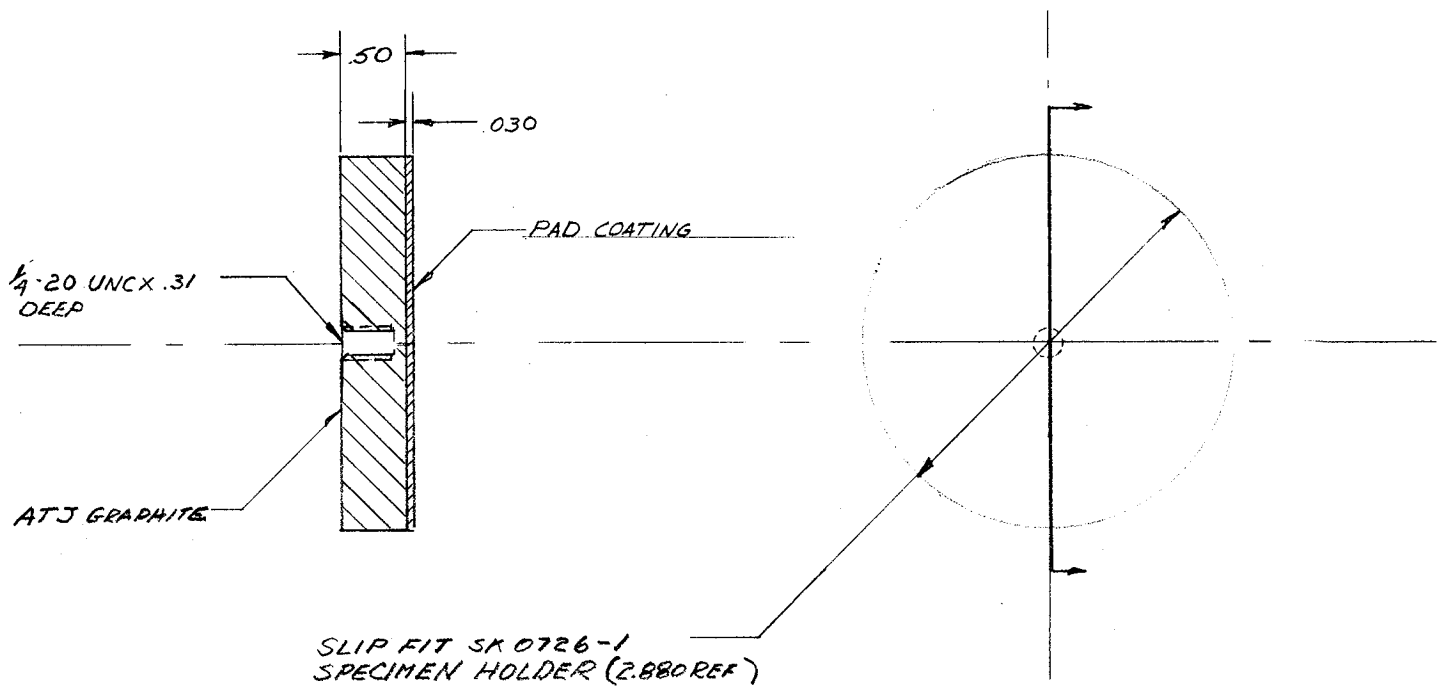
Figure 13. Specimen - Electroform Adhesion

III, A, Material and Process Selection (cont.)

causing the tungsten-zirconia substrate to lift-off the graphite disc. A
change was made to a cylindrical specimen, 3.0 in. in diameter by 3.25-in.-
long, which more nearly approximated the conditions to be experienced in
fabricating the thrust chamber. Cracking at the ends occurred when these
specimens were sprayed with nichrome; however, by rounding the edges, main-
taining the graphite at 200 to 300°F, cooling with air while spraying and
covering the specimen after spraying to ensure a slow cool, specimens were
made successfully and forwarded to Camin Laboratories for electroforming
experiments. Several smaller specimens shown in Figure 14 were made to the
size specified by Camin Laboratories to be used as shear test specimens.

The photograph shown in Figure 15 shows the thermal
cracking of the coating when sprayed with 0.002 in. pure nickel over 0.030 in.
tungsten-zirconia without preheat and slow cool (left), and 0.002 in. nickel-
aluminide sprayed on tungsten-zirconia (right) using a preheat of 200°F and
slow cool. Figure 16 (left) shows a gradated tungsten-zirconia coating made
up of 0.030 in. pure tungsten, 0.010 in. $85W/15ZrO_2$, and 0.078 in. $50W/50ZrO_2$.
All tungsten-zirconia spraying was done with air cooling during spraying. The
specimen in the right side of the photograph was coated with 0.008 in. $50W/50ZrO_2$
and plated with electroless nickel and electro-deposited nickel. This specimen
was sectioned for metallographic examination (Figure 17) for comparison to
other conductive intermediate coatings. Work at Aerojet was limited to
preparation of coated specimens and metallographic examination conducted on
three specimens, Figures 17, 18, and 19. Examination of the photomicrographs
reveal that the bond of electroless nickel to $50W/50ZrO_2$ can be expected to
be poor, as evidenced by the voids (dark areas) at the interface. On the other
hand, the bond of electroless nickel-to-nickel-aluminide and the bond of
electroformed nickel-to-nickel-aluminide show considerably more evidence of
intimate contact and penetration into the pores without bridging.
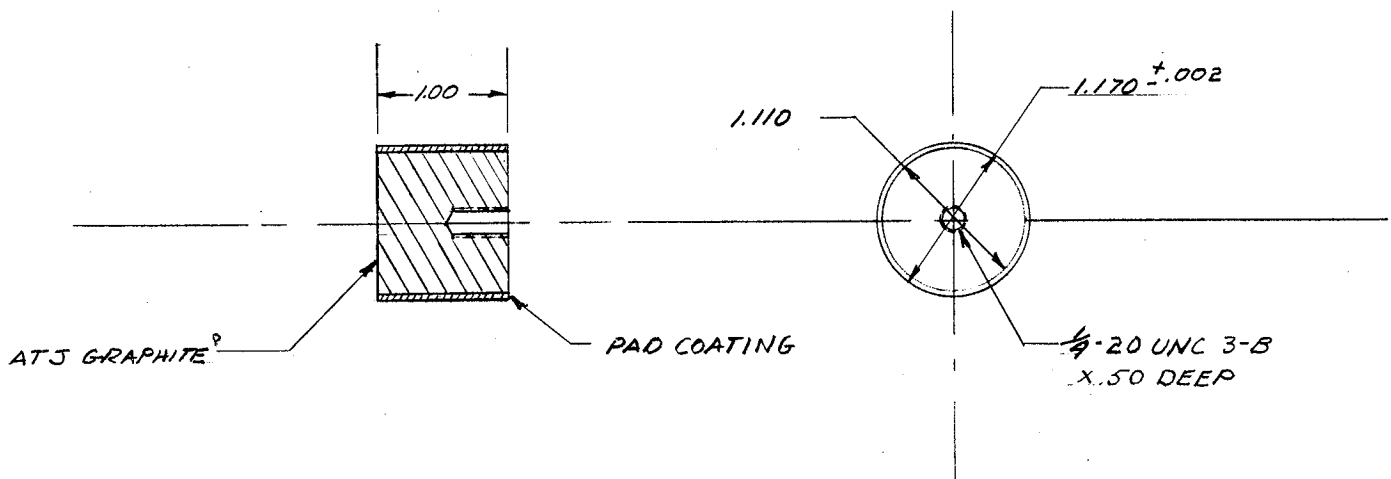
Figure 14. Shear Test Specimen - Electroforming
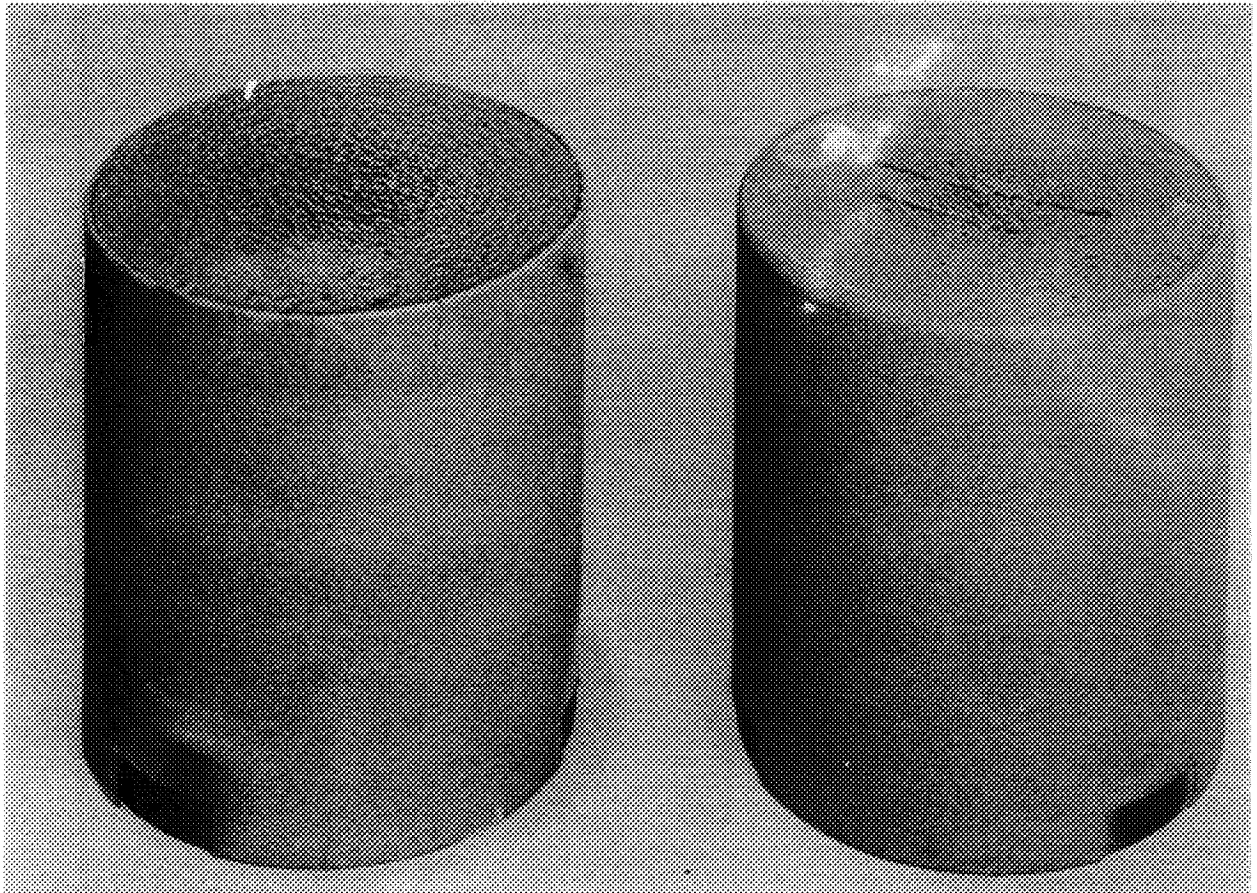
Figure 15.   Plasma Arc Sprayed Specimen Showing Thermal Cracks
(left) and Without Cracks After Process Change
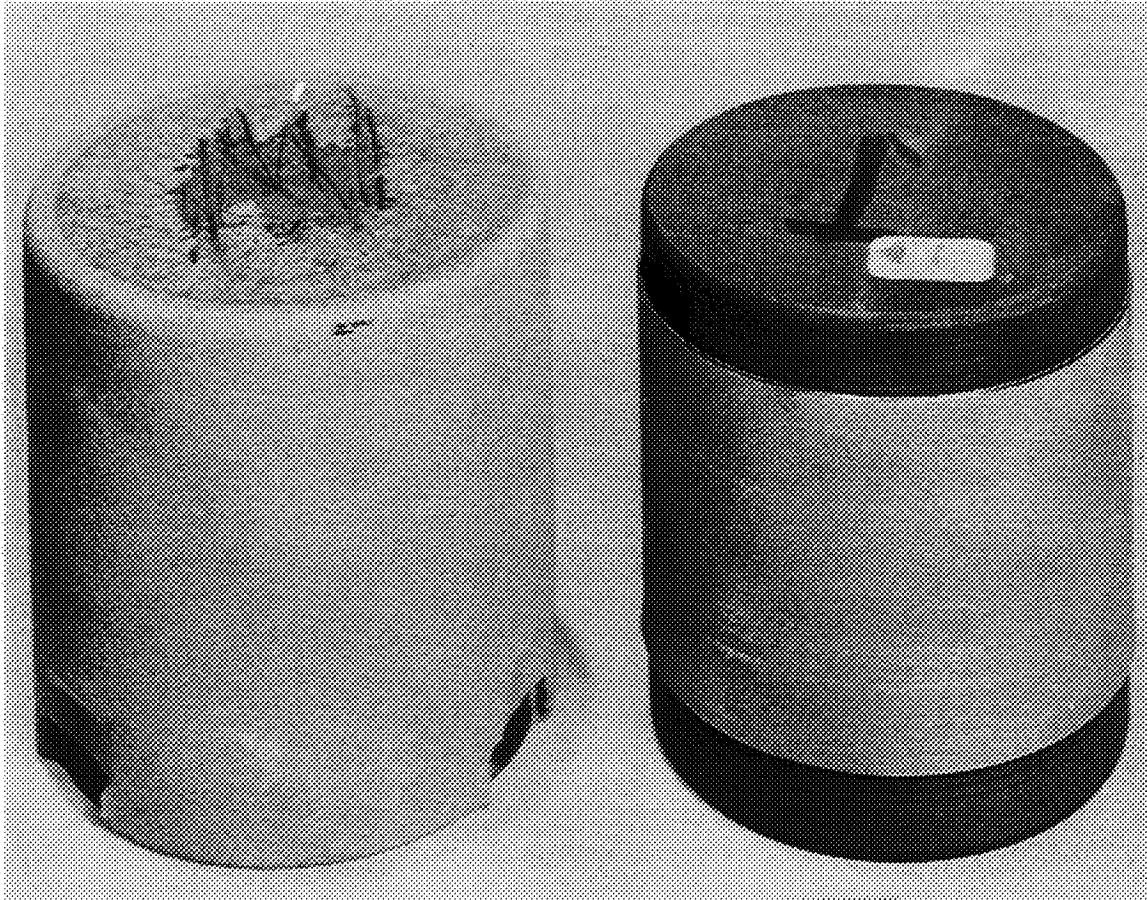
Figure 16. Specimen - Thick Plasma Sprayed Gradated Tungsten-
Zirconia and Specimen With Electroformed Nickel
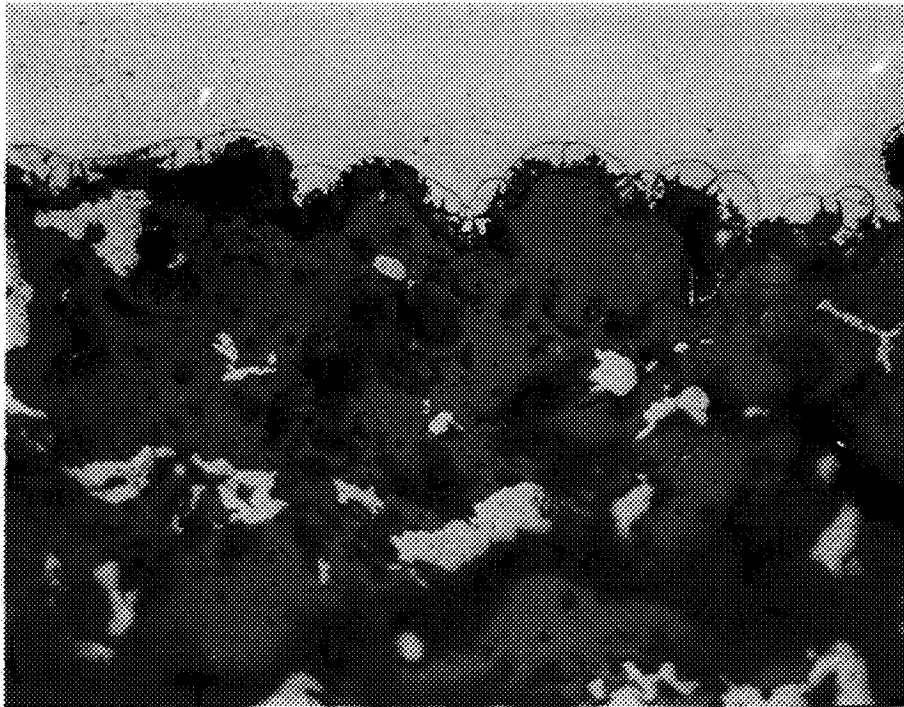
Electroformed Ni

Electroless Ni

50% W-50% ZrO_2

Mag: 500X   Etchant: 1% Nitric, H_2O Elect.

Figure 17. Electroless Nickel and Electroformed Nickel on $50W/50ZrO_2$
Substrate
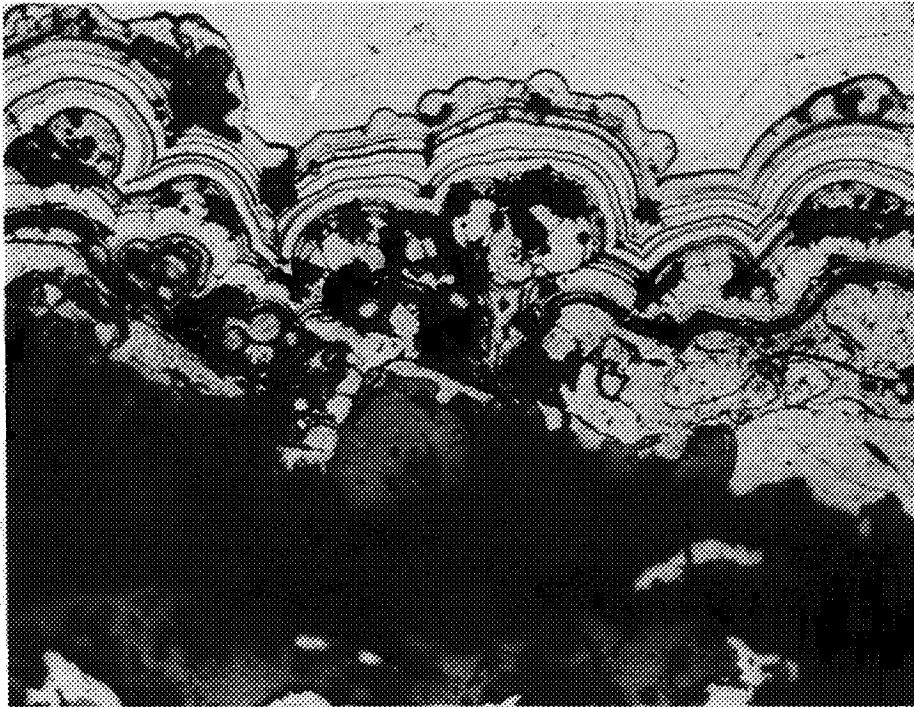
Electroformed Ni

Electroless Ni

Ni Aluminide

50% W-50% ZrO$_2$

Mag: 500x   Etchant: 1% Nitric, Electrolytic

Figure 18.   Electroless Nickel and Electroformed Nickel on
                  Nickel-Aluminide Substrate
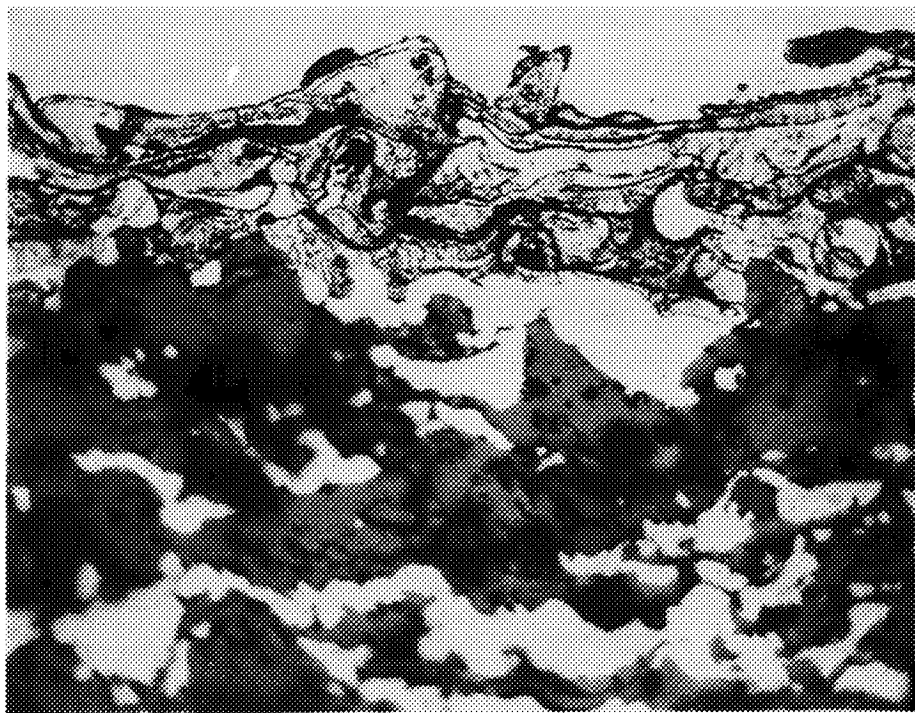
Electroformed Ni

Ni Aluminide

50% W-50% ZrO_2

Mag: 500X   Etchant: 1% Nitric, Electrolytic

Figure 19. Electroformed Nickel on Nickel-Aluminide Substrate

III, A, Material and Process Selection (cont.)

Using a 3.0-in.-dia specimen furnished without a metallic topcoat, Camin Laboratories conducted experiments with silver and with electroless nickel. The silver used was DuPont Dip Spray Compound 8004 brushed on and fired at 1200°F in air. The furnace was brought up to 1200°F and turned off. The specimen was left in the furnace to slow cool. The specimen was shipped to Aerojet where examination proved the coating had disappeared entirely. The probable cause of failure is thermal expansion mismatch of the coating and the graphite (ATJ). Results of Camin's experiments and tests with electroless nickel and with plasma-sprayed silver, nickel, and copper specimens are described below:

Ten shear test specimens (Figure 14) were furnished by Aerojet, plasma-arc coated, as follows:

Specimen No.	Base Coat	Conductive Top Coat
1 through 3	50W/50ZrO$_2$	0.003 in. pure nickel
4 through 6	50W/50ZrO$_2$	0.003 in. silver
7 through 9	50W/50ZrO$_2$	0.003 in. copper
10	50W/50ZrO$_2$	none

Figure 19A shows the intimate bond of electro-formed nickel over plasma-sprayed nickel.

Specimens 1 through 9 were plated with nickel by electroforming; Specimen 10 was plated with electroless nickel, then electro-formed nickel. Figure 20 shows a coated specimen before and after electro-forming. When subjected to a shear bond strength test, all specimens failed in the bond of W/ZrO$_2$ coating to graphite.
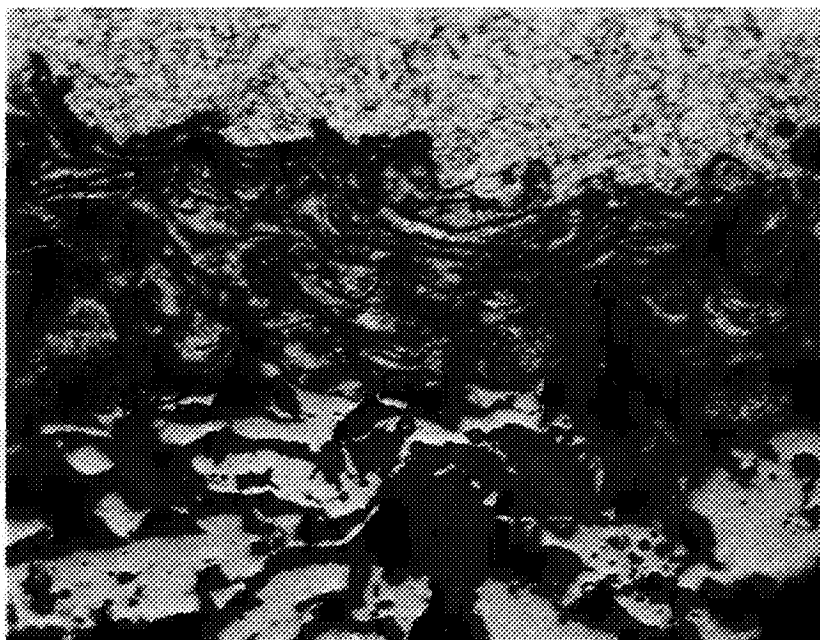
Electroformed Nickel

Plasma Sprayed Nickel

50% W-50% ZrO_2

Mag: 500X　　　　　　Etchant:　1% Nitric, Electrolytic

Figure 19A.　Electroformed Nickel on Plasma-Sprayed Nickel Substrate
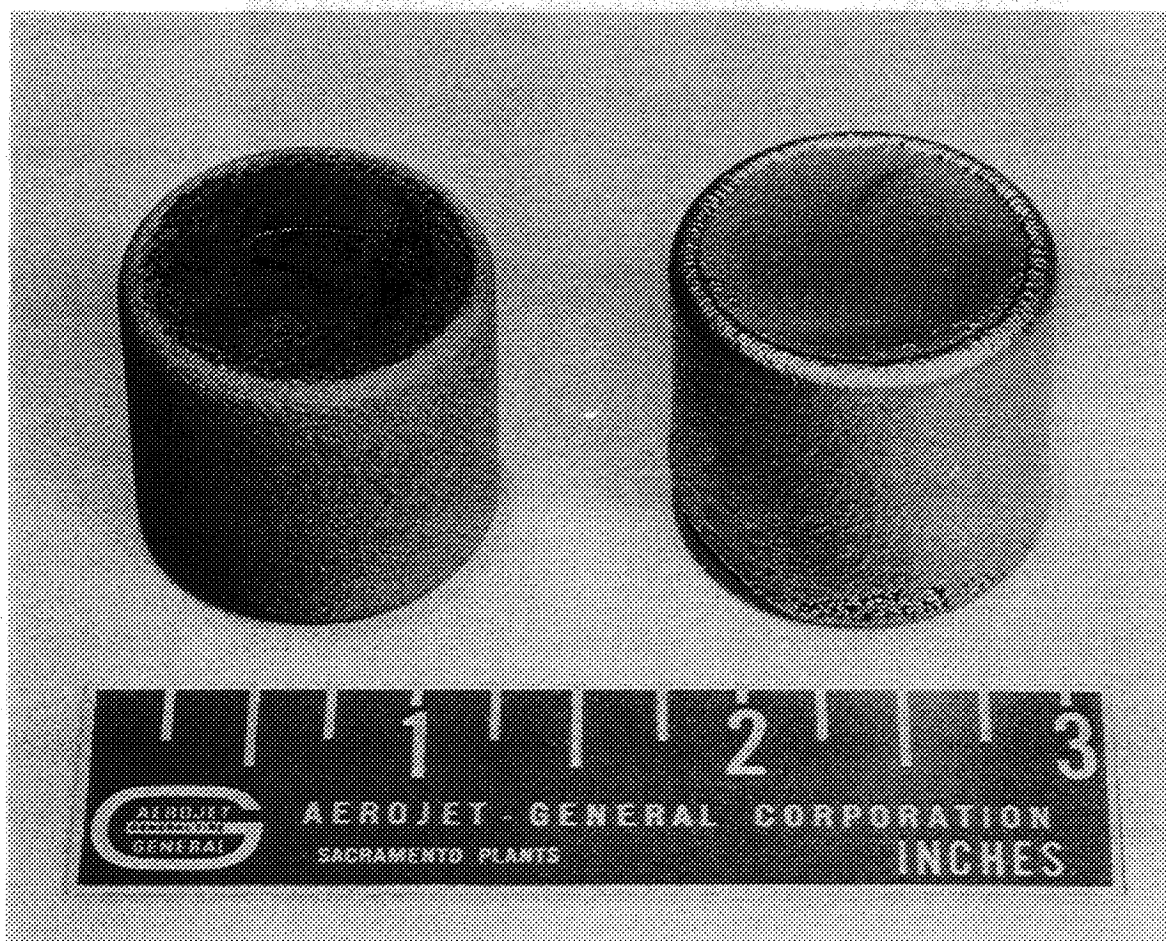
Figure 20.   Coated Shear Bond Strength Specimen Before and
After Electroforming

III, A, Material and Process Selection (cont.)

A conclusion is that electroformed nickel bonds reasonably well to all of the metallic surfaces of low electrical resistivity that were tested, and that the test method selected is not capable of producing qualitative measurements of the bond strength of electroformed nickel to thermal barrier coatings.

Plasma-arc sprayed nickel was selected as the intermediate conductive coating, based on the following facts:

(1) Camin Laboratories was unable to electroform directly on the $50W/50ZrO_2$ coating.

(2) The bond of electroless nickel to $50W/50ZrO_2$ is poor, as evidenced by voids in the bond area (Figure 17).

(3) The bond of electroformed nickel to plasma-sprayed nickel-aluminide, nickel, silver, and copper appear to be equally satisfactory although for unknown reasons, the load at failure of the tungsten-zirconia coating bond to the graphite was significantly higher with nickel-sprayed specimens than with silver or copper-sprayed specimens.

(4) Pure nickel is easily sprayed and, having the same coefficient of thermal expansion as electroformed nickel, creates no mismatch at the bond line.

c. Process Development at Camin Laboratories

Camin Laboratories has submitted a report reviewing design consultation with Aerojet personnel and laboratory experiments and testing during Task I. The testing described above was performed under Camin Laboratories cognizance and the thrust chamber design involving electroformed nickel is a result of numerous conversations and communications with Camin Laboratories personnel.

III, A, Material and Process Selection (cont.)

4. Manifold and Flange

a. Material Selection

The manifolds will be fabricated from T304L stainless-steel sheet. Half-shell stampings will be made and welded together using the TIG process and T349 weld wire. The inlets and outlets will be T304L tubing. The injector attach flange will be plasma-arc cut from T304L plate. The nozzle extension attach flanges are planned as T304L ring forgings. The physical and mechanical properties of T304L corrosion resistant steel are shown in Table V.

The selection of T304L material for the components listed above over other 300 series stainless steels is for ease of welding. Cracking problems have been experienced with Electron Beam welding of T347 material where no filler wire is added. T304L has somewhat better flow characteristics than T321 in TIG welding. Any TIG welding of T304L to T304L will be done with T349 weld wire; however, if any filler wire is necessary, Number 61 nickel weld wire will be used.

b. Process Selection

The Electron Beam welding method was selected for the manifold to chamber and flange to chamber joints to accomplish the welding with a minimum of heat input and thereby minimizing the possibility of separation of the coating from the inner shell due to localized thermal expansion.

The joining of the injector manifold to the injector flange will be accomplished by Tungsten Inert Gas Welding as a subassembly. A further description of joining operations appears in the Fabrication Analysis Section of this report.

III, A, Material and Process Selection (cont.)

5. Ablative Nozzle Extension

a. Material Selection

The primary criterion for selecting materials for use in engines with fluorine oxidizer is chemical compatibility. Of the currently used ablative materials, only those containing graphite or carbon reinforcement can be used. Carbon-reinforced phenolic was selected for the flame liner, since it has a lower thermal conductivity and costs less than graphite-reinforced phenolic. Of the carbon-reinforced phenolics that have been evaluated, WB-8217 appears to be the best candidate because of its good thermal stability and because it uses a high-char resin system which will result in fairly high strength even when completely charred. The liner will, therefore, remain structurally intact even for extended firing durations.

The insulation external to the flame liner is not exposed to the combustion gases and chemical compatibility is therefore not a problem. The most important criteria for material selection are: (1) low thermal conductivity; (2) low thermal expansion and contraction; (3) thermal stability; and (4) structural integrity. The two outstanding candidates are asbestos-reinforced phenolic. It was selected because it is thermally more stable than asbestos-reinforced phenolic. At the relatively high interface temperatures existing after 180 sec of firing duration (about 2100°F), the shrinkage of asbestos phenolic might cause excessive separation with the possibility of gas flow between the liner and insulation. There are many satisfactory silica-reinforced phenolics available. WB-2230 is preferred, however, because it uses the same high-char resin system as WB-8217, which is the preferred flame liner material.

III, A, Material and Process Selection (cont.)

5. Ablative Nozzle Extension

a. Material Selection

The primary criterion for selecting materials for use in engines with fluorine oxidizer is chemical compatibility. Of the currently used ablative materials, only those containing graphite or carbon reinforcement can be used. Carbon-reinforced phenolic was selected for the flame liner, since it has a lower thermal conductivity and costs less than graphite-reinforced phenolic. Of the carbon-reinforced phenolics that have been evaluated, WB-8217 appears to be the best candidate because of its good thermal stability and because it uses a high-char resin system which will result in fairly high strength even when completely charred. The liner will, therefore, remain structurally intact even for extended firing durations.

The insulation external to the flame liner is not exposed to the combustion gases and chemical compatibility is therefore not a problem. The most important criteria for material selection are: (1) low thermal conductivity; (2) low thermal expansion and contraction; (3) thermal stability; and (4) structural integrity. The two outstanding candidates are asbestos-reinforced phenolic. It was selected because it is thermally more stable than asbestos-reinforced phenolic. At the relatively high interface temperatures existing after 180 sec of firing duration (about 2100°F), the shrinkage of asbestos phenolic might cause excessive separation with the possibility of gas flow between the liner and insulation. There are many satisfactory silica-reinforced phenolics available. WB-2230 is preferred, however, because it uses the same high-char resin system as WB-8217, which is the preferred flame liner material.

III, A, Material and Process Selection (cont.)

The attachment flange must be capable of transmitting the imposed loads from the nozzle extension to the thrust chamber. Stainless steel 304L was selected to be compatible with the chamber flange. The thermal environments would not permit the use of aluminum and titanium did not seem warranted because of its higher costs and because the weight of the stainless-steel flange is only about 9 pounds.

The simplest and least costly method of securing the flange to the ablative extension is to apply phenolic impregnated glass cloth and roving over the flange and extension. Other approaches could be used, but they would be more complex, more expensive, and heavier. Table VI lists the important properties of the materials selected for the nozzle extension.

b. Process Selection

Two elements are involved in the fabrication of ablative-reinforced plastics: (1) the laying-up of the tape, or shaped ply or molding compound; and (2) the curing of the resin impregnant by the use of heat and pressure.

The configuration of the ablative component will usually determine which of the lay-up methods and material types (tape, cloth, molding compound) is most suitable and the size of the component will often determine the method of curing (availability of facilities).

The nozzle extension is of a design which favors tape-wrapping operations. Other approaches would require more labor time or higher tooling cost. Since the orientation of the tape is either parallel to the part centerline (liner) or parallel to the surface (insulation), warp tape can be used and will be less costly than bias-cut tape.

TABLE VI

NOZZLE EXTENSION MATERIAL PROPERTIES

Material	Type**	Specific Gravity	Thermal Conduct @ 300°F Btu-in./ft^2-hr-°F	Specific Heat Btu/lb-°F	Thermal Expansion @ 300°F in/in.-°F x 10^{-6}	Tensile Strength @ 100°F, psi	Tensile Modulus @ 100°F psi x 10^6
Carbon-Phenolic	WB-8217	1.50	5.6	0.29	10.4	7,700	2.0
Silica-Phenolic	WB-2230	1.75	2.4	0.28	4.4	9,000	2.1
Glass Cloth	-143	1.9	2.0	0.24	4.0	90,000	5.8
Glass Roving	XF-5255	2.0	2.2	0.30	4.0	400,000*	7.8
CRES	304L	7.9	113	0.12	9.6	75,000	28.0

*Impregnated Strand
**WB-8217 and WB-2230 are products of Western Backing Corp.
  XF-5255 is a product of U.S. Polymeric Chemicals, Inc.

III, A, Material and Process Selection (cont.)

The size of the nozzle extension is small enough for
hydroclave curing. Most plastic manufacturers have facilities for this size.
Pressure during curing is for the purpose of compacting the part to obtain
better structural properties. If a large amount of compaction (debalking) can
be achieved during wrapping, it may be possible to decrease the requirement
for high pressure during curing. Inasmuch as facilities are available for the
extension, and no extra cost is involved, the recommended process is hydroclave
curing.

III, Task I--Design and Analysis (cont.)

B. FABRICATION ANALYSIS

1. Introduction

Fabrication feasibility and cost are primary limiting factors in mechanical design; therefore, it is desirable that the fabrication analysis be conducted concurrent with design and drafting. The selection of materials and the material form fairly well establish the fabrication approach; however, as the configuration, sizes, and component details were developed, fabrication aspects were reviewed for feasibility and cost and the basic fabrication plan was verified. The following paragraphs will describe the fabrication sequence, the processes to be used, the analysis and testing to be performed to confirm the detailed process plan.

2. Fabrication Approach and Production Sequence

		Drawing
a.	Fabricate graphite mandrel	1131937
b.	Application of screen and vapor deposition of tungsten (specification AGC 46897)	1132002
c.	Plasma-arc spray graduated thermal barrier (specification AGC 46898)	1132002
d.	Package and ship to Camin Laboratories, Brooklyn, N.Y.	
e.	Electroform inner shell, ribs, and outer shell; machine to final dimensions, ship to Aerojet	1133462
f.	Fabricate Components:	
	(1) Forward chamber flange	1132563
	(2) Manifold half shells	1132714
	(3) Inlet and outlet ducts	1132563
	(4) Nozzle extension attach flange	1132645

III, B, Fabrication Analysis (cont.)

			Drawing
g.	Assemble and Weld Subassemblies:		
	(1) Inlet manifold and duct		1132644
	(2) Outlet manifold and duct		1132563
h.	Machine outlet manifold		1132563
i.	Assemble and weld outlet manifold to forward flange		1132563
j.	Machine chamber to length and remove graphite mandrel; grit-blast to remove residual graphite		1132625
k.	Machine outlet and inlet manifold assemblies to fit thrust chamber		1132563 1132644
l.	Ship chamber and subassemblies to E.B. welding facility (Von Karman Center in Azusa)		
m.	Complete E.B. welding		1132625
n.	Ship to fabrication shops (Sacramento Plant)		
o.	Machine forward flange and nozzle extension attach flange		1132625
p.	Leak and flow test with water		1132625
q.	Install thermocouples		
r.	Thermal shock test with LN_2		1132625
s.	Remove thermocouples, package and ship to NASA-Lewis Research Center, Cleveland, Ohio		

3. Flame Liner

a. Process Description

The chemical vapor plating of tungsten is a reduction process whereby the halide of the metal is reduced by hydrogen to form metallic tungsten and HF or HCl, according to the following reaction:

III, B, Fabrication Analysis (cont.)

$$WF_{6(g)} + 3H_{2(g)} \xrightarrow{\text{heat}} W_{(s)} + 6HF_{(g)}$$
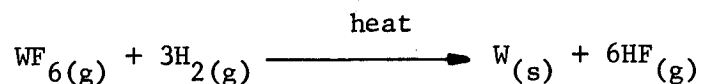
The reaction occurs at the heated surface of the part, the metal condenses on the surface and the other reaction product, HF, passes off as a gas. Pyrolytic-tungsten deposition occurs at temperatures above 392°F. Temperature is the primary rate controlling parameter with the deposition rate increasing with temperature. Although other investigators have plated at 1200°F and above, it has been found that the process is easier to control at lower temperature. At 650°F, the deposit is smooth with only a few nodules and uniform in thickness across a reasonable distance.

b. Equipment and Facilities

The entire chemical vapor deposition facility is placed in a large spark-proof hood. The chamber in which the reaction takes place is 31 in. in diameter and 40-in.-high. The substrate to be plated is placed on a turntable inside the chamber and the chamber sealed to exclude air and moisture. The substrate is rotated at about 5 rpm during plating to ensure an even coating. Heat is provided by a bank of quartz infrared lamps placed outside the chamber and focused on the substrate through a quartz window. The lamps are controlled individually to control the power input along the length of the substrate. The photograph, Figure 21, shows the chamber, hood, and the graphite mandrel. The inside of the chamber is painted with a high-temperature, aluminum-filled silicone paint for high reflectivity. Also, the chamber and the frame for the quartz window are water cooled to below the lower deposition temperature to prevent tungsten from plating on them. Although it has been reported that the reaction rate between HF fumes and quartz is very slow, a purge tube placed around the window floods it with argon for added protection.
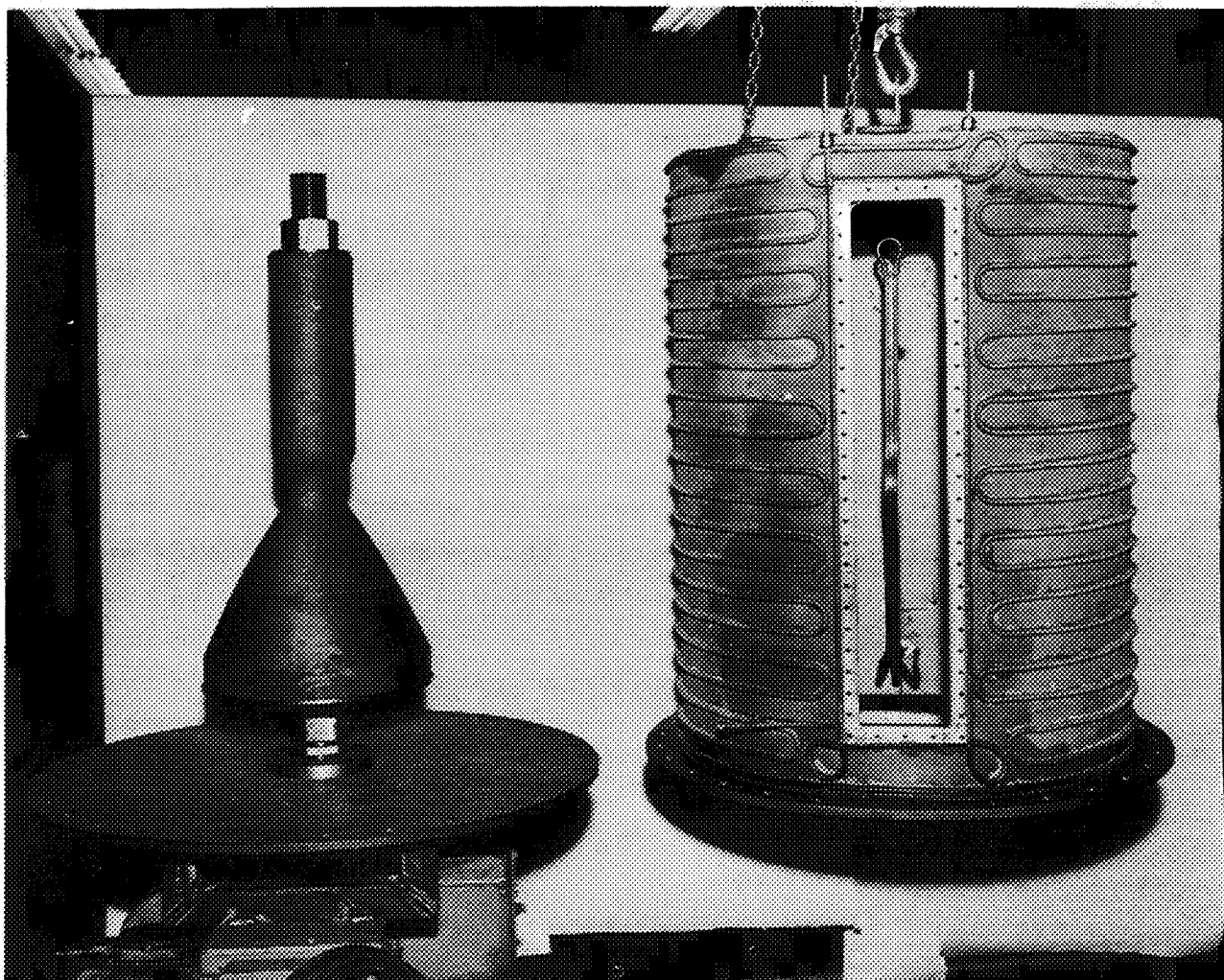
Figure 21.   Vapor Deposition Mandrel and Equipment

III, B, Fabrication Analysis (cont.)

The substrate temperature is measured with a series of thermocouples placed just beneath the surface of the graphite. Stainless-steel-sheathed thermocouples were placed in holes in the substrate and the lead wires brought down through the center bore. The tip of the sheathed thermocouple is threaded into a graphite plug and the plugs are cemented in holes in the substrate, then blended with the substrate contour.

The reactive gases are mixed and metered before entering the chamber through a water-cooled manifold. The manifold is shaped to follow the graphite mandrel's contours. The WF_6 gas is metered by a Brooks Kel-F flow meter, which has been calibrated with a Hastings Mass Flow meter. The H_2 gas is metered by a Mathison tubular flow meter. The piping system is redundant, if valve or line plugs up, the plating run will not have to be discontinued.

A cold trap removes the unreacted WF_6 from the exhaust gases. The remaining gases are bubbled through a sodium hydroxide solution to remove the HF.

c.   Process Development and Equipment Control

The gas seals, connections, valves, and gaskets are leak-checked at room temperature and at operating temperature before the reactive gases are introduced.

One subscale sample will be produced to determine flow rates, deposition time and to prove the design of the reactive gas manifold. Four short deposition runs, 10 to 16 hours of deposition time each, are planned with a 24-hour heat up and cooldown time. After each run, the thickness and uniformity of the coating will be checked by diametric measurements

III, B, Fabrication Analysis (cont.)

and the deposition rates noted. The part will be examined closely for cracking, nodules, and other plating defects.

d. Plan for Vapor Deposition of Flame Liner

(1) Mount mandrel in plating position and install water-cooled furnace shell.

(2) Start helium purge, purge both primary and redundant piping.

(3) Turn on hood fan.

(4) Turn on liquid N_2 to thrust bearing.

(5) Turn on chamber water coolant.

(6) After 75 ft^3 of helium (five times the volume of the chamber) has been used, infrared heat lamps are turned on to provide a heating rate of 30°/hr. When one full bottle of helium (213 ft^3) has been used, argon may be used for the purge gas.

(7) When the temperature has stabilized at 650°F, the argon flow is gradually replaced by hydrogen at 8000 cc/min. Raise the Dewar flask of liquid N_2 to cover the cold trap.

(8) Turn on the argon flow to the quartz window, 5 ft^3/hr.

(9) Start the WF_6 flow and balance the hydrogen and WF_6 flow rates at 8000 cc/min and 600 cc/min, respectively.

(10) Monitor the reactive gas flow rates every 10 minutes and record gas flow rates and temperature every hour for the duration of the plating run.

(11) After 72 hr, remove the Dewar flask of liquid N_2 from the cold trap. Turn off the WF_6 and gradually replace the H2 flow with argon.

(12) The plated mandrel is cooled according to the following schedule:

III, B, Fabrication Analysis (cont.)

        (a) 650°F to 550°F, no greater than 10°F/hr.
        (b) 550°F to 400°F, no greater than 20°F/hr.
        (c) 400°F to 200°F, no greater than 40°F/hr.
        (d) Turn rheostat to zero when 200°F is reached.

(13) Examine coating for defects.

(14) Measure coating thickness with diametric measurements.

    e.   Tooling and Graphite Mandrel Fabrication

A steel mandrel was designed and fabricated to be used in vapor deposit process development and the production of one subscale sample. A shorter mandrel will be used for graphite machining and chamber fabrication in Task II. This tool will probably be destroyed in the electro-forming process and is, therefore, considered consumable. The existing mandrel will be used for vapor deposition only during Task II.

The graphite blocks are bored to a close slip fit with the steel mandrel and bonded together with Sauereisen cement. Then the out-side surface is machined to the thrust chamber contour. The graphite mandrels are consumed in the manufacturing process, since they are machined and sand-blasted from the interior of the completed thrust chamber.

Grade H-205 graphite was chosen for the graphite mandrel material because of its high density, small grain size, and thermal expansion characteristics. A substrate is required which has a thermal expansion coeffi-cient slightly higher than the pyrolytic tungsten. When this situation exists, the tungsten coating will be in compression at all times when cooling from the plating temperature, minimizing the danger of tensile cracking. The coefficient of thermal expansion at 650°F of grades ATJ and H-205 graphite and tungsten are shown in the following Table. The high density of H-205 graphite is required to ensure a smooth surface on the thrust chamber wall after removal of the

III, B, Fabrication Analysis (cont.)

graphite. Since the pyrolytic tungsten will infiltrate all pores open to the surface during deposition, a porous graphite surface will result in a rough tungsten surface.

	H-205		ATJ		
	AG	WG	AG	WG	W
Thermal Expansion (in./in./°F$\times 10^{-6}$)	3.3	2.7	2.13	1.38	2.1
Density (g/cc)		1.75		1.73	19.3

As can be seen from the data in the table, H-205 graphite is also more isotropic than ATJ. The mandrel will be machined so that the direction of the greatest thermal expansion, across grain (AG), will be parallel with the axis of the mandrel. The danger of cracking at the unsupported edge will be minimized by the reasonably close match of the thermal expansion of H-205 with the grain (WG), and tungsten.

4. Thermal Barrier

a. Process Description

The plasma-arc spraying process employs a high current electric arc that is concentrated and stabilized in the controlled atmosphere of a special nozzle. An inert gas flows through the arc where it is heated to a range of 5000 to 16,000°C and accelerated to supersonic speed. The gas forms a highly ionized plasma jet. A cross-sectional view of the top of a Model 57 plasma torch is shown in Figure 21A.

Plasma gases most commonly used are argon, nitrogen, and hydrogen separately and in combination. Materials to be sprayed are injected into the plasma stream in powder form in the torch downstream of the arc or slightly outside of the torch exit nozzle. The primary advantages of the

Water-cooled Lead

Coolant Tube

Rear Housing

Gas Ring

Electrode

Powder Feed

Nozzle

Anode
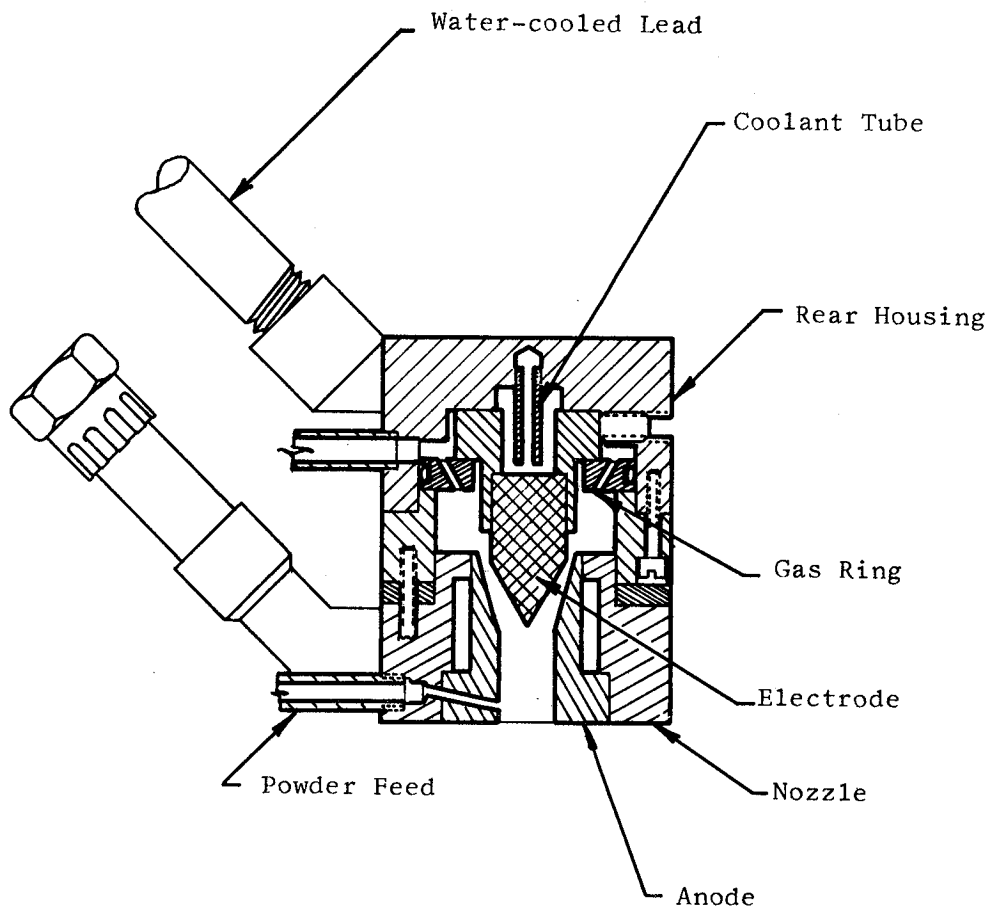
Figure 21A. Plasma Torch

III, B, Fabrication Analysis (cont.)

plasma-arc spraying process are the inherent neutral atmosphere, and the
exceptionally high temperatures achieved making it practical to process
refractory alloys, metals, ceramics, carbides, borides, and nitrides previously
restricted because of high melting points and sensitivity to gas environment.
Successful application of these materials depends on proper establishment and
control of the spraying variables in regard to the physical and thermal
properties of the particular material and the substrate.

      b.   Facilities and Equipment

          The plasma-arc spraying will be conducted in an existing
plasma-arc laboratory where special dust-collecting systems, water-cooling
systems, inert gas piping, and power panels have been installed. An existing
powered chamber rotation mechanism and pantograph feed control will be adapted
for use. A Tafa 57 plasma-arc torch will be used with a Metco 40 KVA power
supply and a Sylvester Mark VII powder feeder. A vacuum dehydrator is available
for drying powder before use.

      c.   Process Plan

          The requirement to furnish test specimens for
electroform experimentation and shear testing was used to advantage for
establishing spraying parameters. Spraying parameters previously established
for spraying tungsten and tungsten-zirconia composites were used and proved
to produce a uniform, crack-free surface. However, spraying of the flat plate
specimens (Figure 13) requested for electroform experiments, proved to be
unsuccessful when coatings lifted off the graphite substrate on application
of the final metallic conductive coating of 0.002 in. nichrome. The reason
for failure is the high thermal expansion of the nichrome, resulting in
excessive shrinkage on cooling, which overcame the relatively weak bond of

III, B, Fabrication Analysis (cont.)

tungsten to graphite. A cylindrical specimen was designed to replace the
flat disc. Two specimens were sprayed with $50W/50ZrO_2$ and topcoats of nickel
and nickel-aluminide. Again, excessive shrinkage of the topcoat caused edge
cracking (Figure 15). By preheating the tungsten-coated graphite to 200°F
before applying the metallic coat, and by increasing the surface speed to
50 surface feet per minute, top coats of nickel, silver, nickel-aluminide,
and copper were applied with no visible cracking.

(1) Spraying Parameters

The following spraying parameters have been
established for coating the thrust chamber:

Coating	$88W/12ZrO_2$	$75W/25ZrO_2$	$50W/50ZrO_2$	Nickel
Cooling	LN_2	LN_2	LN_2	LN_2
Arc Amps	480	480	480	450
Primary Gas and Flow	Ar 100 CFH	Ar 100 CFH	Ar 100 CFH	Ar 100 CFH
Secondary Gas and Flow	H_2 10 CFH	H_2 10 CFH	H_2 10 CFH	H_2 10 CFH
Carrier Gas and Flow	Ar 12 CFH	Ar 12 CFH	Ar 12 CFH	Ar 12 CFH
Shield Gas and Flow	Ar 100 CFH	Ar 100 CFH	Ar 100 CFH	Ar 100 CFH
Spray Distance	4.0 in.	4.0 in.	4.0 in.	4.0 in.
Feed (in./pass)	0.12	0.12	0.12	0.12
Surface Speed (FPM)	30	30	30	60
Torch	TAFA 57	TAFA 57	TAFA 57	TAFA 57
Graphite Temp	100 to 200°F	100 to 200°F	100 to 200°F	200 to 300°F*
Powder Feeder-Feed Screw	150 rpm	150 rpm	150 rpm	140 rpm
Vibrator	45 setting	45 setting	45 setting	45 setting

*Slow cool

III, B, Fabrication Analysis (cont.)

(2) Powder

Tungsten - 61F NS Fine (METCO)

Zirconium Oxide - MCA-151 (Norton Co.) -200 + 325 Mesh

Nickel - Pure Nickel Spray Powder (Varlicoid)
-200 + 325 Mesh

(3) Method

The thrust chamber will be coated using the rotation mechanism and hydraulic torch feeding mechanism shown in Figure 22. This equipment was designed for internal spraying of liquid propellant thrust chambers, but can be simply adapted to external spraying. A cam duplicating the chamber contour will be employed. It will be necessary to offset the torch from the boom, however, to clear the exit end diameter and maintain a constant torch-to-workpiece distance. The torch holder boom operates from a feed screw that can be controlled to give the selected forward feed per revolution of the chamber. A program will be developed to maintain a constant surface speed and a constant feed per revolution. Special tooling required will be adapting plates to secure the chamber to the large drive wheels and a manifold to carry the coolant to the chamber exterior directly below the chamber.

5. Channels and Structure

a. Description of Electroforming Process

Electroforming is a method which uses essentially the same concepts embodied for electroplating, except that the metal is deposited on a mandrel that is subsequently removed, leaving a self-supporting structure. A more important difference is in the thickness produced. Commercial electroplate of nickel is seldom over 0.001-in.-thick, whereas thicknesses of 1/4-in.
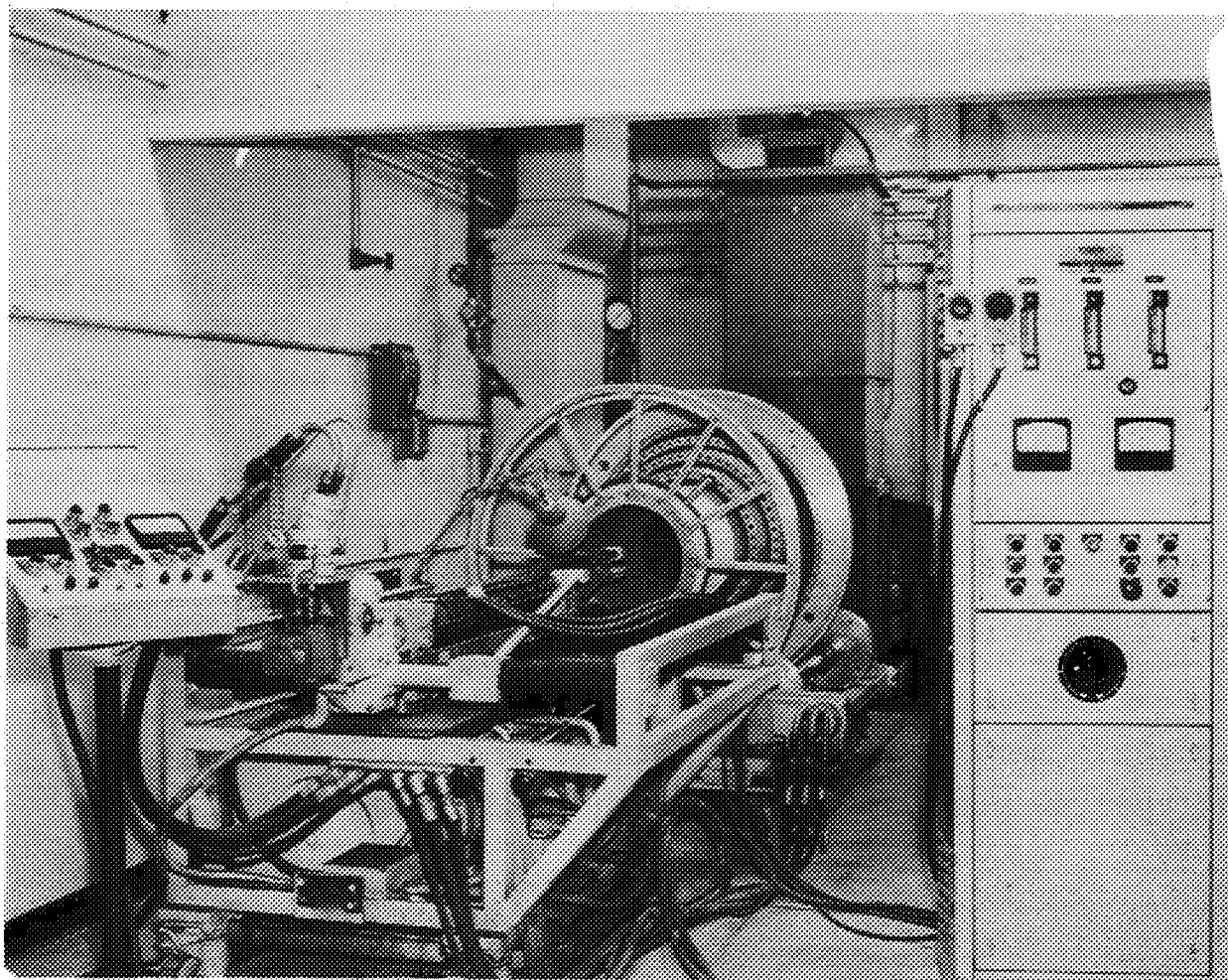
Figure 22.   Plasma Arc Facility and Equipment

III, B, Fabrication Analysis (cont.)

or more are possible in electroforming applications. Reference is made to sources such as the Electroplating Engineering Handbook by Graham for a description of the nickel electroplating process. In the application considered herein, the substrate is not removed, making the fabrication of the inner shell better defined as electroplating. However, subsequent use of a low melting core material for generation of the ribs and center shell meets the definition for electroforming.

b.   Design for Electroforming

Design Limitations: A basic limitation in electroplating and electroforming is the tendency to build up at corners and the difficulty of plating in narrow recesses or sharp internal corners. Deep and narrow recesses receive considerably less current than surfaces closer to the anodes. Special anodes that conform to the contour of the corner or recess may alleviate the problem somewhat, but these are expensive and of limited application. For more comprehensive review of the limitations of electroplating and electroforming as applied to large structures, see Reference 8.

Design Development: The tendency to build up on each corner can be useful, for example, on the ends of a thrust chamber where a thicker section is desired for attaching of flanges. Where buildup is undesirable, current shields of plastic material can be placed over corners and ends to reduce the buildup. The difficulty of plating in shallow recesses results in a sharp corner in the coolant channels. For flow, heat transfer and stress purposes, generous radii would be desirable.

In the process of determining the most feasible and economical technique for increasing the thickness of the outer shell at the forward and aft ends and at the inlet manifold attach point, several concepts

III, B, Fabrication Analysis (cont.)

were discussed with Camin Laboratories. Several of these concepts involved "grown in" inserts such as shown in Figure 23. This concept proved undesirable due to difficulty of "throwing in" nickel into the acute angle and the cost of the precision fit necessary between the machined insert and the chamber. The thick sections requiring a buildup to 0.250 in., as shown in Figure 24, was agreed to be feasible and less costly than "grown in" inserts. In this case, the chamber will be machined to the outer contour, masked and returned to the bath for the buildup in desired areas. A final machine operation is required to machine the thickened areas to dimension.

For proper evaluation of the chamber design and the chamber by firing tests, it is desirable to have the capability to monitor the temperature of the nickel inner shell at the thermal barrier interface. Installation of the thermocouples through the ribs with the tip within 0.030 in. of the thermal barrier was determined to be the only feasible location. Discussion with Camin Laboratories revealed that a hole through the rib could not be cored as the wall adjacent to the core would be thinner than permitted by the thickness to height limitation of 1 to 2. Further discussion resulted in agreement on the method illustrated in Figure 25, where a hole is drilled in the wall at the process stage where the ribs and plastic filler have been machined to height and contoured. This drilled hole will be about equal to one-half the rib height. A plastic or nylon core will be fitted to the hole and will remain in position while the outer shell is plated and machined. On removal of the core, a hole will extend from the outside of the chamber to a point halfway through the rib height.

Certain portions or aspects of Camin's electroforming process are proprietary; however, the following basic fabrication approach was freely divulged to assist Aerojet engineering personnel in developing a proper design.

TIG WELD
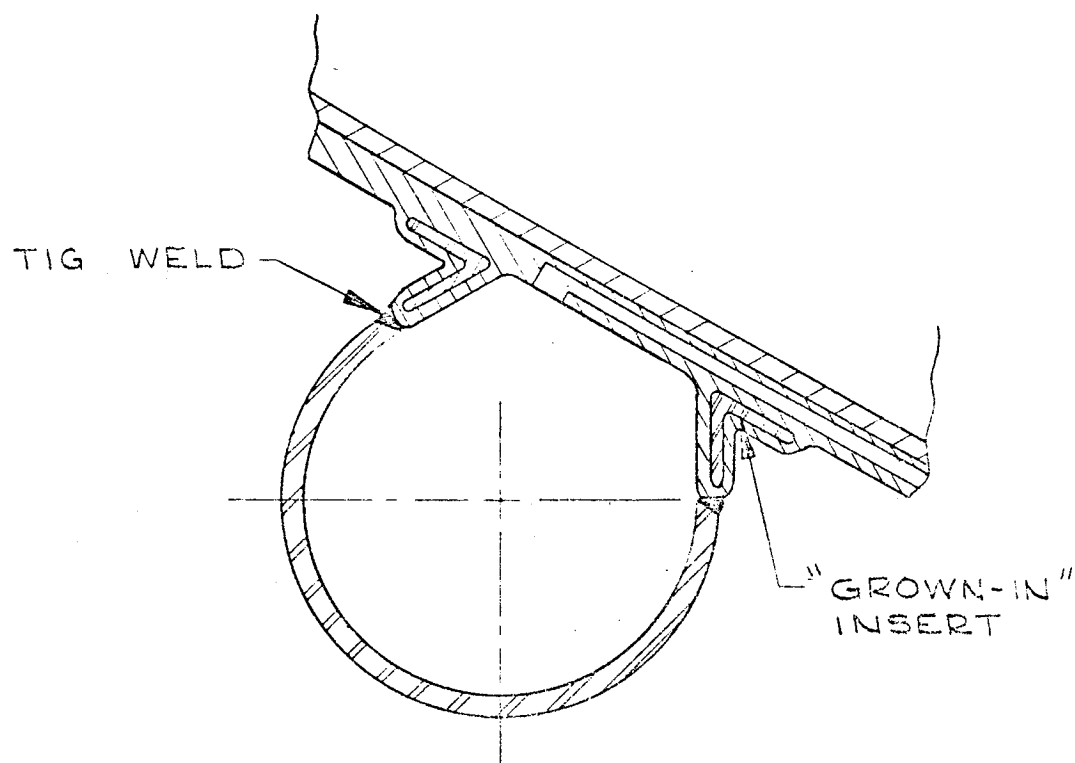
"GROWN-IN" INSERT

Figure 23. "Grown In" Insert by Electroforming
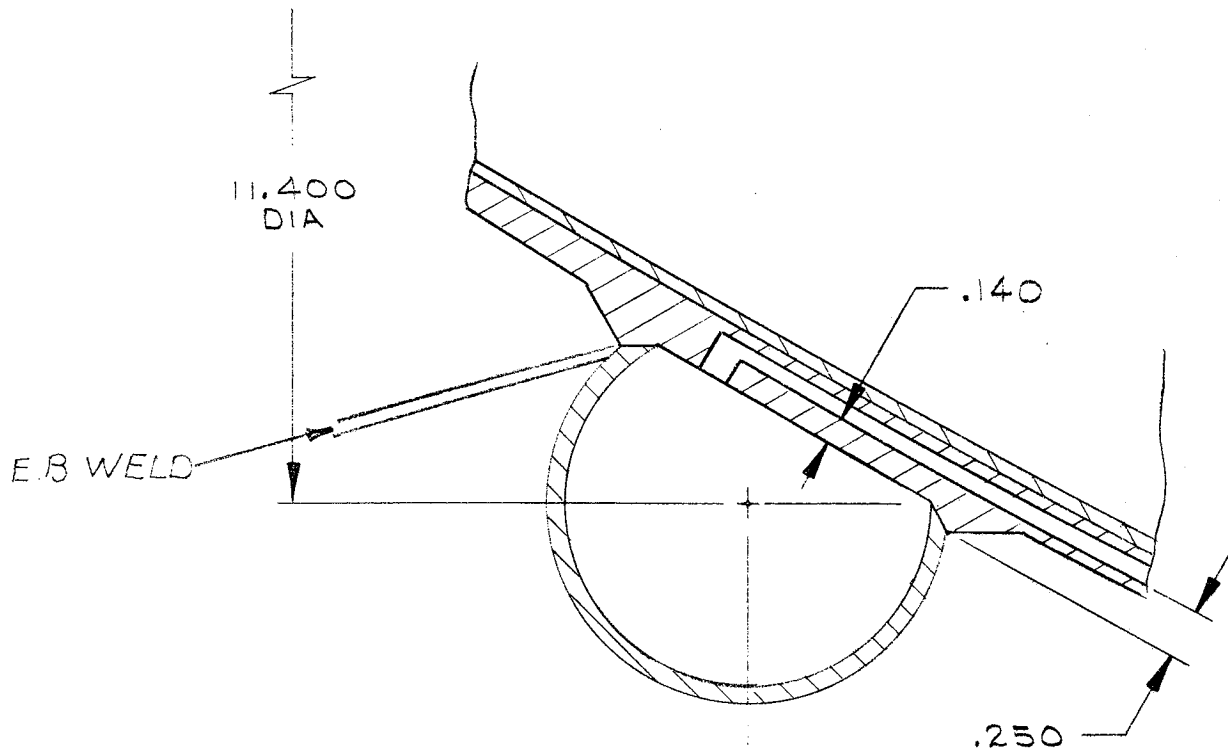
Figure 24. Joint Design - Inlet Manifold

STEP 1
DRILL .030 DIA X
DEPTH INDICATED

STEP 2
PLACE CORE

STEP 3
ELECTROFORM OUTER
SHELL

STEP 4
MACHINE COUNTOUR
& MELT OUT CORE

STEP 5
DRILL $\cdot^{.018}_{.019}$ DIA
TAP 6MM NATL MINAT.

STEP 6
INSTALL THERMOCOUPLE
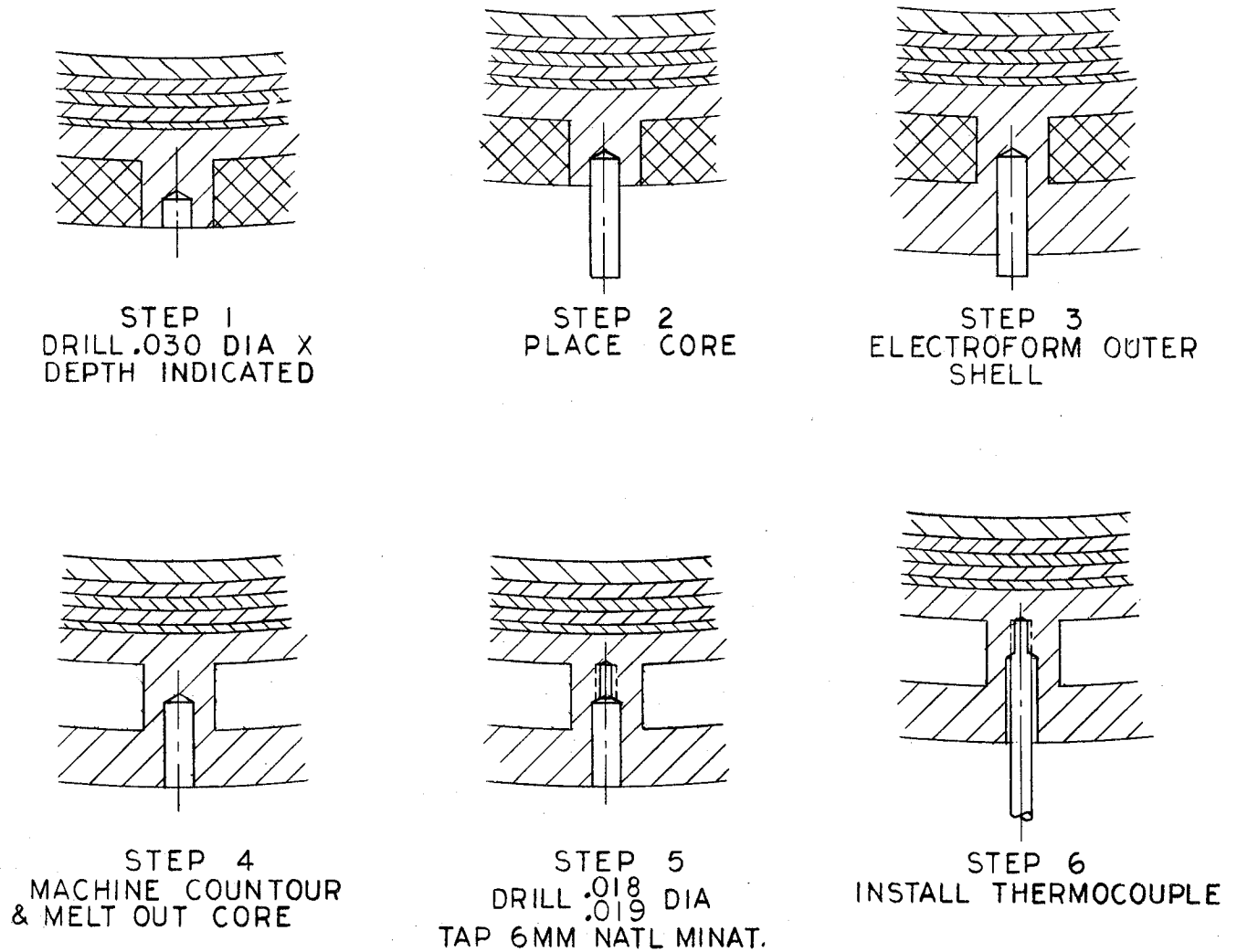
Figure 25. Thermocouple Installation

III, B, Fabrication Analysis (cont.)

(1)   A flash coat of a conductive material must cover the tungsten-zirconia substrate.

(2)   The inner shell is electroplated over the mandrel to a thickness several thousands over the finished thickness. The outside of the inner shell is machined using a tracer lathe to the desired thickness and finish. Normal machining practice governs tolerances and finish. Dimensions, however, must be from the axis centerline, not on the thickness.

(3)   The mandrel with the machined inner shell is covered with a thick coating of a low melting point plastic material by dipping, brushing or spraying and oven cured.

(4)   The plastic material is machined away in the areas where ribs or other raised areas are desired. It is desirable that all ribs be either radial or axial so that machining can be accomplished on a tracer lathe with a Dumore grinder attachment. Where a circular cutter leaves an undesirable radius, an end mill can be used to sculpture out the radius and obtain a square shoulder. Tapered ribs (width) are not feasible as the machine cuts would not be axial; however, rib width can be varied in steps by changing the width of the slotting cutter. Rib height can be tapered as height is a radial dimension from the axis and is controlled by the tracer template. Rib width-to-height ratio can be 1 to 3, but 1 to 2 is preferred for best results. Maximum height of ribs of any thickness and maximum thickness of any buildup is 0.12 in. Thickness greater than this will probably require an intervening machine cleanup cut and a second plating operation.

(5)   Holes can be cored in ribs or collars, but the area around the cored hole must not be in excess of the 1 to 2 thickness-to-height ratio. Cores are set by locating and drilling a small hole in the nickel and fitting a core of plastic material that can be subsequently pulled or melted out.

III, B, Fabrication Analysis (cont.)

(6) The mandrel is returned to the bath after the ribs are machined in the plastic material and plating builds up these areas to several mils over the desired finished rib height.

(7) Ribs and other areas such as end closures are machined to the desired height along with the plastic that remains in place.

(8) The mandrel is returned to the bath where the outer shell is electroplated (it is assumed that the plastic core material is somehow made conductive so electroplating can occur). Again, plating is in excess of finish dimensions to permit machine cleanup. Where additional thickness is required, as in the manifold and flange attach points, the chamber may be masked and returned to the bath for the additional nickel buildup only in the required areas, followed by machining to finish dimensions.

(9) The plastic core material is melted out through the inlet and outlet openings. Water will be flowed through each channel and the flow visually inspected to insure complete removal of the core material.

6.   Manifolds and Flanges

a.   Injector Attach Flange

The injector attach flange will be machined from plasma-arc cut T304L plate and machined leaving stock for machining the inside diameters to dimension after welding of the outlet manifold. Stock will also be provided for final machining of the injector interface after the flange and manifold assembly are welded to the chamber.

III, B, Fabrication Analysis (cont.)

      b.   Nozzle Extension Attach Flange

          The nozzle extension attach flange will be machined from a ring forging or a rolled and welded ring leaving stock for machining the interface surface after welding.

      c.   Manifolds

          The manifolds are designed to be welded from a basic half shell, which can be formed by several different methods. Drop hammer stamping, hydroforming or spinning could be employed with equally acceptable results. Costs would be approximately equal for any method; however, where only four pieces are to be made, spinning has an advantage of saving a machining operation in that the trim of the outer diameter and the weld chamfer can be made immediately after the spinning operation, while the part is on the spinning die.

          The fabrication procedure for the inlet manifold is typical and is illustrated below:

      (1) Form half shells.

      (2) Finish trim and chamfer outer diameter, rough trim inner diameter.

      (3) TIG weld outer joint using T349 weld wire and gas backup.

      (4) Cut hole for inlet ducts.

      (5) Weld inlet ducts to manifold.

      (6) Machine trim manifold assembly to fit chamber with maximum clearance of 0.004 in.

III, B, Fabrication Analysis (cont.)

7. Final Assembly and Test

a. Electron Beam Welding

(1) Weld Joint Design

There are two important criteria in designing for butt welding for the electron beam method. It is necessary to provide a good fit-up and desirable to provide a backup in which to allow the beam to decay. Where a butt weld is made without filler wire, clearance must be held to a minimum to prevent the distortion that will occur when the two edges are pulled together by shrinkage of the weld.

To obtain a satisfactory weld and minimize distortion, weld joint clearance will be held to 0.004 in. maximum. To ensure this maximum clearance, the matching diameters must be dimensioned with a nominal clearance of 0.002 in. with a diametrical tolerance of ± 0.002 in. on each dimension. These tolerances are not impossible to hold; however, they are expensive and an error resulting in excessive clearance could result in a poor weld joint and distortions. For this reason, it is expeditious in this program to delay the machining of the attaching components until the chamber machining is complete, then machine to fit. This plan permits, in effect, a doubling of tolerance from ± 0.002 in. to ± 0.004 in. on the outer member, and allows a standard tolerance of ± 0.010 in. on the chamber outside diameter interfaces rather than ± 0.002 in.

Backup has been provided for all EB welds where feasible by designing shoulders in the joint. Joints that cannot be backed up or welded from both sides can be through welded, if desired, or the weld can be controlled for only partial penetration. Through welding leaves a rough

III, B, Fabrication Analysis (cont.)

concave surface in the underside of the weld, and in some cases, involves the
danger of the beam crossing the gap and causing undesired melting on the next
wall. Electron beam welds with only partial penetration are objectionable
only in that they do not make a 100% joint. Both through welds and incomplete
penetration welds leave stress risers that are objectionable in many applica-
tions. The thrust chamber has been designed to avoid any through or incom-
plete penetration welds.

(2) Nozzle Extension Flange to Chamber

This joint, illustrated in Figure 26, will be made
by welding from both sides with an overlap from 1/8 to 1/4 in. in the center
of the joint.

(3) Inlet Manifold Assembly to Chamber

To assemble the inlet manifold from the injector
end, the upper weld joint interface cannot be oriented other than parallel
to the chamber axis. At this angle, the welding head cannot be positioned to
focus the beam parallel to the joint due to interference of the upper chamber
wall. Thus, it will be necessary to make the weld at a slight angle across
the joint. To ensure adequate coverage, two overlapping welds will be used.
(This joint and weld configuration is illustrated in Figure 24.) The lower
joint is self-locating and easily accessible.

(4) Outlet Manifold Assembly to Chamber

Both the upper and lower joints have sufficient
material behind the joint for backup of the electron beam. The joints are
self-locating requiring no tack-welding, and are easily accessible as shown in
Figure 25A. The electron beam welding is planned for the Azusa welding facility.
Equipment available there is a Sciaky 60KV Electron Beam Welder with a vacuum
chamber capable of handling cylindrical parts up to 44.0 in. dia and 30 in.

CHAMBER ₵

E.B. WELD

E.B. WELD
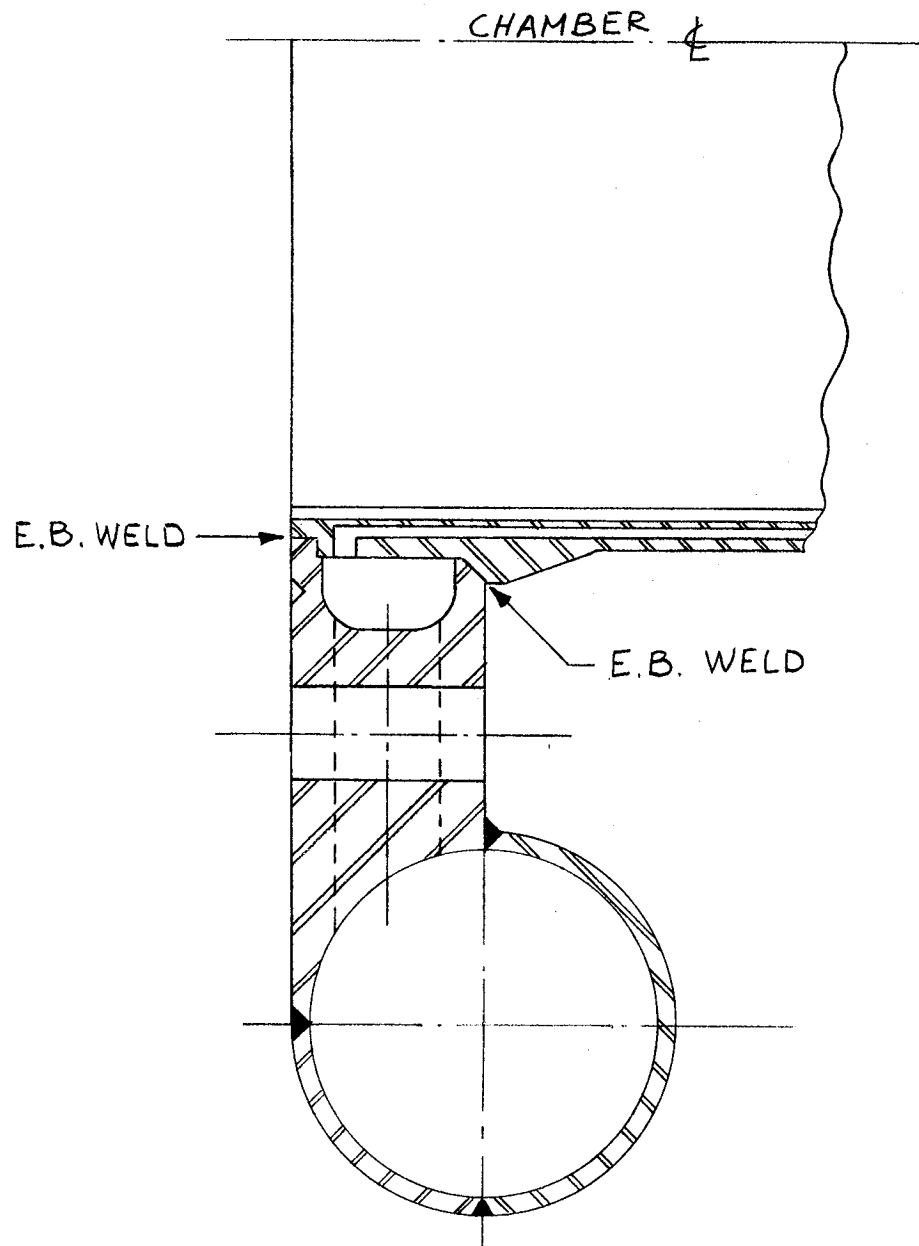
Figure 25A.   Joint Design of the Outlet Manifold
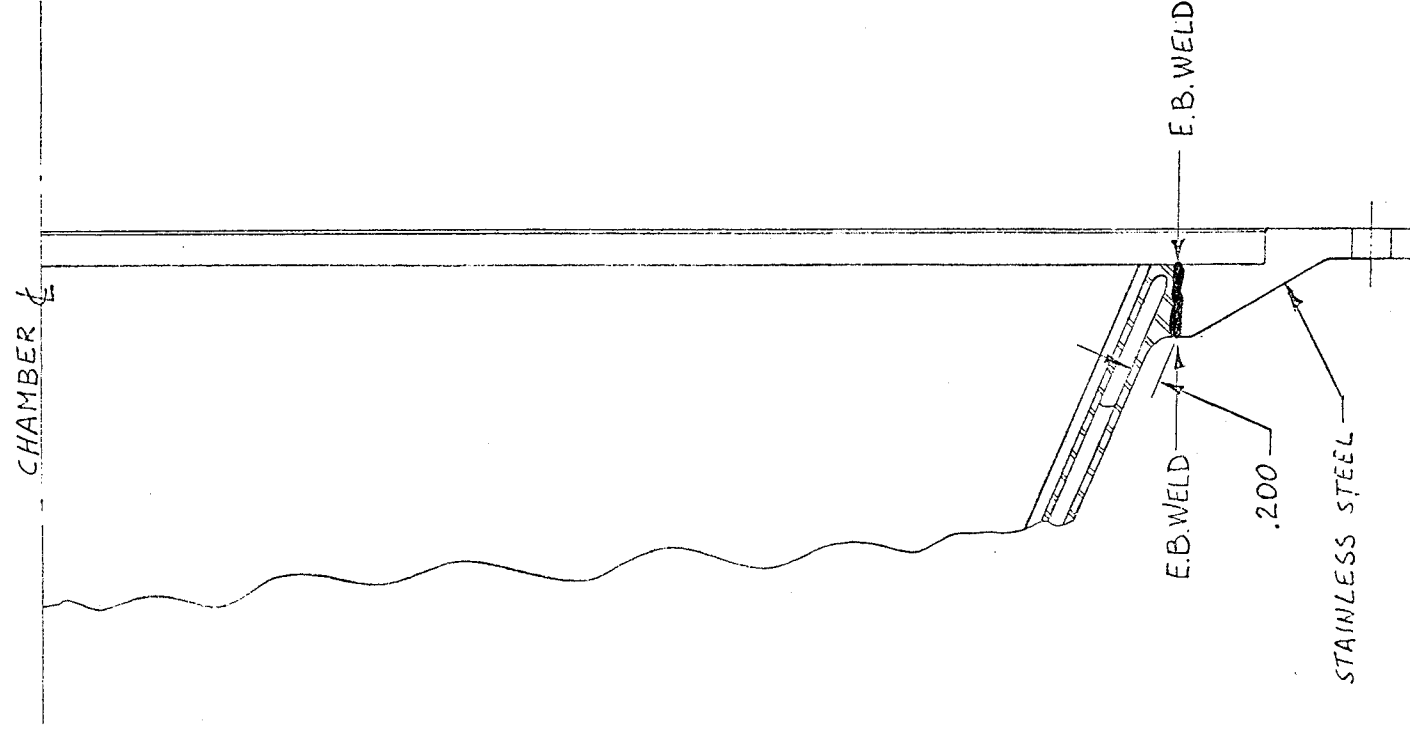
Figure 26. Weld Joint – Manifold to Chamber

III, B, Fabrication Analysis (cont.)

high. This joint, illustrated in Figure 26, will be made by welding from both
sides with an overlap from 1/8 to 1/4 in. in the center of the joint.
Figure 27 shows a circumferential weld in a cylindrical shape assembly
approximately the size of the subject thrust chamber. The view shown is
inside the vacuum chamber.

8.   Process Plan – Electron Beam Welding

The following operations are planned for accomplishing the
electron beam welding required:

a.   Establish preliminary weld schedules for each joint. The
welding parameters are listed on the sample Electron Beam Welding Parameters
sheet, Figure 28.

b.   Verify the settings with practice specimens.

c.   Clean all interfaces with MEK followed by methyl alcohol.

d.   Position and clamp the thrust chamber to the rotary fix-
ture with injector end up and with the nozzle extension attach flange positioned
flush with the chamber exit end. Position the welding head for the upper joint
and set machine to proper welding parameters.

e.   Evacuate chamber and weld.

f.   Assemble the inlet manifold to the thrust chamber. Posi-
tion the welding head and set the machine to the selected welding parameters.

g.   Evacuate the chamber and weld first pass.

h.   Reposition head and weld second pass.
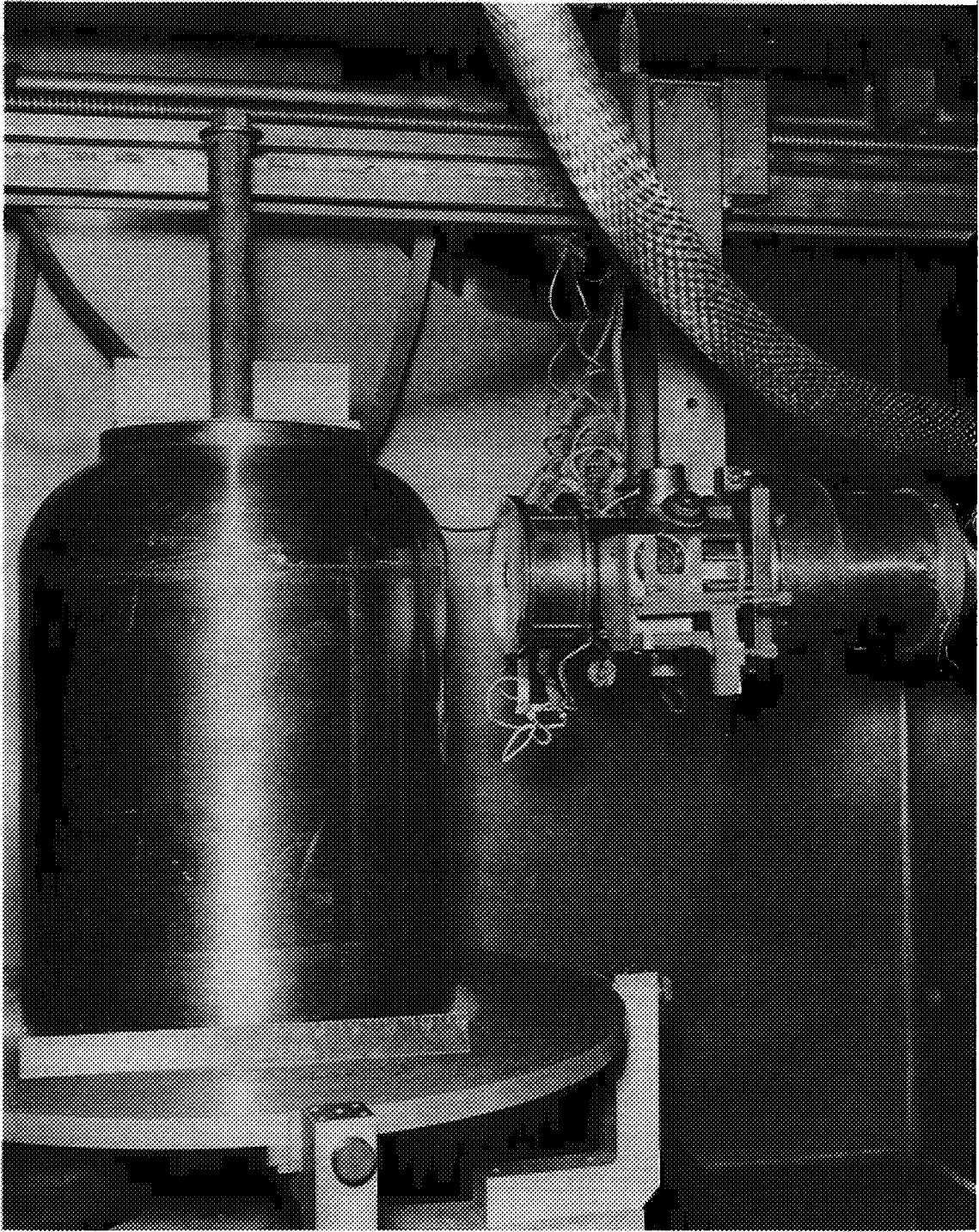
Figure 27. Circumferential Joint by EB Welding

ELECTRON BEAM WELDING PARAMETERS

Test No.	Weld Matl Depth	Matl Type	Joint Type	Gun to Work	Beam Current MA	Voltage KV	Focus Current	Filam. Current	Speed I.P.M.	Filam Size	Fil. to Cath Dist.	Anode to Cath.	Gun Type	Remarks

Figure 28. Electron Beam Welding Parameters

III, B, Fabrication Analysis (cont.)

i.   Assemble the outlet manifold assembly to the chamber. Position the welding head for the upper joint. Set the machine to the selected welding parameters.

j.   Evacuate the chamber and weld.

k.   Reposition the thrust chamber on the rotary table with the injector end down. Position the welding head for the lower nozzle extension attach flange joint. Set the machine to the selected welding parameters.

l.   Evacuate the chamber and weld.

m.   Position the welding head for the lower inlet manifold joint. Set the machine for the selected welding parameters.

n.   Evacuate the chamber and weld.

o.   Position the welding head for the lower outlet manifold assembly joint. Set the machine to the selected welding parameter.

p.   Evacuate the chamber and weld.

(1) Final Machining

After all welding operations are complete, the injector attach flange and the nozzle extension attach flange will be machined to dimension normal to the axis. The gasket seal grooves will also be machined at this time.

III, B, Fabrication Analysis (cont.)

(2) Leak and Flow Test

Leak and flow testing will be done with water at pressures and flow rates called out on the final assembly drawing. Pressure drop will be recorded and K_w values will be calculated. Vacuum dehydrating will follow testing.

(3) Thermal Shock Test

This test consists of introducing liquid nitrogen into the chamber at a flow rate to simulate cold start transient conditions. The test parameters and instrumentation requirements are as follows:

(a) Test Media   – LN_2

(b) Inlet Pressure   – 760 psia

(c) Flow Rate   – 15 lb/sec

(d) Duration   – 5 sec

(e) Initial Conditions – Ambient

(f) Instrumentation   – Thermocouples three places on chamber and at inlet and outlet connections.

(g) Monitor flow rate and inlet and outlet pressure.

(4) Final Inspection

Inspect for evidence of deterioration of bond-nickel to thermal barrier and thermal barrier to flame liner. Inspection will be visual and by the ultrasonic method using a facsimile recorder.

III, B, Fabrication Analysis (cont.)

(5) Nozzle Extension

The ablative nozzle extension requires conventional and proven fabrication steps only. The materials used and the method of manufacture are the same as used in tactical programs such as the Minuteman and in numerous experimental programs for liquid and solid engines.

The inner flame liner consists of a carbon-reinforced-phenolic prepreg that will be tape wrapped on a steel mandrel on an Edwards Tape Wrapping Machine (or equivalent) with an orientation parallel to the extension centerline. The tape will be heated and roller pressure applied during wrapping to obtain a high as-wrapped density. After a debulk cycle, the OD of the liner will be machined to required size. A coat of resin will be applied to the OD and silica-reinforced phenolic will be tape wrapped over the inner liner in an orientation essentially parallel to the liner outer surface. Extra material will be overwrapped at the forward end.

This composite structure will be cured in a hydroclave at a pressure of 1000 psig and a temperature of 300°F for a minimum of four hours. Following cure, the OD of the extension will be machined to size. The stainless steel flange, which could be machined from a forging or from a weldment, will be attached to the extension by adhesive. After cure of the adhesive, the OD of the flange sleeve and a portion of the extension downstream of the flange will be resin-primed and phenolic impregnated glass cloth will be laid up and roving will be wound under tensile over the flange and extending downstream of the flange for about 5 inches.

Following curing of the glass cloth and roving, the ends of the extension will be machined, including the O-ring groove at the forward end. The tag ends of the extension will be used to verify satisfactory cure and density of the carbon and silica reinforced phenolics. Strict control of raw material, tape wrapping, and curing procedures will be applied.

III, Task I--Design and Analysis (cont.)

C. HEAT TRANSFER ANALYSIS

1. Introduction

The purpose of this portion of the Design and Analysis task
is to establish the coolant channel and instrumentation designs and the thermal
barrier requirements for the regeneratively cooled portion of the chamber and
to provide temperature and heat flux data necessary to select and size the
materials to be employed in the ablative cooled nozzle expansion region.

2. Preliminary Studies

Prior to beginning the design study, preliminary studies were
performed to establish the gas-side and coolant-side boundary conditions, the
radiation heat flux from the propellant gases and the method to be employed
for pressure drop calculations. The gas-side studies were required for this
propellant system because the high fluorine/hydrogen gas temperatures and pos-
sible recombination effects are not accounted for with existing design
correlations.

a. Gas-Side Convective Boundary Conditions

(1) Gas-Side Film Coefficient State of Art

At Aerojet, calculations of the gas-side film coeffi-
cient are generally made by using a pipe flow type of correlations; usually the
simplified Bartz equation (Ref 13). This equation, which was derived semi-
empirically, has been used successfully both at Aerojet and throughout the
industry to calculate the film coefficient in the throat and expansion regions
of thrust chambers, provided low or intermediate energy propellants (e.g.,
N_2O_4/AeroZINE 50, LO_2/LH_2, etc.) were employed and the effects of

III, C, Heat Transfer Analysis (cont.)

two-dimensional gas flow in the expansion region of the chamber were included in the calculations. In the combustion chamber region, film coefficients predicted by the Bartz equation were found to be lower than measured coefficients; sometimes as much as a factor of two. This was attributed to "injector streaking"* and the generally higher turbulence level encountered in the chamber region. This difficulty was overcome by employing empirically determined multiplying factors which were applied to the Bartz equation for chamber region calculations. This procedure was adequate for design with most chambers and propellant systems encountered.

More recent chamber development programs with low thrust, low pressure systems, very high pressure systems and systems employing high energy, high gas temperature propellants have indicated the presence of other effects, such as laminarization at low Reynolds numbers and surface roughness effects at high Reynolds numbers, that are not predicted by the Bartz equation**. Since fluorine/hydrogen is a high energy propellant system, the effects which occur with this category of propellants are of particular interest to the current design study.

(2) Heating Effects with High Energy Propellants

The higher gas temperatures encountered with high energy propellants produce larger temperature gradients in the cooled boundary layer, which results in larger thermal property variations than are found with low energy propellant systems. For this reason it can be concluded that a correlation which was derived from low energy propellant data, such as the Bartz equation, cannot be employed for high energy propellants. The very high

*Local chamber region anomalies such as mixture ratio variations which result in hot-spots are termed "injector streaking". These effects generally vary both circumferentially and axially in the combustion chamber region.
**A discussion of these effects and the current effort at Aerojet to develop design correlations which include them, is given in Reference 14.

III, C, Heat Transfer Analysis (cont.)

gas temperatures which occur with fluorine/hydrogen and other high energy
propellants, can also produce appreciable dissociation of the hot gas molecules,
which may then recombine in the cooled boundary layer or at the chamber wall
with the production of heat. This heating effect will be in addition to the
normal convective heating of the wall. Molecular and atomic hydrogen and
atomic fluorine, which can recombine, are present in the fluorine/hydrogen
combustion gases, as shown in Table VII.

TABLE VII

CHEMICAL COMPOSITION OF FLUORINE/HYDROGEN
GAS AT NOMINAL DESIGN CONDITIONS

Chamber Pressure, psia	400
Mixture Ratio	12.0
Stagnation Temperature, °R	7654
Energy Release Efficiency (assumed)	98%

Chemical Specie	Mole Fraction
HF	0.6746
H_2	0.1318
H	0.1654
F_2	0.0000
F	0.0281

Thrust chamber test data obtained with gox/heptane (Ref 15) have shown that
the heating effect attributed to recombination was 45% of the convective heat
flux. Estimates based on fluorine/hydrogen chamber test data (Ref 16) indi-
cate that recombination effects may be even greater with these propellants,
and will vary with chamber location and chamber pressure.

III, C, Heat Transfer Analysis (cont.)

(3) Prediction of Fluorine/Hydrogen Heat Flux

A pipe flow type of correlation similar to the form recommended by Eckert (Ref 17) for predicting both convective heat transfer rates and recombination effects, has been selected for the design study. In this method, enthalpies are used as the thermal driving potential between the hot gas and the cooled chamber wall. The convective heat flux is calculated using Equation (1).

$$q_c = h_{gi} (i_r - i_w) \qquad \text{(Eq 1)}$$

where

q_c = convective heat flux

h_{gi} = heat transfer coefficient

i_r = recovery enthalpy

i_w = enthalpy at wall temperature and pressure

The heat transfer coefficient is calculated by the following equation:

$$h_{gi} = \frac{C_g}{Re*^{0.2} Pr*^{0.6}} \rho V \left| \frac{T_s}{T*} \right. \qquad \text{(Eq 2)}$$

The correlation constant, C_g, has been determined empirically and varies with chamber location. This variation accounts for higher than pipe flow fluxes in the combustion chamber region due to injector effects, and lower than pipe flow fluxes in the throat, which are attributed to acceleration and pressure gradient effects. The gas mass velocity term, ρV, and static temperature, T_s, are calculated from two-dimensional flow theory in the expansion region of the nozzle where these values deviate from one-dimensional flow values.

III, C, Heat Transfer Analysis (cont.)

The thermal properties employed in Equation (2) are evaluated at the Eckert reference enthalpy which is given by Equation (3).

$$i^* = 0.5 \, (i_s + i_w) + 0.22 \, Pr^{*1/3}(i_o - i_s) \quad \text{(Eq 3)}$$

The recovery enthalpy is calculated using Equation (4). The stream and stagnation enthalpies used in this equation are based on an assumed 98% energy release efficiency in the combustion chamber.

$$i_r = i_s + Pr^{*1/3}(i_o - i_s) \quad \text{(Eq 4)}$$

The stream enthalpy is calculated assuming shifting equilibrium in the combustion chamber and throat and on frozen composition beyond area ratio 1.3 in the divergent nozzle where stream freezing is predicted to occur. The latter prediction is consistent with fluorine/hydrogen thrust chamber test data, such as Ref 18.

(4) Film Coefficient Correlation Constant

The heat transfer coefficient constant, C_g, was obtained from a recent Aerojet literature survey (Ref 14 and 19) and a limited amount of fluorine/hydrogen and lox/hydrogen test data. The Aerojet data indicate the range of C_g values shown in Table VIII.

TABLE VIII

EMPIRICAL HEAT TRANSFER COEFFICIENT
CORRELATION CONSTANT, C_g

Location	C_g
Combustion Chamber	0.016 to 0.032
Throat	0.011 to 0.019
Supersonic	0.019 to 0.026

III, C, Heat Transfer Analysis (cont.)

C_g values of 0.023 in the chamber, 0.015 at the throat and 0.023 in the super-sonic region were selected for the design study. These values are representa-tive of mean values for these chamber locations.

The heat transfer coefficient Equation (2) can be rewritten in terms of Stanton X Prandtl and Reynolds numbers as Equation (5).

$$St^* \ Pr^{*0.6} \ = \ C_g \ Re^{*-0.2} \qquad \qquad (Eq \ 5)$$

In this form the design heat transfer coefficients could be compared to the lox/hydrogen data of Ref 20 and a limited amount of fluorine/hydrogen data (Ref 16 and 18) at the throat and chamber regions. The design equations and curves showing the limits of the C_g data scatter are shown for the chamber region on Figure 29 and for the throat on Figure 30. The large scatter evi-dent in the chamber data might be attributed to injector effects. These effects apparently have decayed at the throat where there is less confusion in the data and better agreement with the correlation. The design equations are thought to give representative predictions of the coated chamber heat transfer coefficients, however, it should be emphasized that a good deal of uncertainty exists in these predictions, as is indicated by Table VIII and Figure 29.

      b.   Gas Radiation

Radiation from the HF molecule, the principal propellant gas specie, will account for a significant percentage of the heat flux incident on the chamber wall, particularly in the high pressure chamber region. This is due to the very high gas temperatures and the high emissivity of HF gas. The radiation heat flux was calculated using Equation (6), which is recommended by McAdams (Ref 21) for gas radiation to a black body.

Figure 29. Stanton X Prandtl Number vs Reynolds Number, Combustion Chamber Region
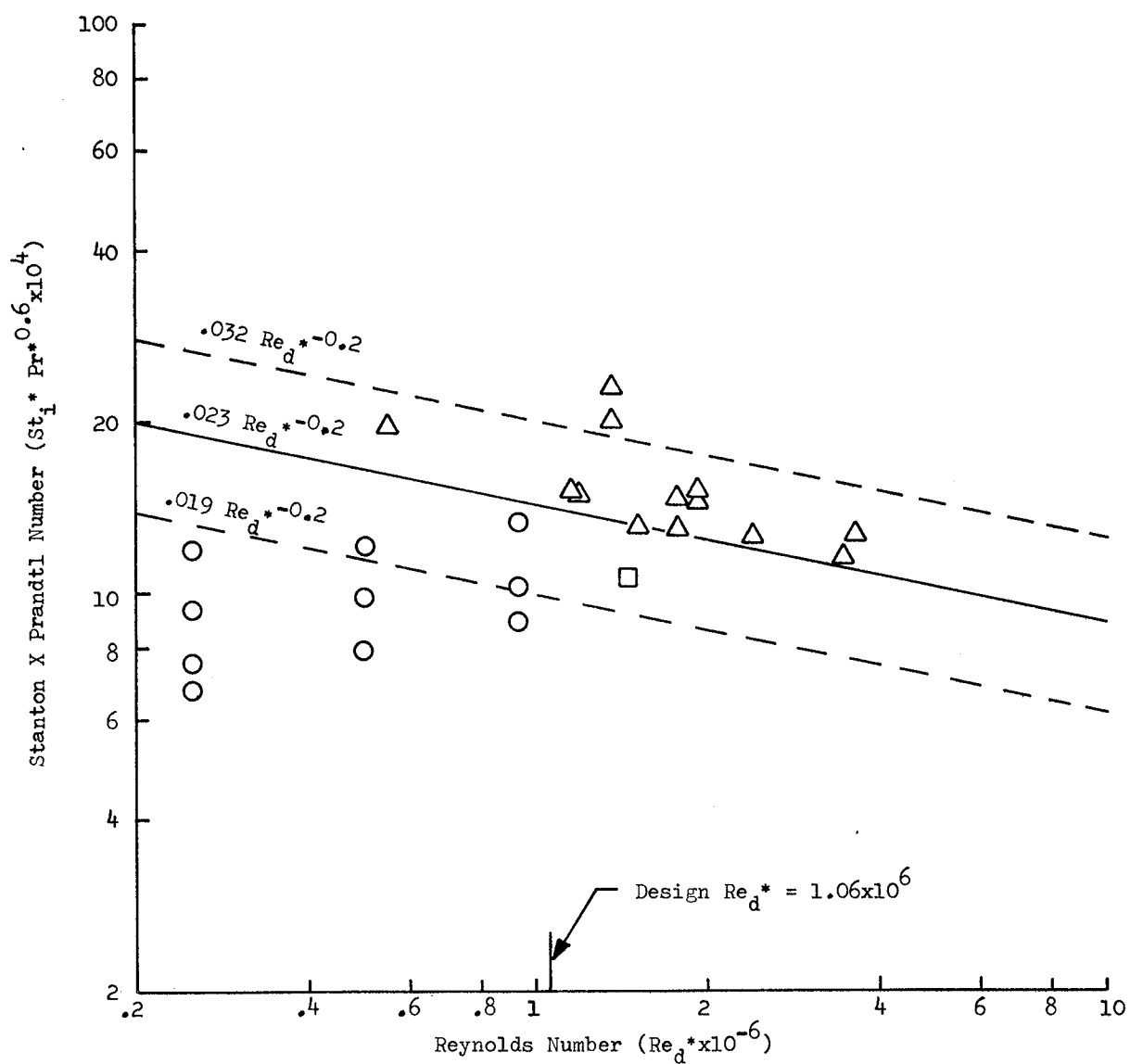
NOTES:

1. Properties evaluated at Eckert ref. enthalpy,

$$i* = 0.5 \, (i_s + i_w) + 0.22 \, (i_o - i_s)$$

2. St_i* based on enthalpy driving potential

LEGEND:

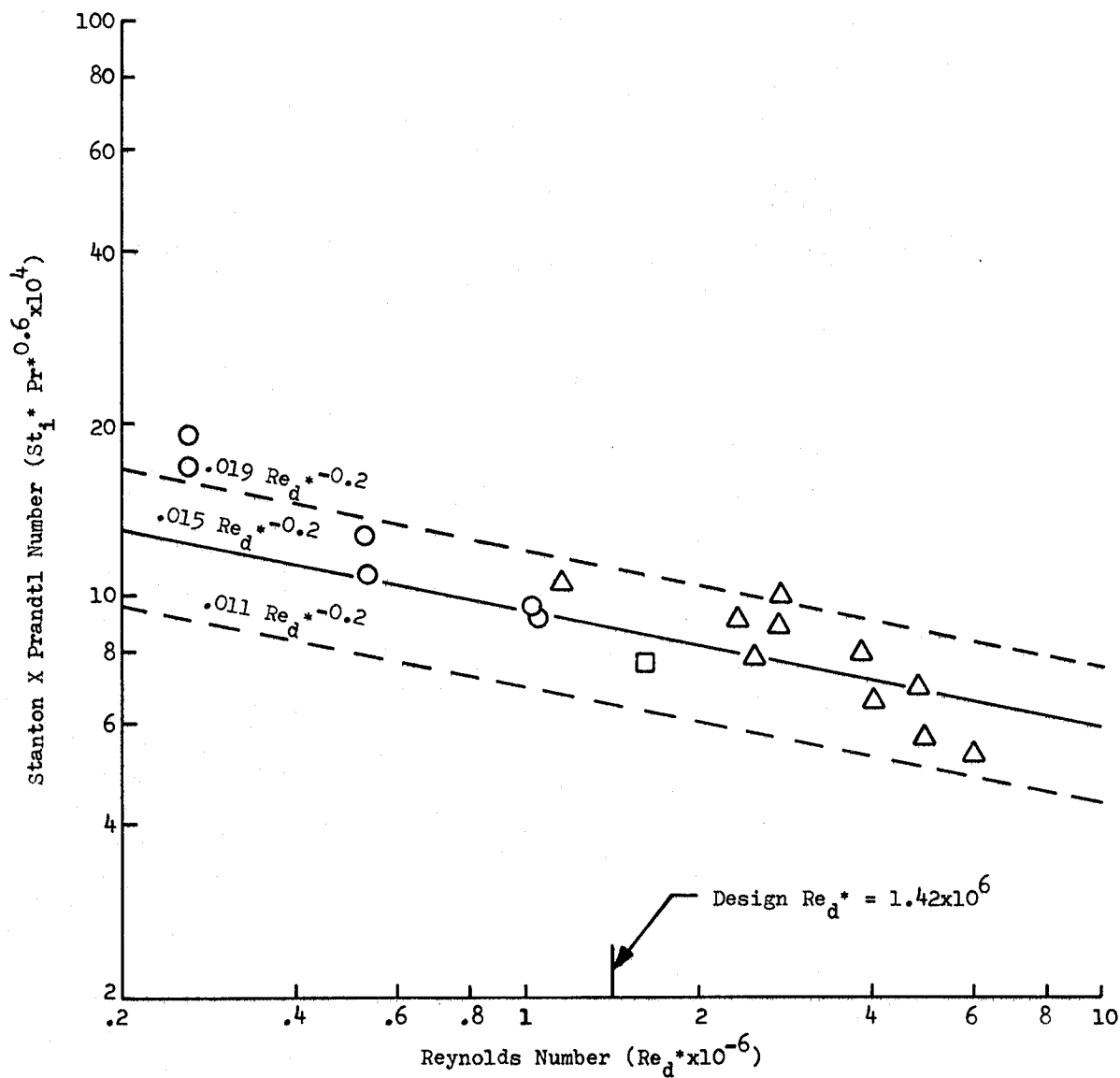$\triangle$ Ref.20, LO_2/LH_2

$\bigcirc$ Ref.16, LF_2/GH_2

$\square$ Ref.18, LF_2/LH_2

Figure 30. Stanton X Prandtl Number vs Reynolds Number at Throat

III, C, Heat Transfer Analysis (cont.)

$$(Q/A)_{RAD} = 3.3 \text{ Btu/sec-in.}^2 \times 10^{-15} (\varepsilon_s T_s^4 - \alpha_w T_w^4) \quad \text{(Eq 6)}$$

The HF emissivity and absorptivity employed in Equation 6 were calculated by
the method of Penner (Ref 22). The radiation heat flux is shown as a function
of chamber axial distance shown on Figure 31. The radiation heat flux in the
chamber region (approximately 1.0 Btu/in.2-sec) is 12% of the total flux.

    c.   Coolant Side Heat Transfer

        (1)   Convection Film Coefficient

           The convective heat transfer coefficient for super-
critical, cryogenic hydrogen has been successfully correlated over a wide range
of conditions for flow in circular, straight channels; however, the use of these
correlations is limited to rather narrow ranges of pressure, temperature and
heat flux or cooled wall temperature to bulk temperature ratio for bulk tempera-
tures below 200°R. This is attributed to the wide variation of the thermal
properties of hydrogen with pressure and temperature in this temperature range.
Above 200°R, the thermal properties are fairly well behaved functions of tem-
perature and exhibit only a moderate dependence on pressure. For this reason
correlations derived at temperatures above 200°R may be used without the restric-
tions which limit the use of the low temperature correlations. It was especially
important in this study to recognize the limitations of these correlations, since
the bulk temperature rise of the hydrogen coolant is in excess of 400°R. This
results in the hydrogen being present at both the lower and higher bulk tempera-
ture ranges in the coolant channels. Because of this large bulk temperature
variation, a single design correlation could not be employed throughout the
regeneratively cooled chamber.

           Two empirical forms of film coefficient correlation
have been selected for design, each being a check on the other, and with dif-
ferent correlations applying to different regions of the chamber according to
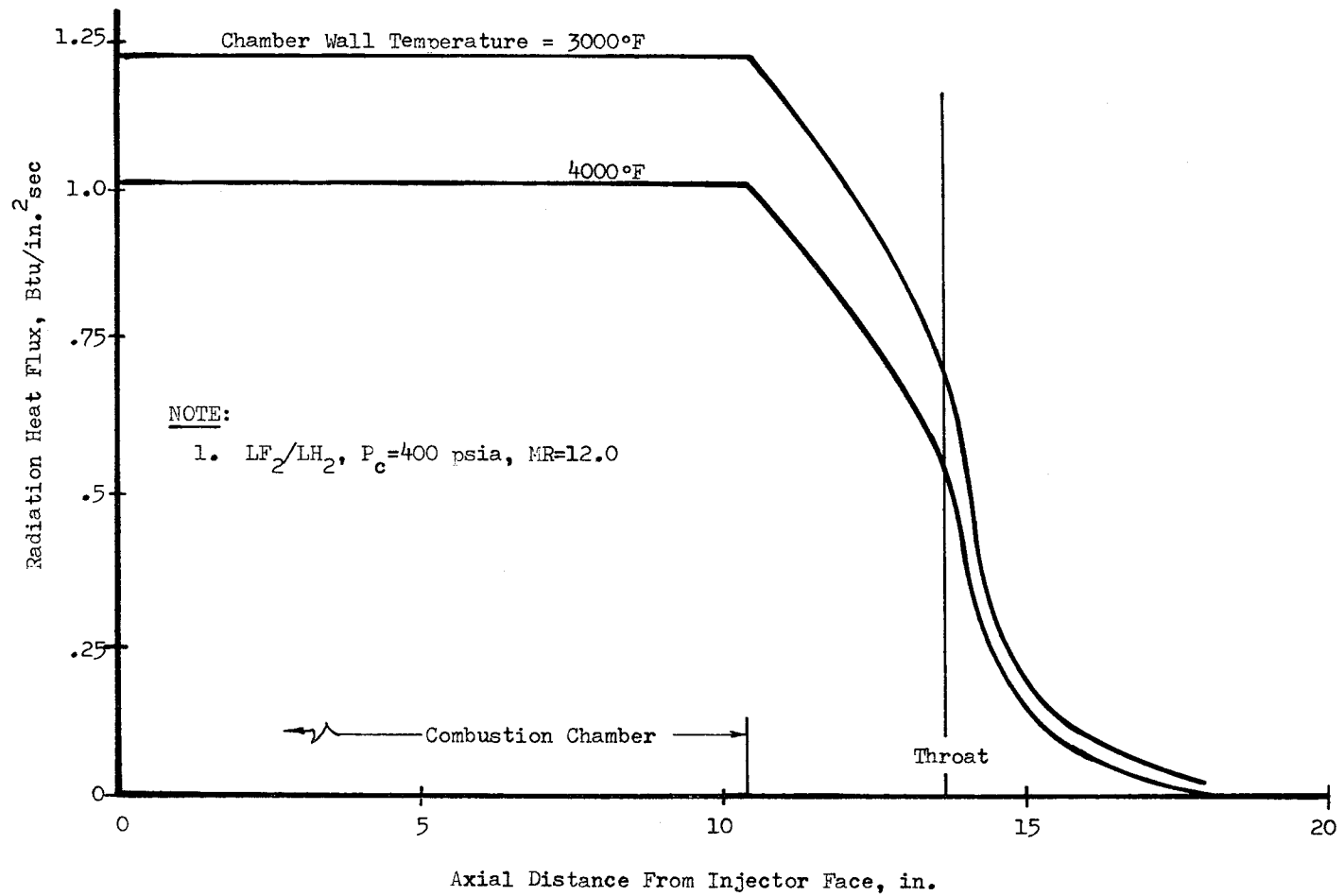the local coolant bulk temperature. One form employs bulk temperature thermal

Figure 31. HF Gas Radiation Heat Flux

III, C, Heat Transfer Analysis (cont.)

properties with a wall-to-bulk temperature ratio correlation term; the other is based on film temperature properties. The coolant-side design correlations with their chamber region of applicability are tabulated in Table IX.

(2) Film Coefficient Enhancement

Entrance effects attributed to boundary layer growth at the coolant entrance, promotion of turbulence at turns, and the presence of sudden contractions and expansions will enhance the coolant film coefficient, as will channel curvature at the throat and contraction regions of the chamber. Also, recent work on hydrogen convection at Aerojet (Ref 27) indicates that the low bulk temperature design correlations employed in the study (Equations 1 through 3, Table IX) predict film coefficients that are much lower (as much as a factor of 2.5) than measured film coefficients below approximately 100°R. These effects have been neglected in the design study which tends to make the cooling design conservative where these effects occur (i.e., low bulk temperature expansion region, throat, etc.). However, interpretation of channel wall temperature data obtained from test firings will require that these effects be included.

(3) Channel Geometry Effects

The design correlations tabulated in Table IX have been derived from data obtained for hydrogen flowing in straight, symmetrically heated, circular channels. Since the current design employs rectangular, asymmetrically heated channels some differences in the flow characteristics and film coefficients might be anticipated. Aerojet data (Ref 28) indicates that the hydrogen film coefficient obtained with flattened, asymmetrically heated tubes are higher than the coefficients for circular, symmetrically heated tubes. This seems to indicate that the round tube correlations employed in the design study will give conservative predictions of the chamber wall temperatures. These effects are best determined for hydrogen by correlating test data obtained

TABLE IX

COOLANT-SIDE DESIGN CORRELATIONS

Correlation Form: $Nu_{ref} = C_1 Re_{ref}^{0.8} Pr_{ref}^{0.4} \phi_1 \phi_2$

	Source	Reference Temperature	Correlation Constant, C_1	ϕ_1	ϕ_2	Range of T_w/T_b	Bulk Temp Range, °R	Chamber Design Application
1.	Thompson-Geery (Ref 23)	Bulk	0.028	$(T_w/T_b)^{-0.64}$	---	1.4 to 16.5	50 to 200	Coolant Inlet Region
2.	Thompson-Geery (Ref 23)	Bulk	0.0217	$(T_w/T_b)^{-0.34}$	---	1.4 to 16.5	50 to 200	Expansion Region
3.	Hess-Kunz (Ref 24)	Film	0.0208	---	$1+0.01457\, \upsilon_w/\upsilon_b$	---	50 to 200	Expansion Region
4.	McCarthy-Wolf (Ref 25)	Bulk	0.0250	$(T_w/T_b)^{-0.55}$	---	2.3 to 11.1	200 to 700	Throat and Chamber Region
5.	Taylor (Ref 26)	Film	0.021	---	---	---	200 to 700	Throat and Chamber Region

III, C, Heat Transfer Analysis (cont.)

with the rectangular, asymmetrically heated channels. The channel wall thermocouple instrumentation will provide data which may be used to estimate this effect.

Three-dimensional coolant flow effects, due to channel curvature at the throat and at the transition from the contraction region to the cylindrical chamber, will enhance the coolant film coefficient. Correlations have been derived for liquid hydrogen by Aerojet (Ref 28) and for gaseous hydrogen at Rocketdyne (Ref 36) which account for curvature effects with symmetrically heated round tubes. The gaseous hydrogen data indicate that this effect depended on the channel radius of curvature, the tube radius and the Reynolds number; an increase of the film coefficient by a factor of two or three with high Reynolds numbers and large curvature angles was noted. These data also show that the enhancement of the film coefficient persisted in the uncurved portion of the tube downstream of the curved tube zone. Again, the wall thermocouple test data will provide data which may be used to estimate these effects.

d. Coolant Pressure Drop

Friction Loss: Pressure drop due to wall friction was calculated using a rough channel friction factor correlation and an estimated wall roughness of 64 micro-inches. Rough channel friction factor correlation is as follows:

$$f = 0.001375 \left[1 + \left(2 \times 10^4 \ \frac{E}{De} + \frac{1 \times 10^6}{Re_b} \right)^{\frac{1}{3}} \right]$$

where

  f: friction factor
  E: channel roughness, inch
  De: channel equivalent diameter, inch (= 4 flow area ÷ wetted perimeter)
  Re_b: Reynolds Number – bulk coolant properties

III, C, Heat Transfer Analysis (cont.)

This is an approximate form of the Colebrook equation with an accuracy of $\pm 5\%$ for $4 \times 10^3 \le Re_b \le 1 \times 10^7$. The frictional pressure drop is then calculated,

$$\Delta P_{friction} = \frac{2\bar{f}_1 \, P_F}{\overline{De}} \cdot \frac{\overline{\rho B} \, \bar{V}_L{}^2}{144 \, g}$$

    1: channel length, in.

    ρB: bulk density, lb/ft^3

    V_L: Coolant velocity, ft/sec

    g: 32.2 ft/sec^2

    P_F: constant, taken as 1.3 in study.

    Bar (—) denotes average values between stations, n and n+1; i.e.,

    $\bar{f} = 1/2(fn + fn + 1)$

        Aerojet test experience (Ref 29) with hydrogen flowing in formed tubing has shown that the non-isothermal friction factor for super-critical hydrogen is greater than the value predicted by rough tube correlations by an average of 30%. This is attributed to variations of the velocity profile due to property variations that are present with non-isothermal hydrogen flow. These effects are not accounted for by correlations based on incompressible fluid data. A multiplying factor of 1.3 was applied to the rough tube correlation to account for this effect.

        (1) Form Losses: Sudden contraction and expansion, turned-around losses, and turbulence losses due to channel curvature were included in the coolant pressure drop calculations. The correlation recommended by Ito (Ref 30) for curved tube friction factor was employed to calculate channel curvature losses. The other form losses were calculated according to the form loss data given in Vennard (Ref 31).

III, C, Heat Transfer Analysis (cont.)

Ito's correlation for channel curvature losses,

$$\frac{f\ curved}{f\ straight} = \left[Re_b \left(\frac{ro}{R} \right)^2 \right]^{\frac{1}{20}}$$

where

R: channel radius of curvature

ro: radius of circular cross-section of channel (taken as 1/2 De in study

Vennard form loss data,

(1) Sudden enlargements calculated as,

$$\Delta P - \bar{\rho} B \frac{(V_1 - V_2)^2}{288_g}$$

where

V_1: velocity in approach section, ft/sec

V_2: downstream velocity

(2) Sudden contraction calculated as,

$$P = K_L\ \bar{\rho} B \frac{V_2^2}{288g}$$

K_L: A function of channel contraction ratio given on page 216 of Vennard as follows,

A_2/A_1	0	0.1	0.2	0.3	0.4	0.5	0.6	0.7	0.8	0.9	1.0
K_L	0.50	0.46	0.41	0.36	0.30	0.24	0.18	0.12	0.06	0.02	0

III, C, Heat Transfer Analysis (cont.)

(2) Momentum Loss: Changes of coolant pressure to dynamic heat due to heating pressure losses, and changes in channel flow area were included in the momentum pressure drop calculations.

(3) Wall Material Thermal Properties: The thermal properties of vapor-deposited tungsten and electroformed nickel were obtained from the data of Refs 32 through 35 for pure tungsten and nickel. These data are plotted as smooth curves on Figures 32 and 33. The properties of the tungsten-zirconia coating materials are given in Table X and Figure 10.
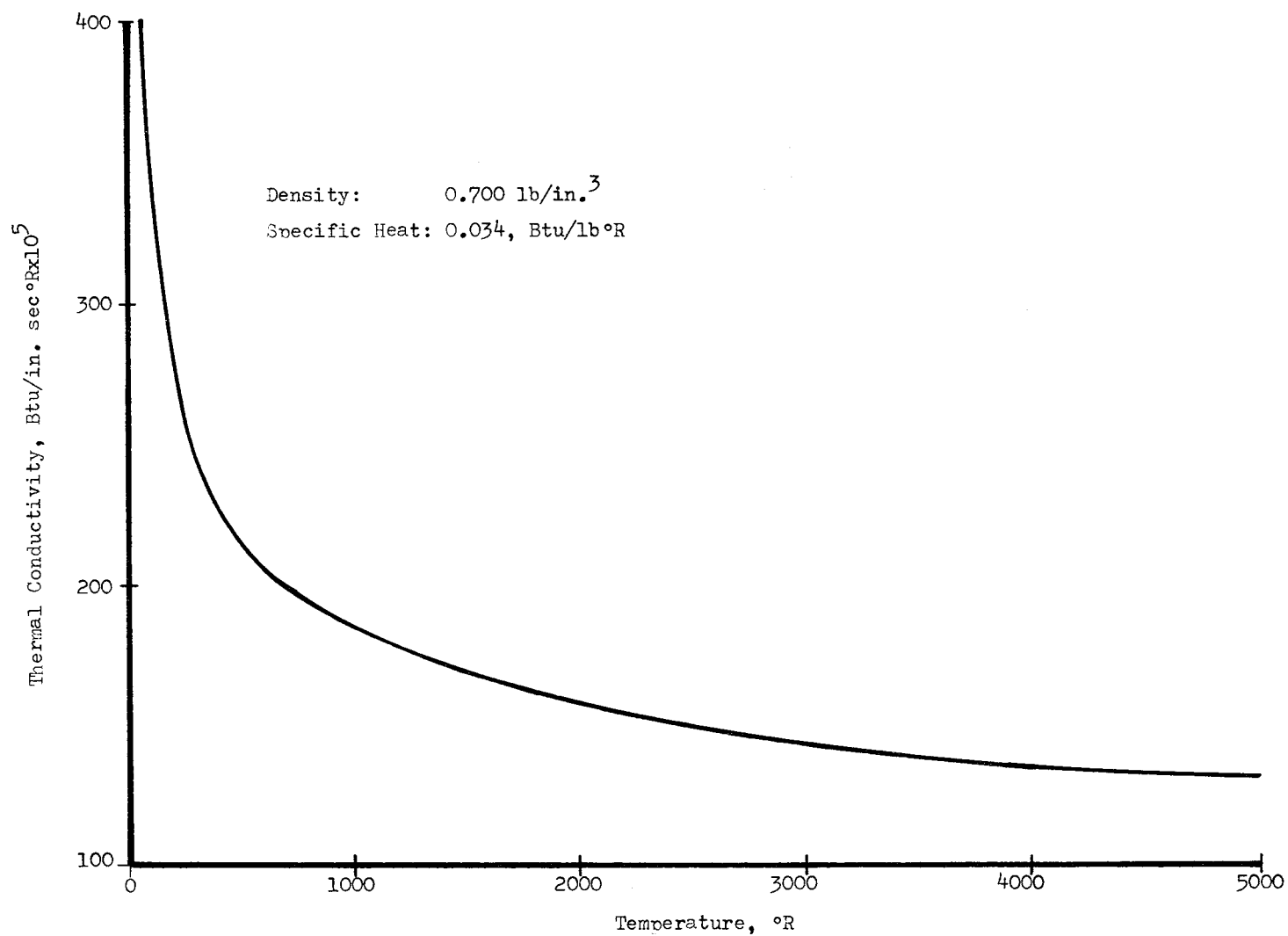
Figure 32. Thermal Properties of Tungsten

Figure 33. Thermal Properties of Nickel
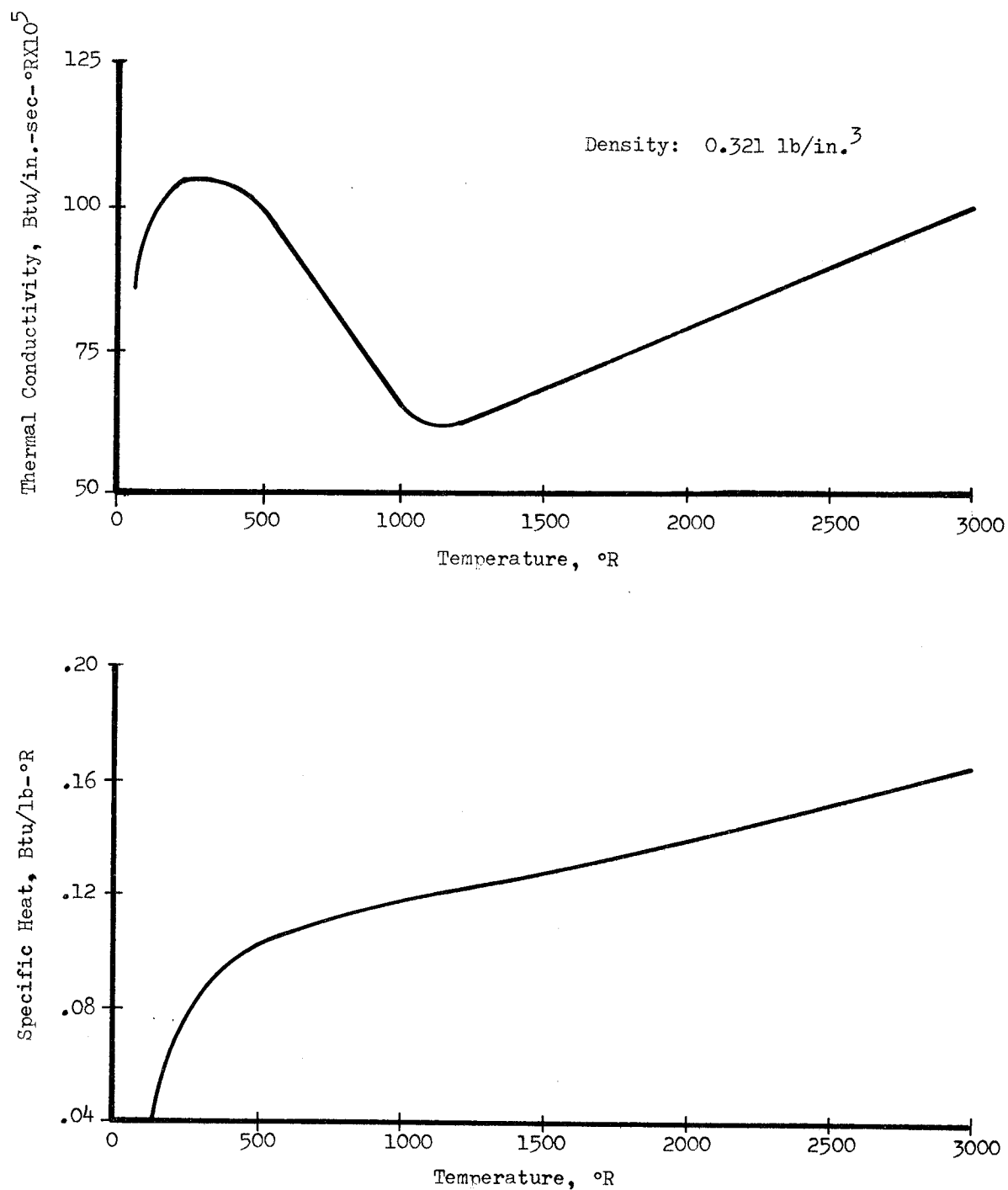
TABLE X

DENSITY, SPECIFIC HEAT AND THERMAL DIFFUSIVITY
OF FLAME-SPRAYED TUNGSTEN-ZIRCONIA COMPONENTS

Material	Density*, lb/in.^{3}	Specific Heat, Btu/lb-°F	Thermal Diffusivity, in.^{2}-sec
$88W-12ZrO_2$	0.532	0.035	0.0086
$75W-25ZrO_2$	0.490	0.039	0.0051
$50W-50ZrO_2$	0.385	0.049	0.0030

*Assumes 85% of theoretical density

III, C, Heat Transfer Analysis (cont.)

3. Design Study Results

a. Regeneratively Cooled Section Design

Local channel dimensions were designed to provide suffi-cient hydrogen cooling to maintain the coating and channel wall temperatures at reasonable values without excessive coolant pressure drop. The nickel land size and configuration was designed to be consistent with these requirements, to provide strength, and to insure ease of fabrication. The channel design provides for two coolant passes in the nozzle from area ratio 6:1. This permits preheating of the low temperature hydrogen, which is a relatively poor coolant, in the low heat flux region while maintaining reasonable coolant velocities and wall temperatures. After passing through the two-pass region, the hydrogen flows through the high heat flux throat and combustion chamber zones in a single-pass and enters the collection manifold at the injector end of the chamber. The coating thermal resistance will be tapered from the coolant inlet to the throat. The channel and coating thermal resistance designs are summarized on Table XI. The coated channel cross-section and temperatures at the throat are shown on Figure 34.

The predicted, steady-state chamber operating parameters for hydrogen regenerative cooling are given on Table XII and on Figures 35, 36, and 37. The nickel wall temperature curves shown on Figure 35, are the best estimates which were obtained by interpolating from the curves derived using different coolant-side film correlations, and also included are the effects of two-dimensional heat transfer. The nickel wall temperatures pre-dicted with film and bulk temperature correlations are compared in Table XIII.

TABLE XI

CHANNEL AND COATING RESISTANCE DESIGN SUMMARY

Area Ratio	Axial Distance	Flow Channels	Total Channels	Channel Width	Channel Height	Land Width	Coating Resistance
6.00	19.13	48	144	0.122	0.0777	.090	1000
10.58	22.13			0.190	0.0885		
16.00	25.38	48		0.254	0.1000		
16.00	25.38	96		0.254	0.1000		
10.58	22.13			0.190	0.1885		
6.00	19.13	96	144	0.122	0.0777		
6.00	19.13	96	96	0.230	0.0777		1000
3.83	17.53			0.167	0.0720		
2.12	16.05			0.103	0.0667		
1.97	15.58	96	96	0.097	0.0639		
1.97	15.58	48	48	0.281	0.0639		Linear Taper
1.15	14.83			0.197	0.0620		
1.03	14.43			0.182	0.0608		
1.00	14.13			0.178	0.0600		425
-1.03	13.73			0.182	0.0630		
-1.05	13.48			0.184	0.0645		
-1.45	12.38	48	48	0.230	0.0709	.090	
-1.45	12.38	96	96	0.095	0.0709	0.090 & 0.040	
-1.69	11.68			0.108	0.0749	0.090 & 0.040	
-1.69	11.68			0.095	0.0749	0.090 & 0.065	
-1.97	10.80			0.108	0.0800	0.090 & 0.065	
-1.97	0-10.80	96	96	0.096	0.0800	0.090	425
-	Inch	-	-	Inch	Inch	Inch	$\dfrac{in.^2 sec-°R}{Btu}$
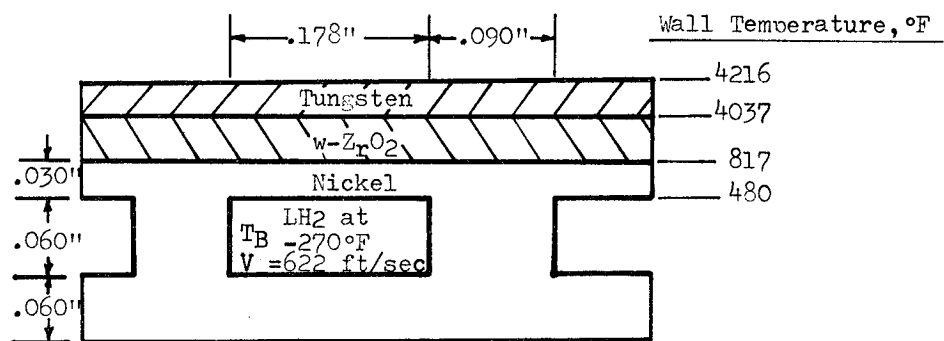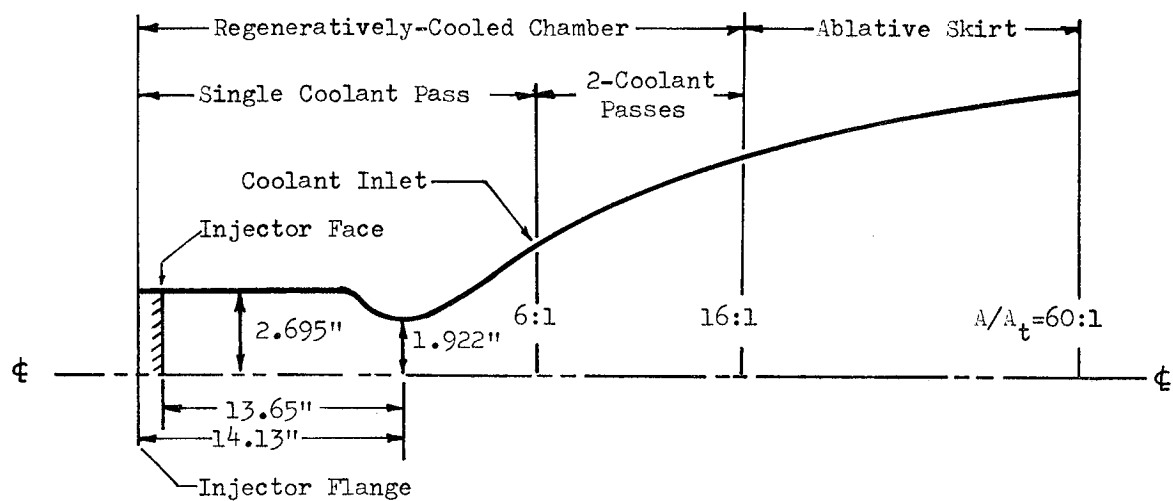
Figure 34. Chamber Wall Cross-Section at Throat
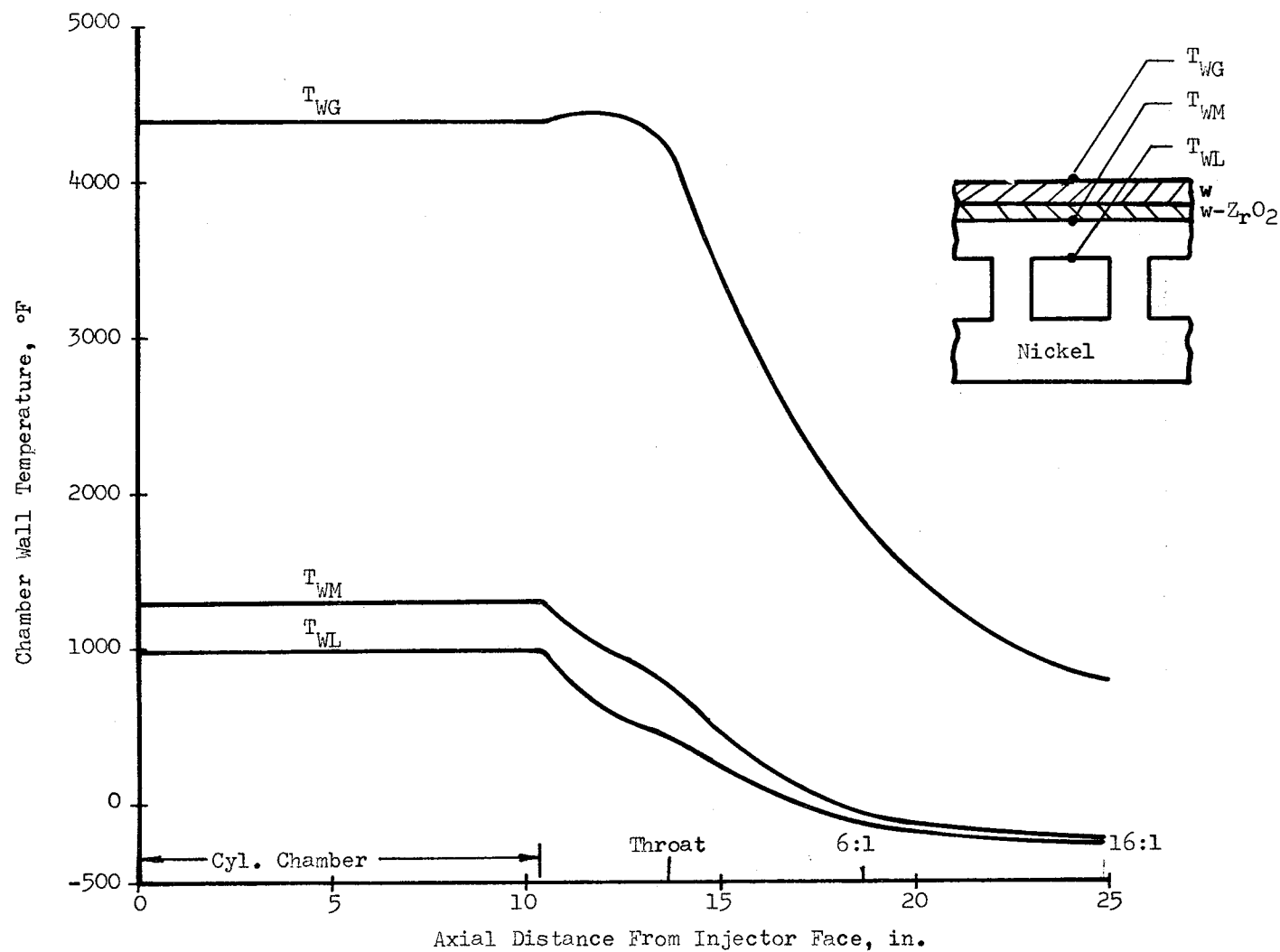
Figure 35. Steady-State Chamber Wall Temperatures
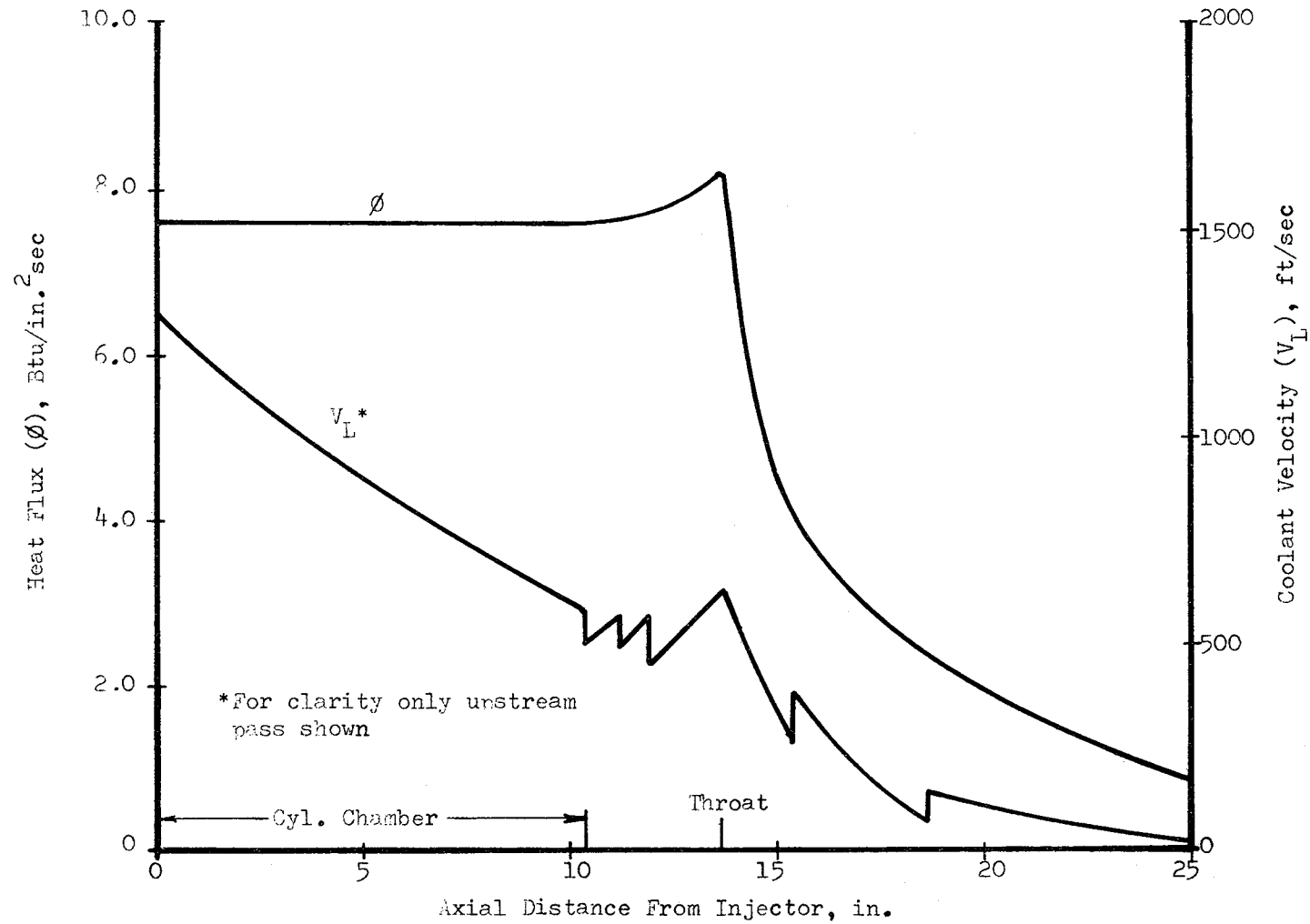
Figure 36. Steady-State Chamber Heat Flux and Hydrogen
Coolant Velocity

NOTE:

1. Hydrogen Inlet Conditions:
   P_B=760 psia, T_B=50°R
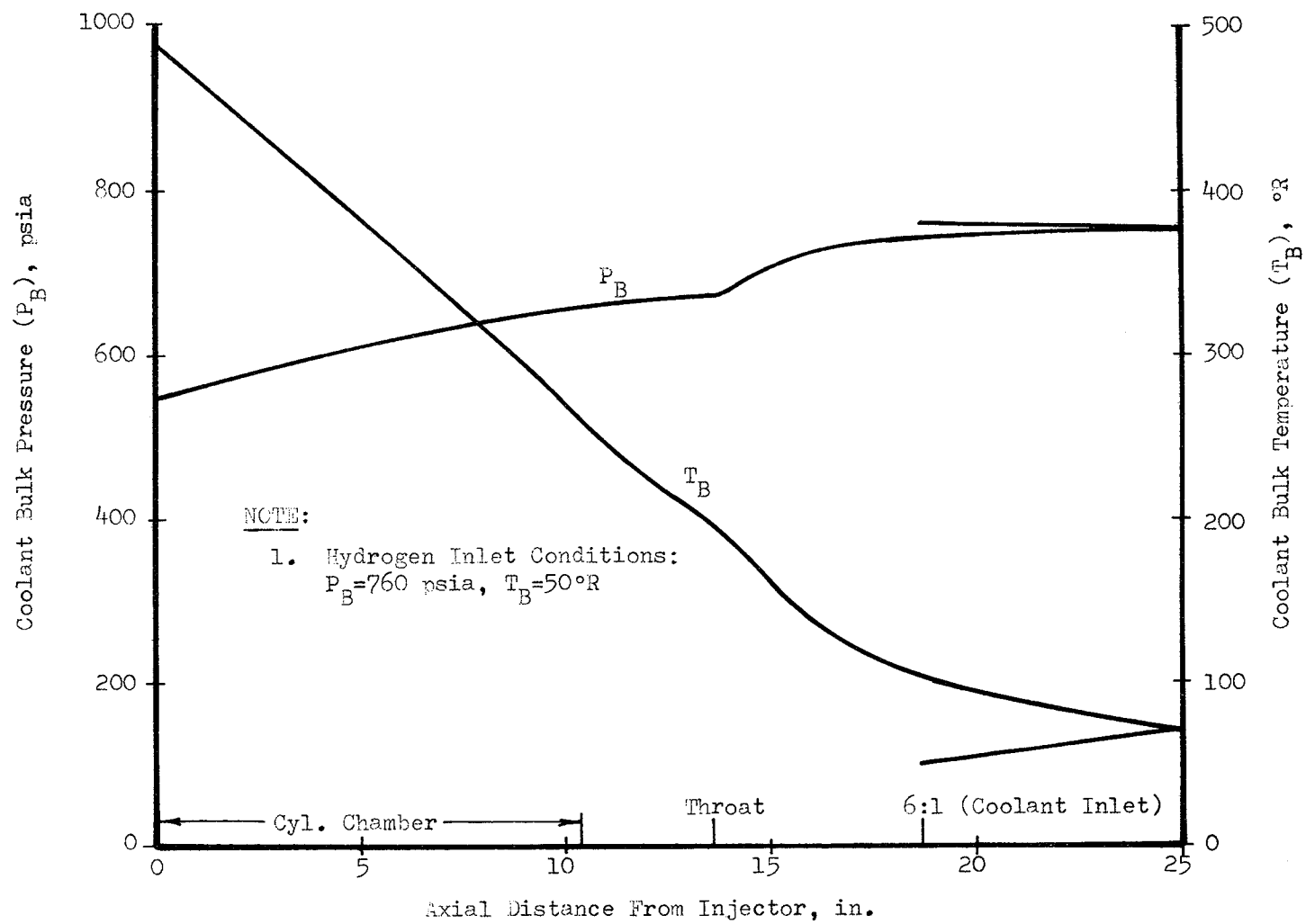
Figure 37.   Hydrogen Coolant Bulk Pressure and Temperature

TABLE XII

REGENERATIVELY COOLED CHAMBER STEADY-STATE THERMAL PARAMETERS

	Hydrogen Cooling	Water Cooling
Coolant Flow Rate, lb/sec	1.42	15.0
Heat Flux, Btu/in.^{2}-sec -Throat	8.17	8.24
-Chamber	7.42	8.10
Max Tungsten Temperature, °F		
-Throat	4249	4169
-Chamber	4456	4198
Max Nickel Wall Temperature, °F		
-Throat	776	669
-Chamber	1303	755
Max Coolant-Side Temperature, °F		
-Throat	413	302
-Chamber	1002	395
Coolant Inlet Pressure, psia	760	*
Pressure Drop, psi	213	108
Coolant Inlet Temperature, °F	-410(50°R)	70
Bulk Temperature Rise, °F	440	171
Max Coolant Velocity, ft/sec	1300	73
Max Burnout Heat Flux Ratio**	---	0.62

---

*A water supply pressure of 400 to 500 psia is recommended. The pressure drop will be independent of inlet pressure with water coolint.

**This is defined as the ratio of wall heat flux to the coolant burnout heat flux.

TABLE XIII

PREDICTED NICKEL WALL TEMPERATURE FOR
DIFFERENT COOLANT-SIDE DESIGN CORRELATIONS

Chamber Location	Thompson-Geery Regime A (1)°	Thompson-Geery Regime B (2)	Hess-Kunz (3)	McCarthy-Wolf (4)	Taylor (5)	Chamber Application
Area Ratio 16:1	173	−30	---	---	---	(1), (2)
Coolant Inlet (6:1)	238	−26	---	---	---	(1), (2)
Area Ratio 2:1	---	506	657	---	---	(2), (3)
Throat	---	---	---	962	1160	(4), (5)
Chamber Region	---	---	---	1382	1419	(4), (5)

*Type of correlation is shown in Table VIII.

III, C, Heat Transfer Analysis (cont.)

The hydrogen pressure drop, 213 psi, is calculated for a 760 psia supply pressure. This produces a 547 psia hydrogen pressure in the collection manifold, and will permit operation of the chamber and injector in series. The chamber hydrogen coolant will be supplied separately from the injector and will operate independently of the injector during the initial series of tests. However, provision for series operation of the chamber and injector has been made in the design if the initial tests are successful. The regeneratively cooled portion of the chamber was terminated at area ratio 16:1 instead of 25:1, which had been originally planned. This allows a lower pressure drop by decreasing the bulk temperature in the high velocity throat and chamber. The pressure drop for cooling to an area ratio of 25:1 is estimated to be in excess of 400 psi. Regenerative cooling to the nozzle exit, 60:1, would result in a considerably greater drop and was not considered in the design study.

The coolant pressure drop and outlet manifold pressure will vary with supply pressure, as is shown on Figure 38. It should be noted that approximately 20% of the pressure drop occurs as hydrogen velocity head loss to the outlet manifold. It is believed that 80 to 90% of this loss can be recovered by employing a diffuser section between the end of the coolant channel and the manifold. Although space limitations with the present injector-chamber configuration did not allow incorporating a high efficiency diffuser in the design, the diffuser could be included in a flight-weight version. This potential recovery of velocity head is included in the dashed curve ($\Delta P'$) on Figure 38.

b.   Two-Dimensional and Transient Heating Effects

The two-dimensional heat transfer effects were evaluated to facilitate a comprehensive stress analysis of the coating-nickel channel composite structure, and to determine the effects on chamber wall temperature.
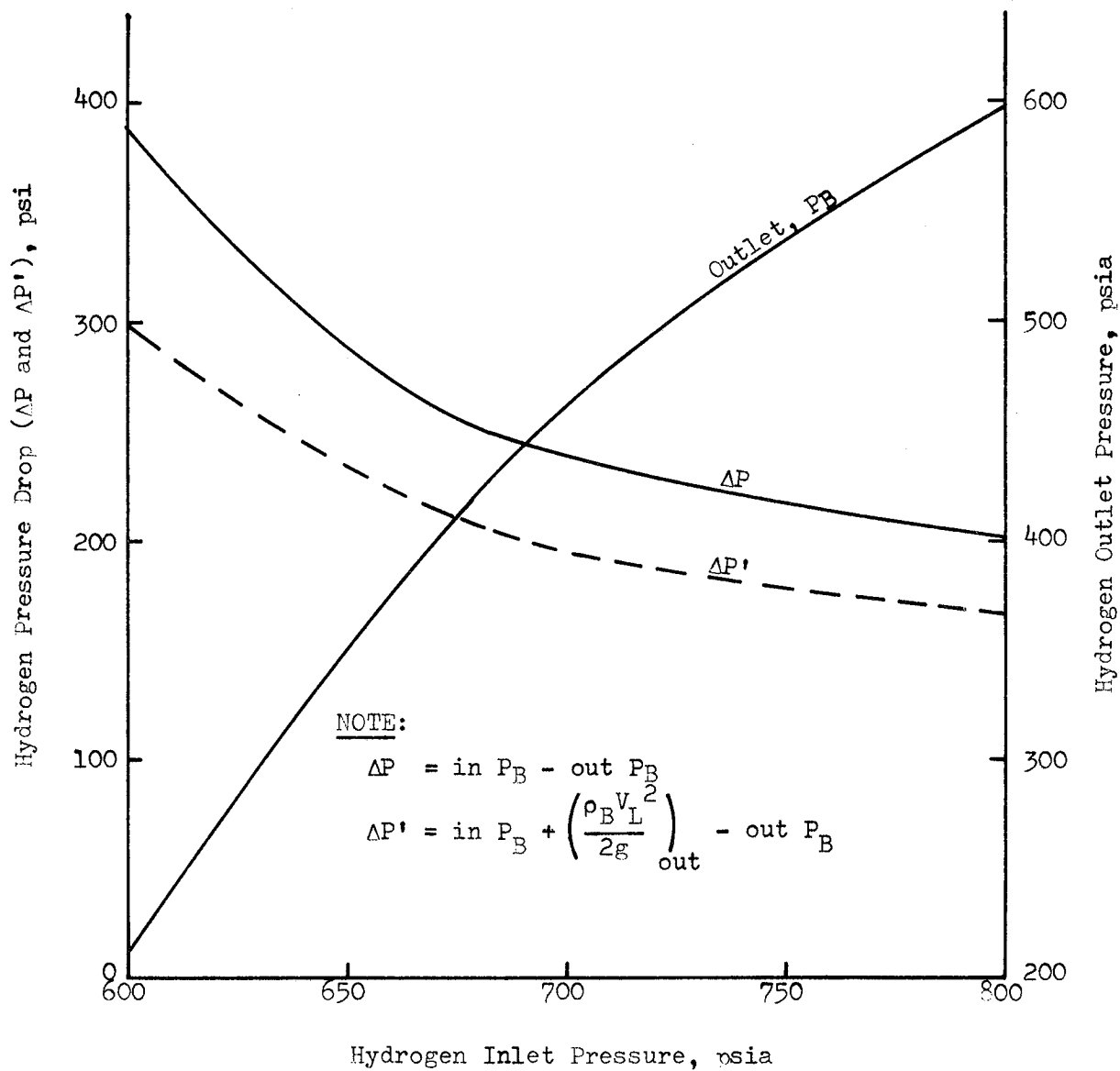
Figure 38. Hydrogen Pressure Drop and Outlet Pressure

III, C, Heat Transfer Analysis (cont.)

The two-dimensional temperature network for the channel cross-section and coolant conditions at the throat is given on Figure 39. The lower nickel temperatures which occur at the nickel-coating interface near the land center line are attributed to the "fin" effect of the land and the outer nickel shell, which is further enhanced by the high nickel conductivity at low temperatures (see Figure 33).

The throat startup temperature transients for several radial locations at the channel center line are shown on Figure 40. The highest temperature gradients during startup will occur in the tungsten-zirconia portion of the coating.

The heat stored in the coating will redistribute itself and will increase the channel temperature, unless the coolant flow is continued after shutdown. Shutdown transients were not considered in this investigation, but will be considered when the injector purge flow has been established. Post-shutdown coolant flow may be required to minimize thermal shock of the coating.

c. Ablative Skirt

The ablative skirt liner materials and thicknesses were selected to permit a 180 sec continuous firing duration. The skirt will consist of a tapered carbon-reinforced phenolic inner flame liner and a silica-reinforced phenolic overwrap. The surface, interface and outside temperature transients of the skirt at the attachment point and the nozzle exit are shown on Figure 41.

Figure 39. Two-Dimensional Chamber Wall Temperature at Throat
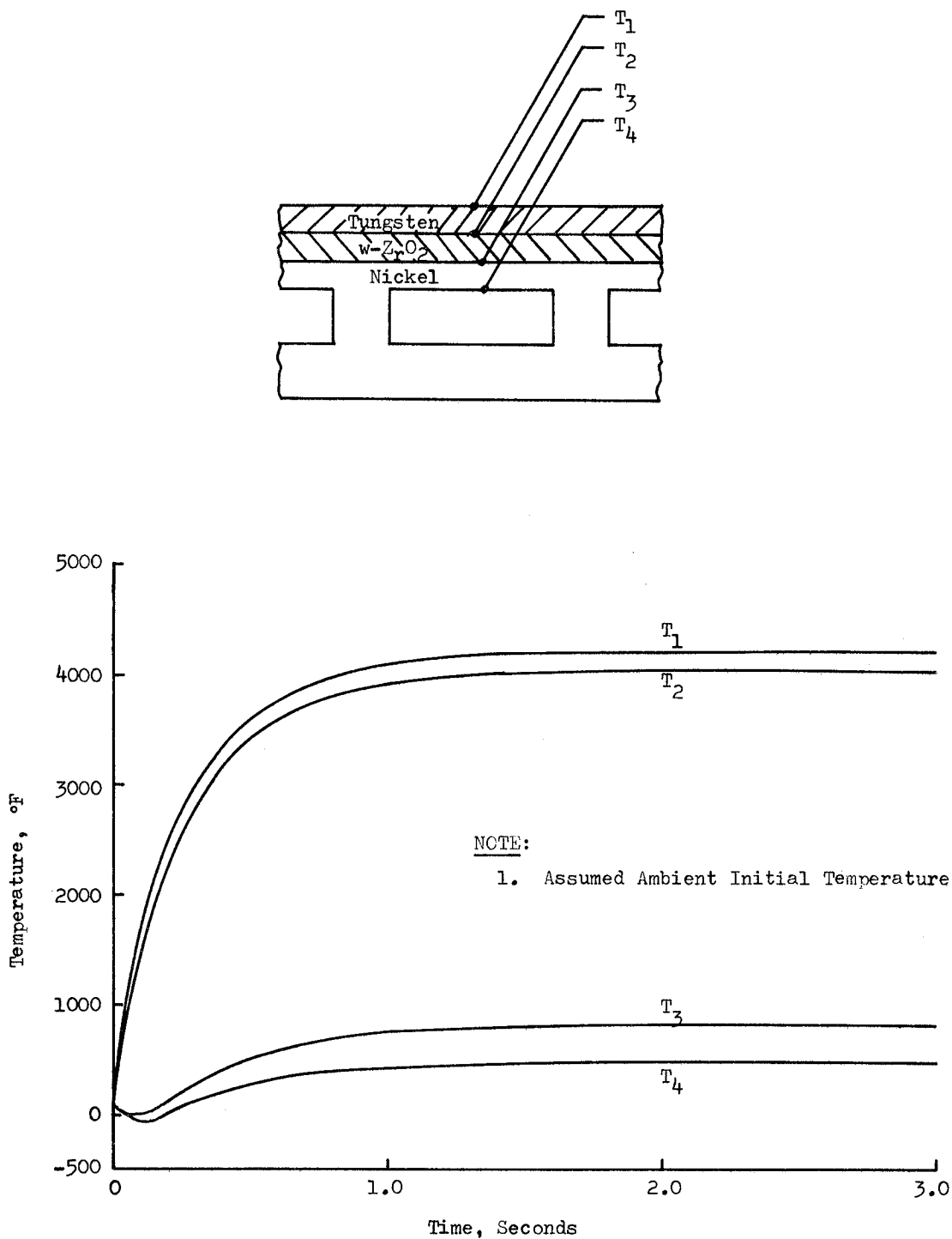
Figure 40. Chamber Wall Startup Temperature Transients at Throat
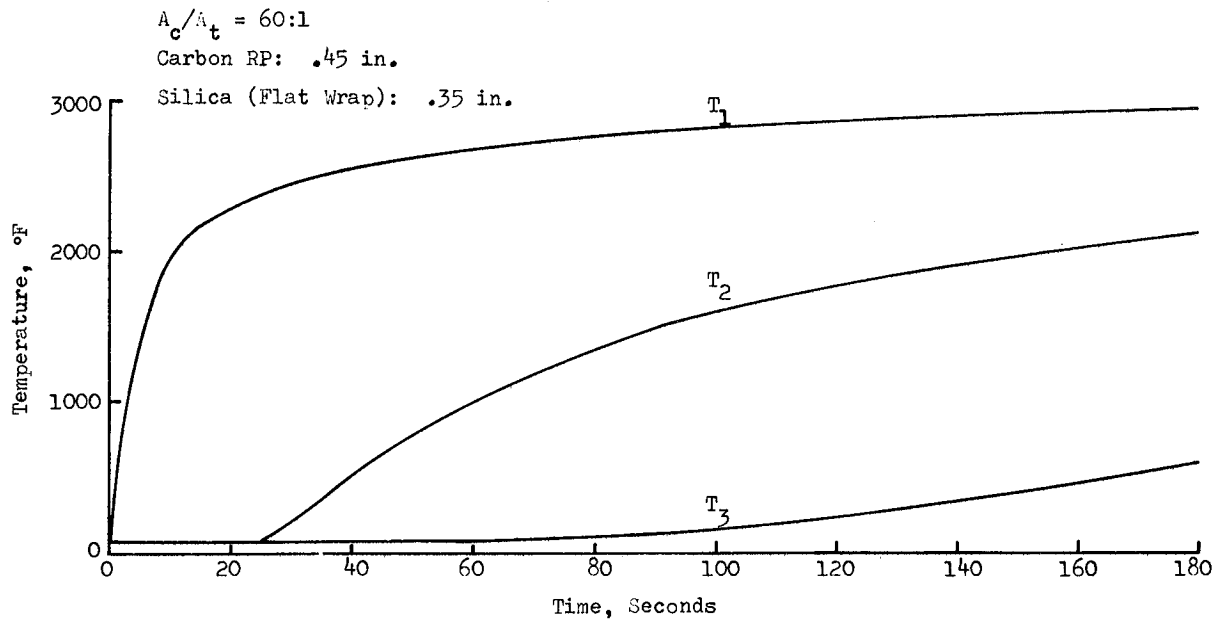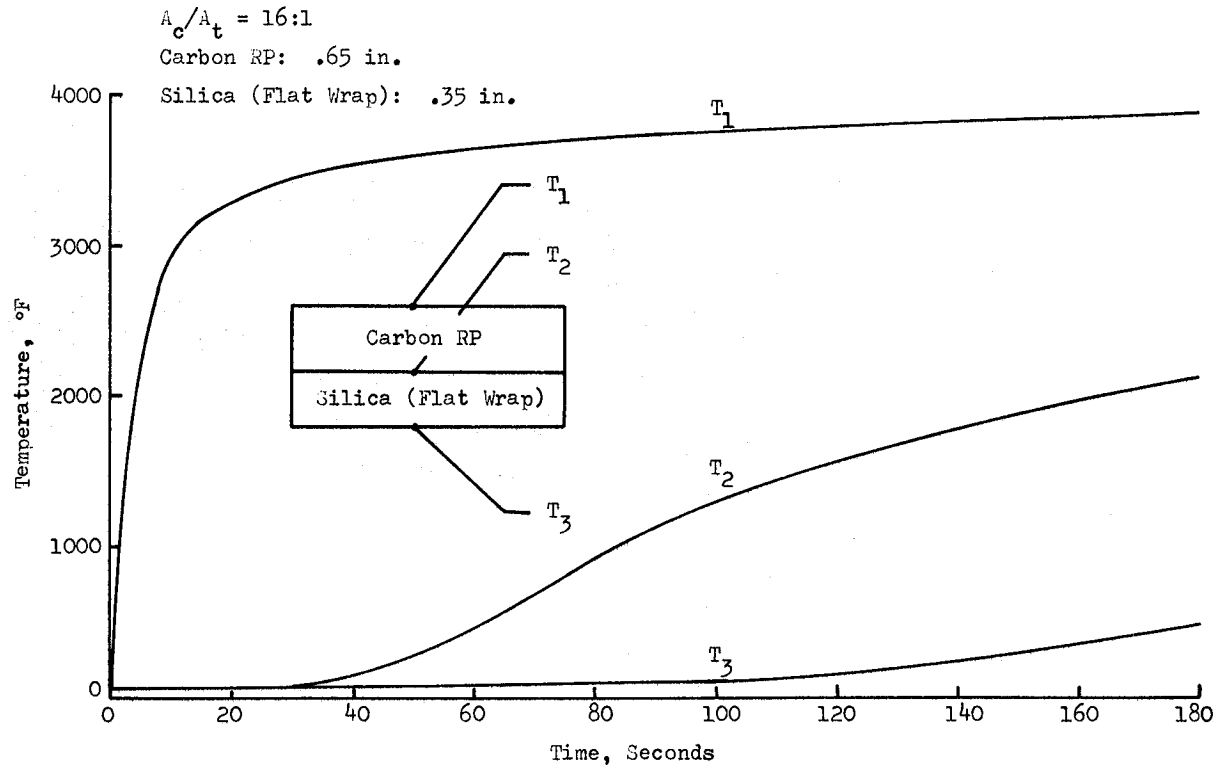
Figure 41. Ablative Skirt Temperature Transients

III, C, Heat Transfer Analysis (cont.)

d. Wall Temperature Instrumentation

In addition to hydrogen bulk pressure and temperature instrumentation, thermocouples are planned for measuring the channel wall temperatures. Thirty locations at ten axial locations and in three planes will be adequate to obtain the channel wall temperature profiles. The planned thermocouple location schedule is given in Table XIV.

TABLE XIV

THERMOCOUPLE LOCATION SCHEDULE

Group	No. Tc's	Approximate Axial Location	Angular Location	Type
1	3	1 in. Downstream of Injector Face*	0°, 120°, 240°	CA
2	3	4 in. Downstream of Injector Face	0°, 120°, 240°	CA
3	3	7 in. Downstream of Injector Face	0°, 120°, 240°	CA
4	3	End Cylindrical Chamber	0°, 120°, 240°	CA
5	3	3/4 in. Upstream Throat	0°, 120°, 240°	CA
6	3	Throat	0°, 120°, 240°	CA
7	3	3/4 in. Downstream Throat	0°, 120°, 240°	CA
8	3	A/A_t = 2:1	0°, 120°, 240°	CA
9	3	A/A_t = 8:1	0°, 120°, 240°	CC
10	3	A/A_t = 12:1	0°, 120°, 240°	CC

*Reference NASA/Lewis Drawing CD 620831 (Injector Assembly)

These locations will provide temperature data to define axial and circumferential variations both directly under and between the coaxial elements of the injector which will be used for testing. Nominal 0.020 in. OD sheathed thermocouples, which can be threaded into the nickel land, will be employed. These will provide good transient response characteristics and will minimize the thermal perturbation introduced by the thermocouples. The thermocouples will

III, C, Heat Transfer Analysis (cont.)

be located in the nickel land, adjacent to the coolant-side of the inner nickel shell. This is desirable from a fabrication standpoint and is thermally acceptable because of the flat, two-dimensional temperature profiles that occur in this region (see Figure 39). A typical thermocouple installation is shown in Figure 25.

III, Task I--Design and Analysis (cont.)

D. STRESS ANALYSIS

1. Introduction

The purpose of this analysis is to define the structural integrity of the proposed design. The conditions chosen for this analysis were the maximum engine operating pressure and steady-state temperature acting simultaneously.

The entire study was accomplished using the latest analytical methods which consist in most cases of constructing finite element computer models of the chamber and applying the design loads to these models. A brief summary of the structural investigation appears below:

2. Summary

The evaluation was performed and the ultimate margin of safety for a maximum design load condition was determined. Local yielding was indicated in the chamber structure on the hot side. This condition is typical for all cooled chambers and has been proven by actual tests to be acceptable when high ductility materials were used.

The maximum compression strain imposed upon the tungsten is approximately 1.6%. At the high temperature, the elongation is approximately 20% and, therefore, is adequate. However, it is subject to low cycle fatigue for which there is no available data on tungsten.

At the initiation of a firing, the tungsten and its composites are subject to thermal shock. The inner layer of pure tungsten being of high conductivity, assumes the high temperature almost instantaneously with little

III, D, Stress Analysis (cont.)

gradient and will, therefore, not be subjected to tension shock; however, the next layers being of low conductivity, will develop high thermal gradients during the transient and may be susceptible to tension cracks.

In the stress analysis performed, only the steady-state thermal conditions were used; therefore, the stress values and their locations correspond to those conditions only. Both manifolds were analyzed by the 1040 Computer Program.

High stress values were found in the inlet manifold at the joint. This high stress is developed due to restraint imposed by the chamber ring and is of local character only. Following are the margins of safety for the critical areas:

TABLE XV

Location	Margin of Safety
Inlet Manifold	+ 0.65 (Ultimate)
Chamber Throat	1.2% Strain (Plastic)
Chamber, Upper Section	1.16% Strain (Plastic)
Flange	0.25 Yield
Outlet Manifold	Excessive (Yield)

3. Analysis

a. Description of the Thrust Chamber

The combustion chamber is constructed of 96 electroformed nickel channels with 0.030 in. inner and 0.060 in. outer wall in the chamber section. Channels are of rectangular shape, 0.080-in. in height and 0.096-in.-width, average separated by 0.090 in. ribs.

III, D, Stress Analysis (cont.)

The internal surface of the chamber is made from tungsten and tungsten-zirconia composition formed in concentric layers by: (1) 0.030-in.-thick inner vapor deposited W; (2) 0.016-in.-thick plasma-arc sprayed 88% W and 12% ZrO_2; (3) 0.009 in. of 75% W - 25% ZrO_2 sprayed; (4) 0.012 in. of 50% W - 50% ZrO_2 sprayed.

The upper part of the chamber is welded to the T304L Stainless Steel flange machined to form the inner manifold and with drilled passages leading to the toroidal outlet welded on manifold.

b.   Structural Design Criteria

The conditions selected for this analysis were based on the availability of thermal data and represents the steady-state thermal, combined with operating pressures. The design safety factor considered is 1.5 for the mechanical stress, based on the ultimate, and 1.0 safety factor for thermal stress. Yielding conditions, whenever not too excessive, will be considered permissible. Local yielding is very frequently experienced in cooled chambers, and it is not practically feasible to design to preclude it wherever thermal stresses are prevailing.

Design Loads:

T 8000-lb Thrust

T_c 400-psi Chamber Pressure

P_{in} 800-psi Manifold Inlet Pressure

P_t 730-psi Channel Throat Pressure

P_o 605-psi Manifold Outlet Pressure

MR 12:1 Mixture Ratio

T_1 4455°F Chamber Inner Wall Temperature

III, D, Stress Analysis (cont.)

T_2 4215°F Throat Inner Wall Temperature

T_3 1809°F Inner Wall Temperature (at A/A_t = 6:1)

T_c -410°F Coolant Inlet Temperature

T   -30°F Coolant Outlet Temperature

c.   Method of Analysis

The analysis was conducted using two computer programs:
(1) Linear Shell Program 1040 for both inlet and outlet manifolds; and (2)
A Digital Computer Program E11401 (Ref 39) for the finite element analysis of
solids was used for the composite structure of flange and upper chamber, and
for the calculation of plain stress at two sections of chamber (a) under
flange and (b) at throat.

(1)   1040 Program

This program is a numerical analysis for the
solution of the general equations of thin shells of revolution subjected to
axisymmetrical pressure and temperature distribution.

The basic differential equations are in a very
general form which permits the geometry to be specified by discrete points.
The analysis determines elastic stresses, strains, and displacements for
multi-layer, multi-sectional shells of revolution. Surface loads, temperature,
thicknesses and material properties may vary arbitrarily in the meridional
direction.

(2)   Finite Element Program E11401

The finite element method is applied to the
determination of displacements and stresses within plane or axisymmetric solids

III, D, Stress Analysis (cont.)

with linear or non-linear material properties. The continuous body is
replaced by a system of elements with triangular or quadrilateral cross
section. Since the elements are of arbitrary shapes and material properties,
the procedure may be applied to structures composed of many different materials
of practically any symmetrical geometry.

In the finite element approximation of solids, the
continuous structure is replaced by a system of elements which are inter-
connected at joints or nodal points. Equilibrium equations, in terms of unknown
nodal point displacements, are developed at each nodal point. A solution of
this set of equations constitutes a solution to the system.

The advantages of the finite element method, as
compared to other numerical approaches, are numerous. The method is completely
general with respect to geometry and material properties. Complex bodies
composed of many different materials are easily represented. Since anisotropic
materials are automatically included in the formulation, filament structures
are readily handled.

Figures 42 through 54 show the pressure and thermal
conditions, Figures 55 and 56, physical properties of materials, and Figures 57
through 63 illustrate the stress in the sections.

(3) Outlet Manifold

The outlet manifold is shown in Figure 57. The
torus stresses were calculated by the 1040 computer program with a pressure
of 650 psia and utilized fixed end boundary conditions. This results in the
conservative values in the discontinuity region of the fixed ends.
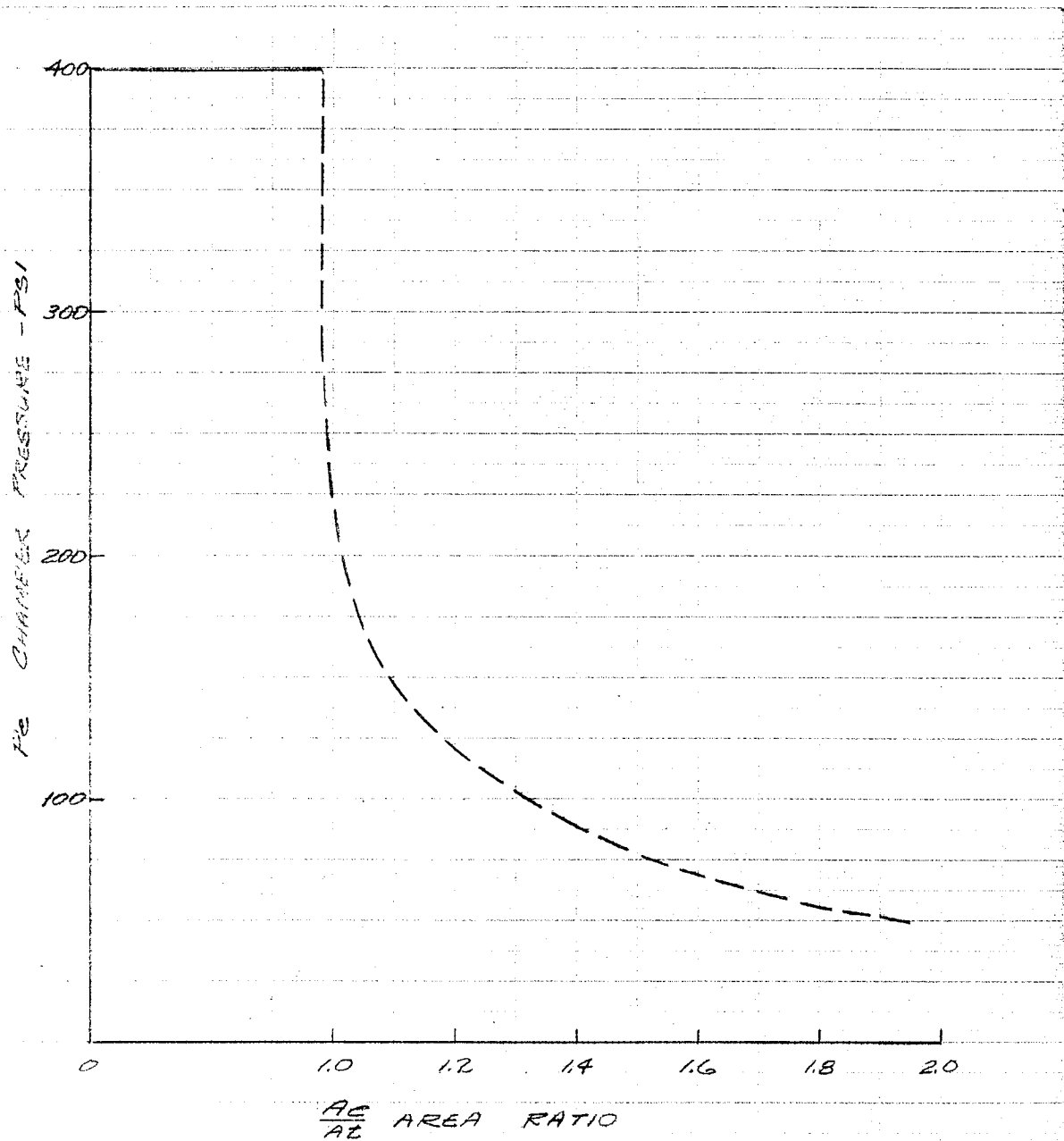
Figure 42.   Chamber Pressure vs Area Ratio 1:1 - 2:1
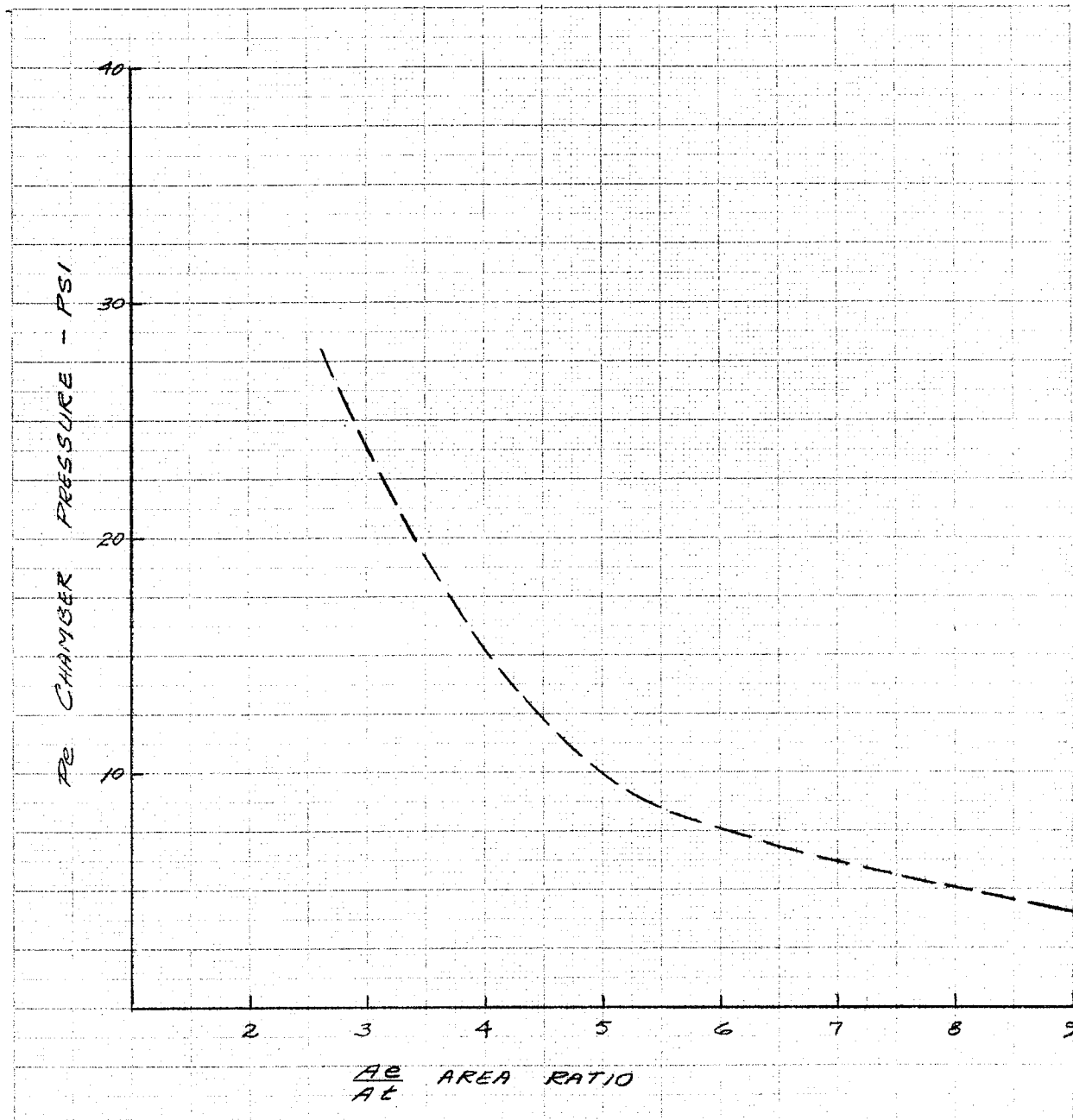
Figure 43.   Chamber Pressure vs Area Ratio 2:1 - 10:1
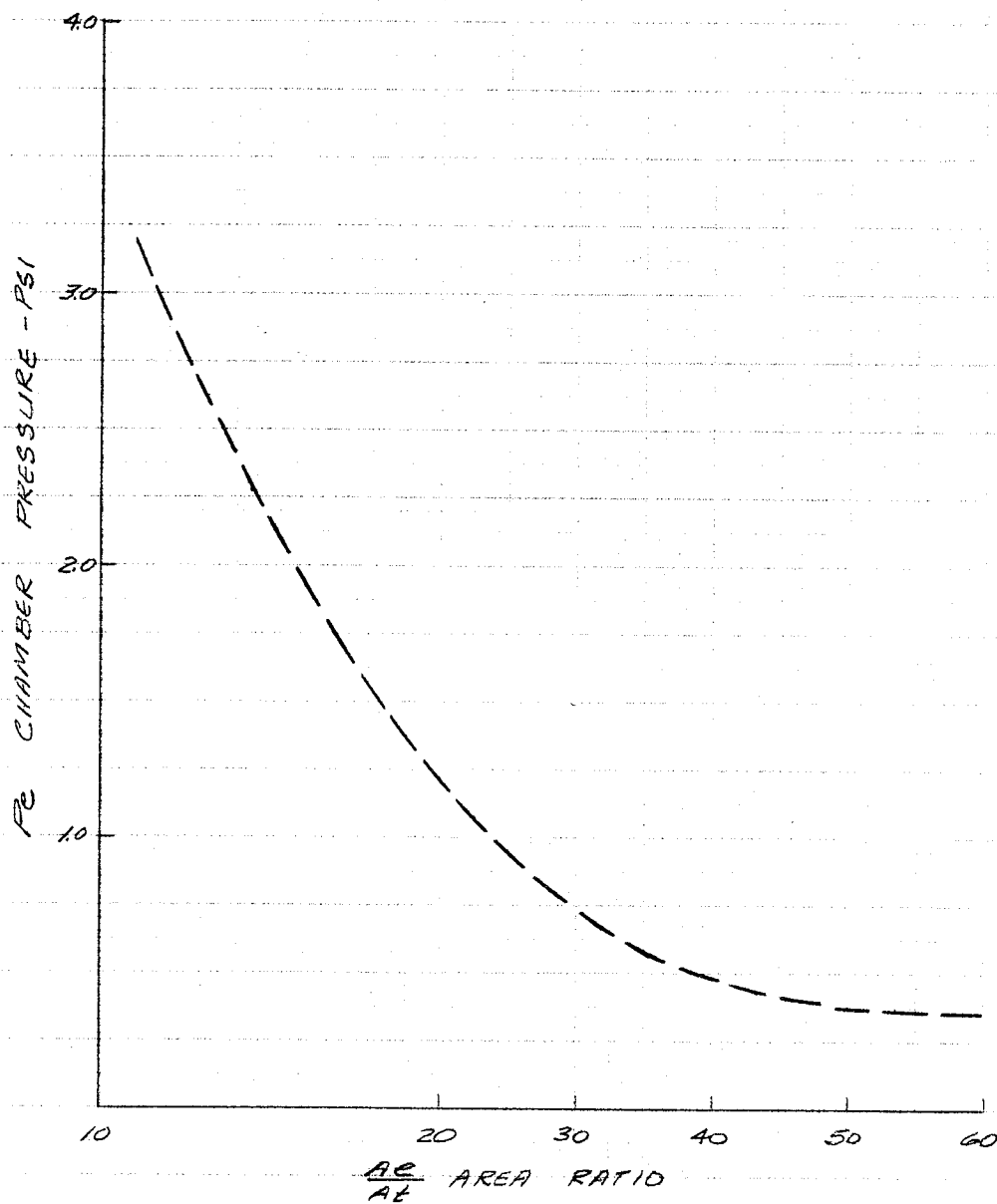
Figure 44. Chamber Pressure vs Area Ratio 10:1 - 60:1
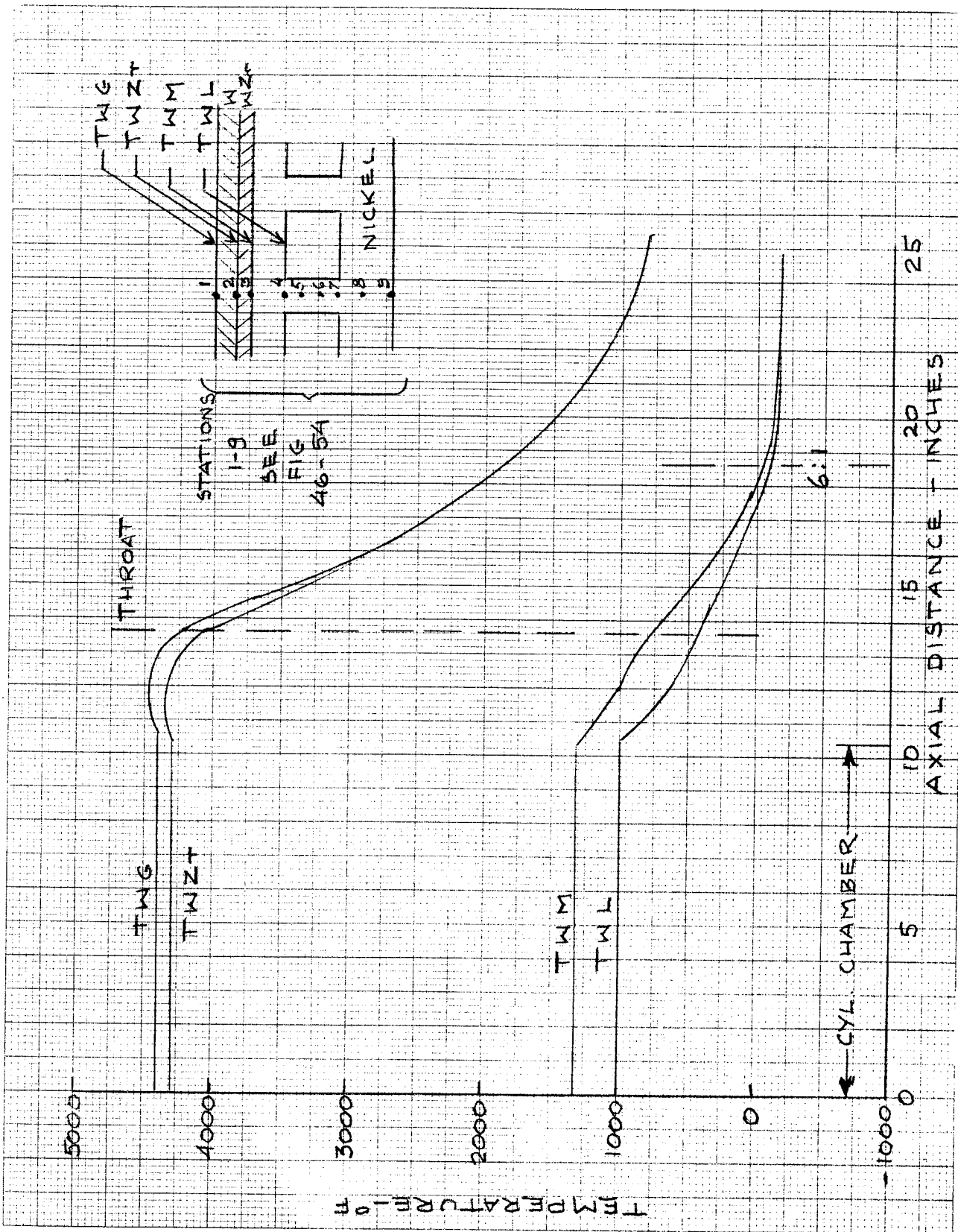
Figure 45. Chamber Wall Temperature
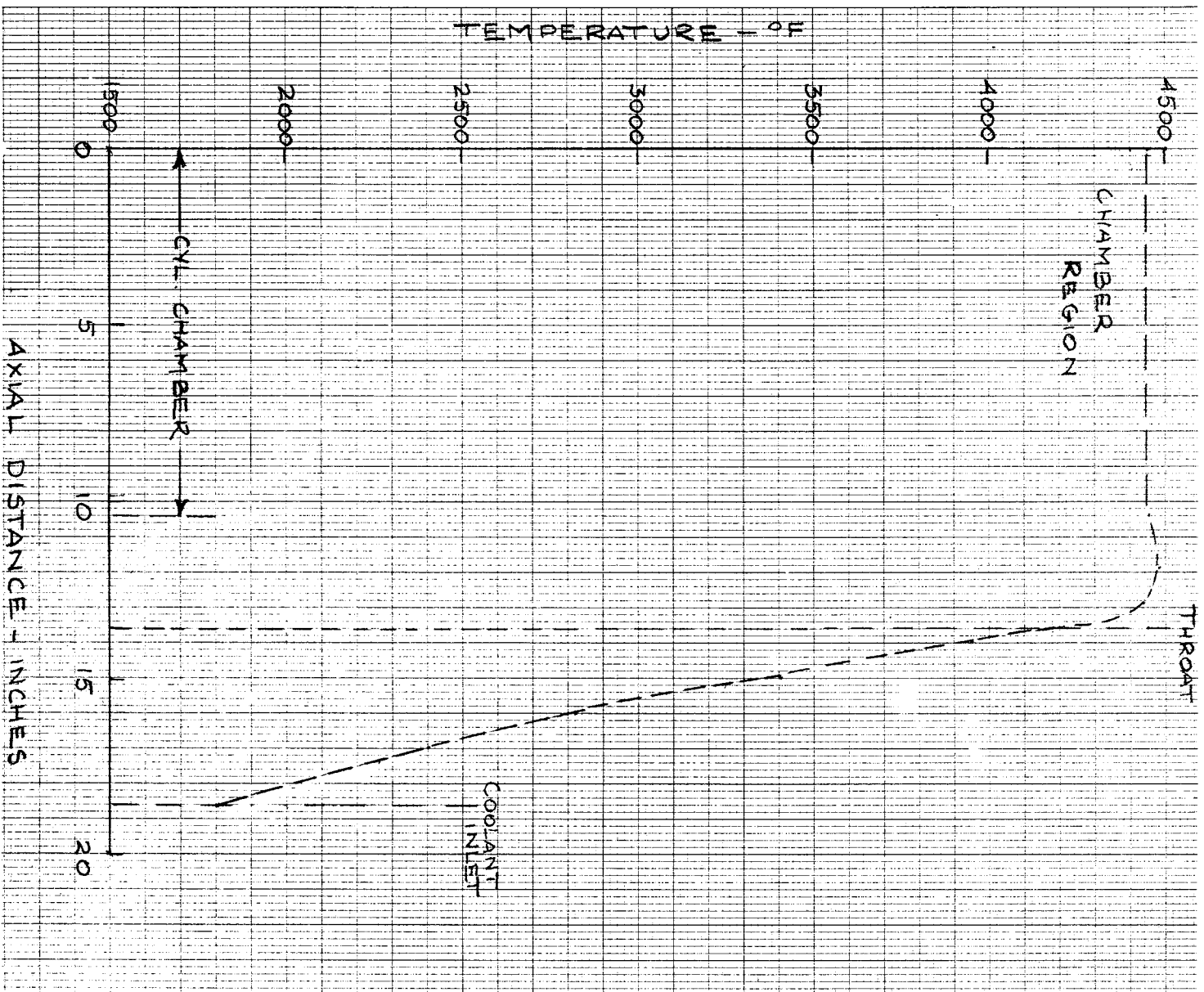
Figure 46. Chamber Wall Temperature Station 1
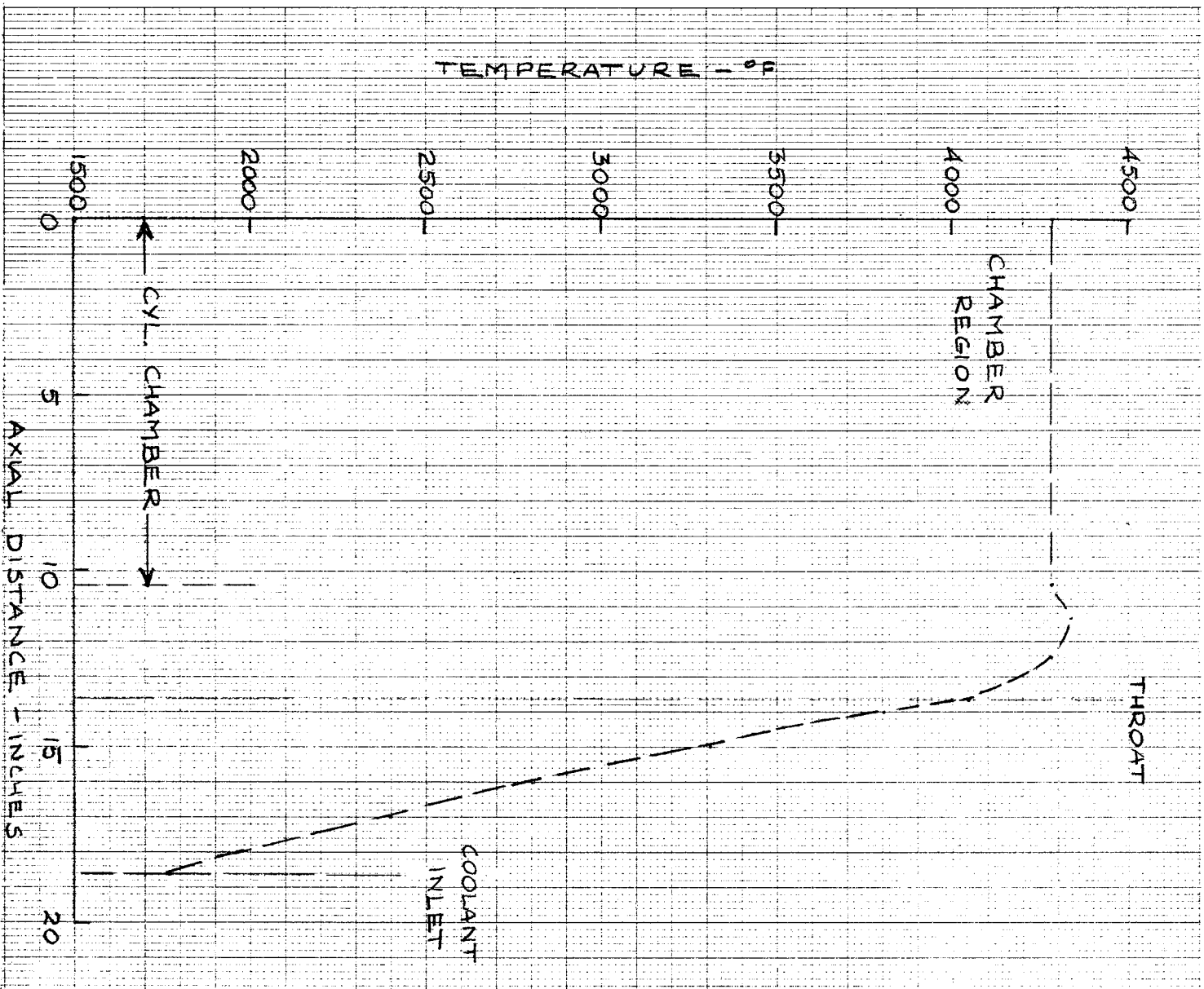
Figure 47. Chamber Wall Temperature Station 2
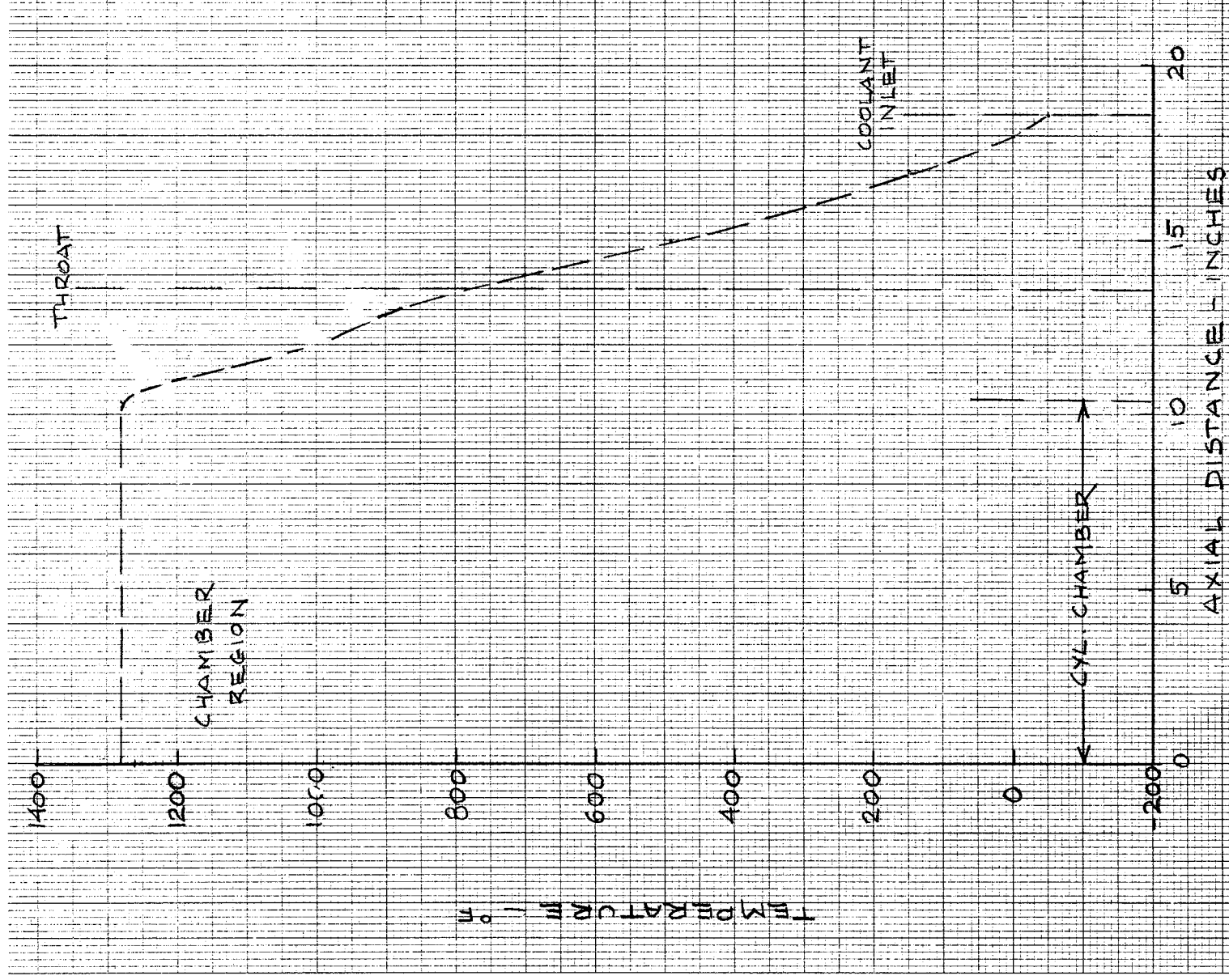
Figure 48. Chamber Wall Temperature Station 3
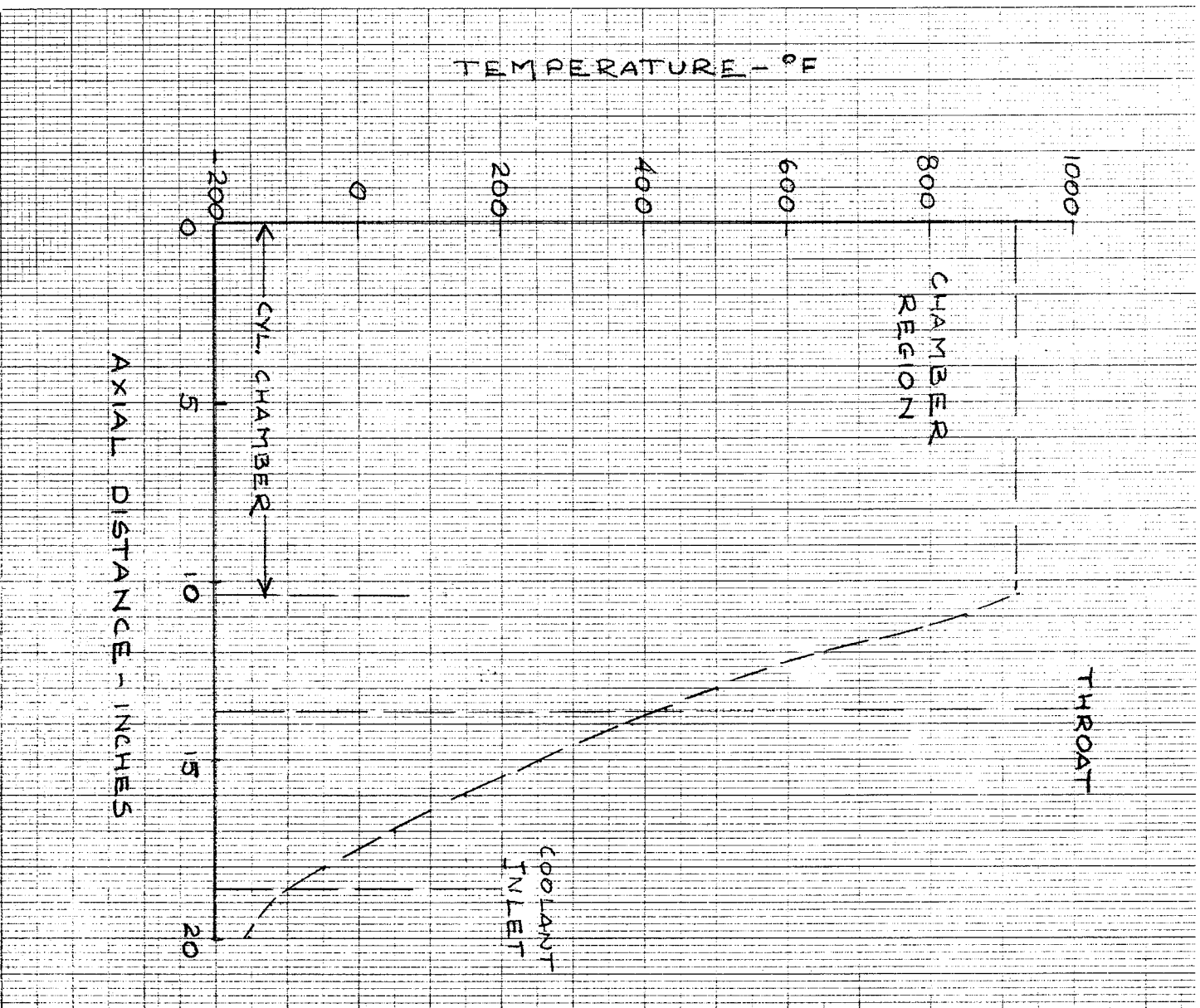
Figure 49. Chamber Wall Temperature Station 4
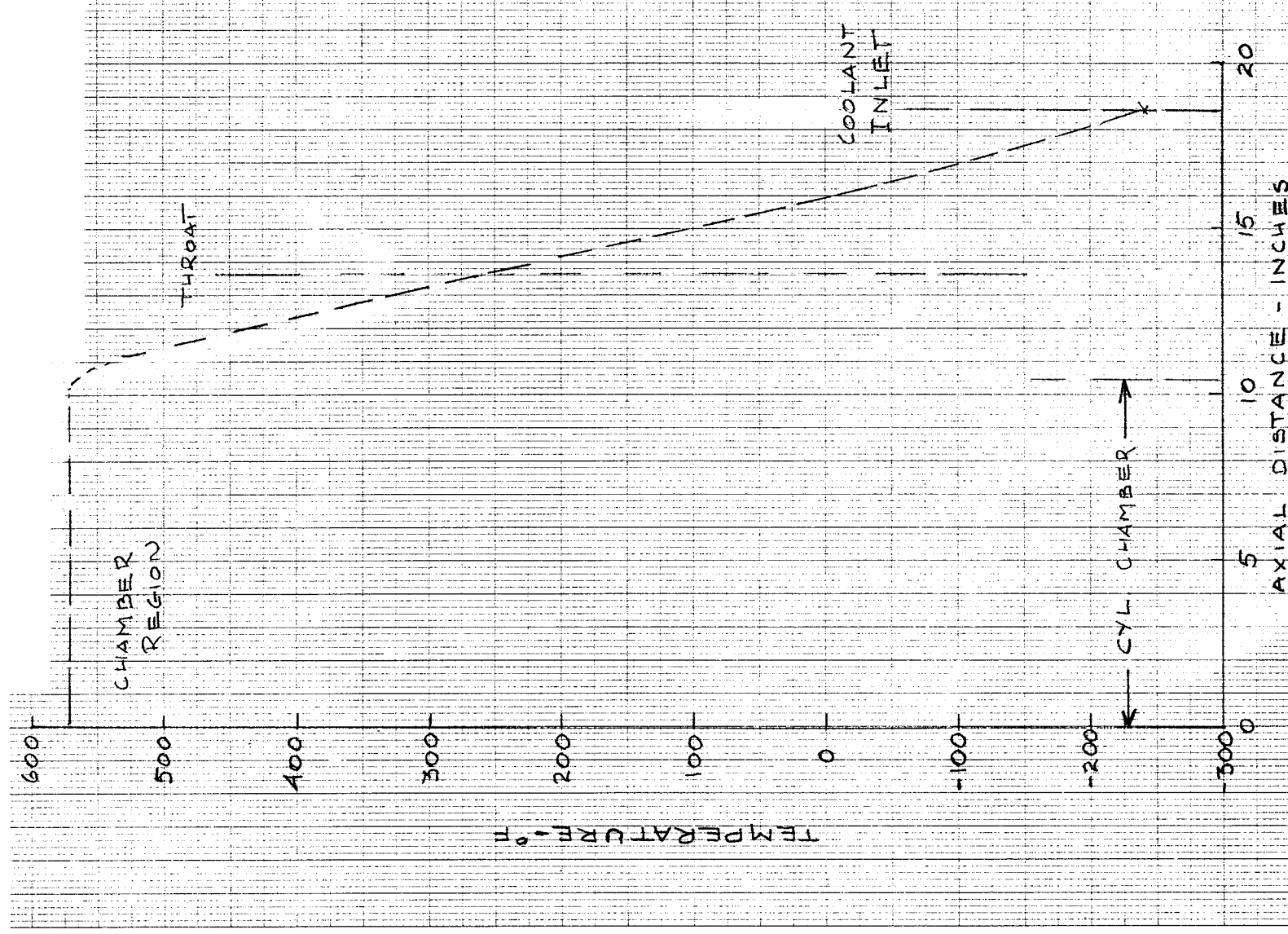
Figure 50.   Chamber Wall Temperature Station 5
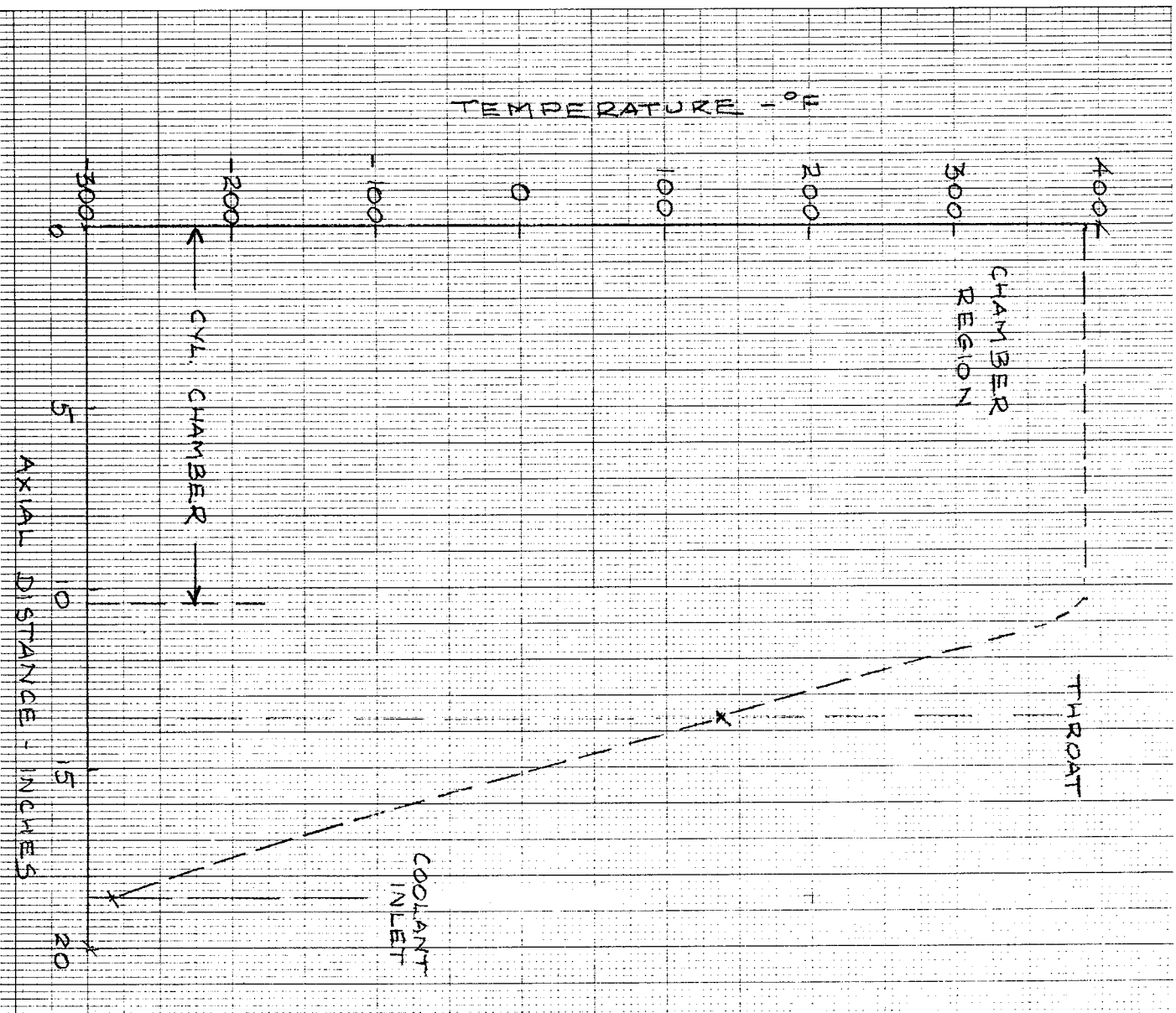
Figure 51. Chamber Wall Temperature Station 6
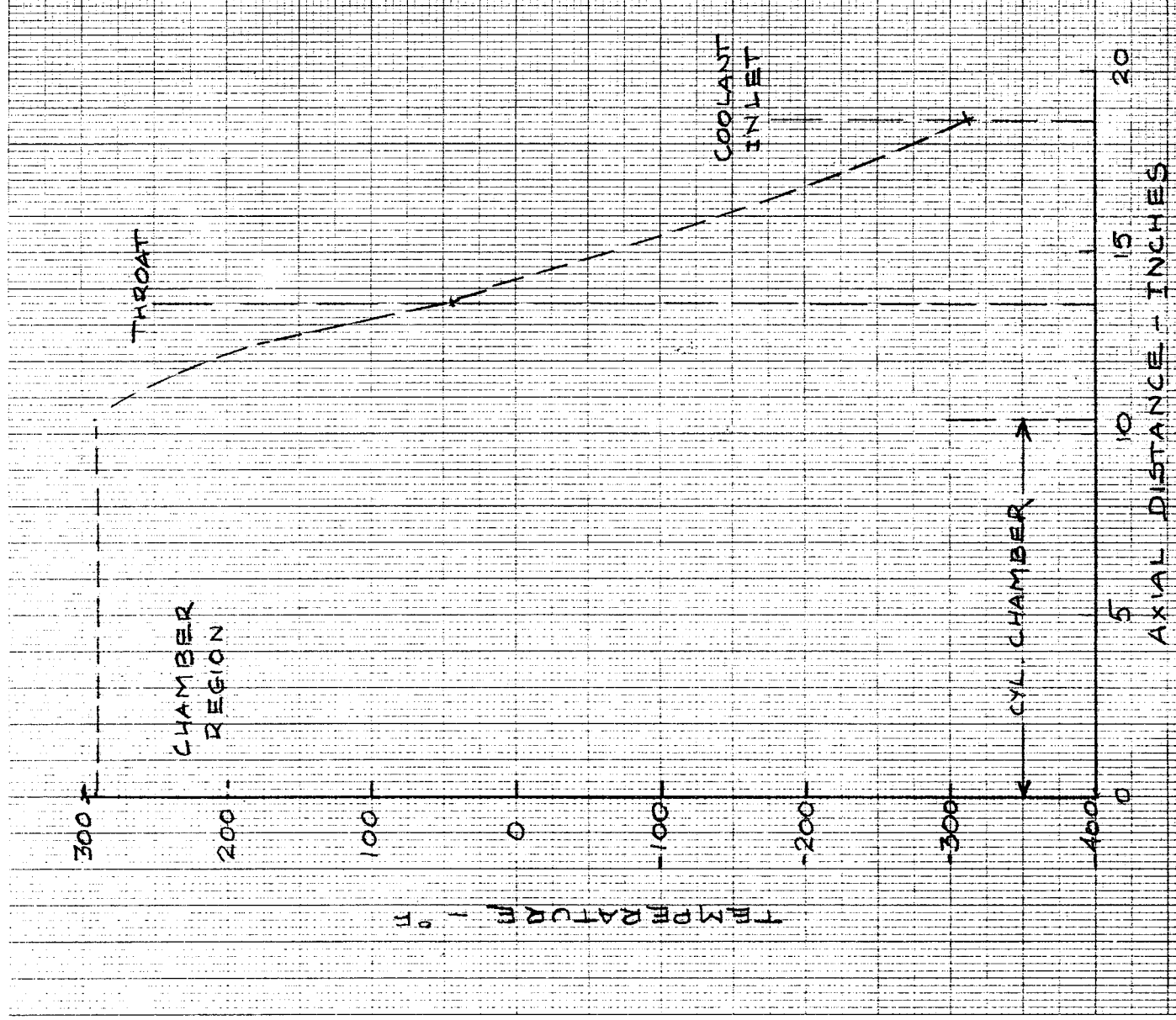
Figure 52. Chamber Wall Temperature Station 7
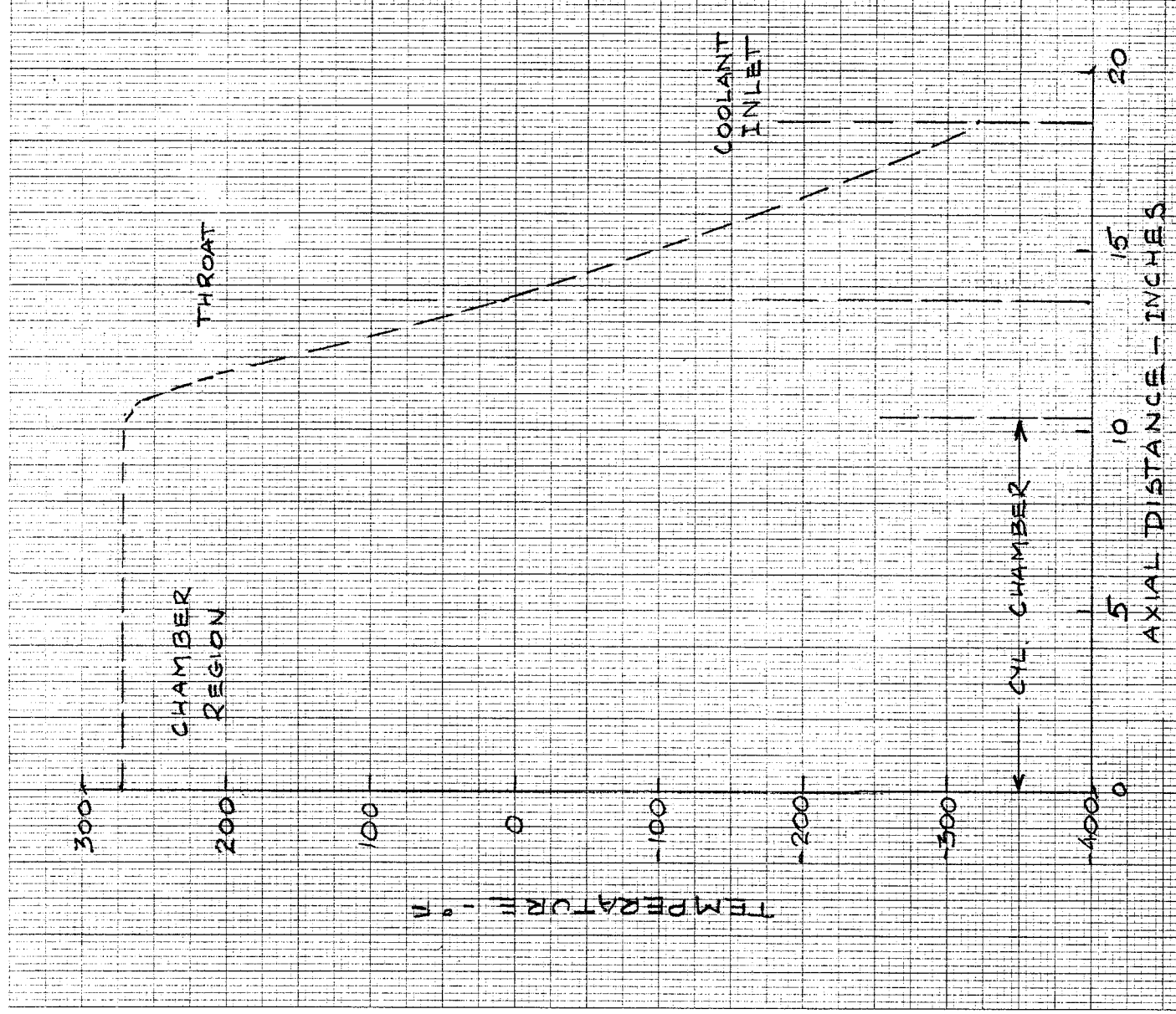
Figure 53.   Chamber Wall Temperature Station 8
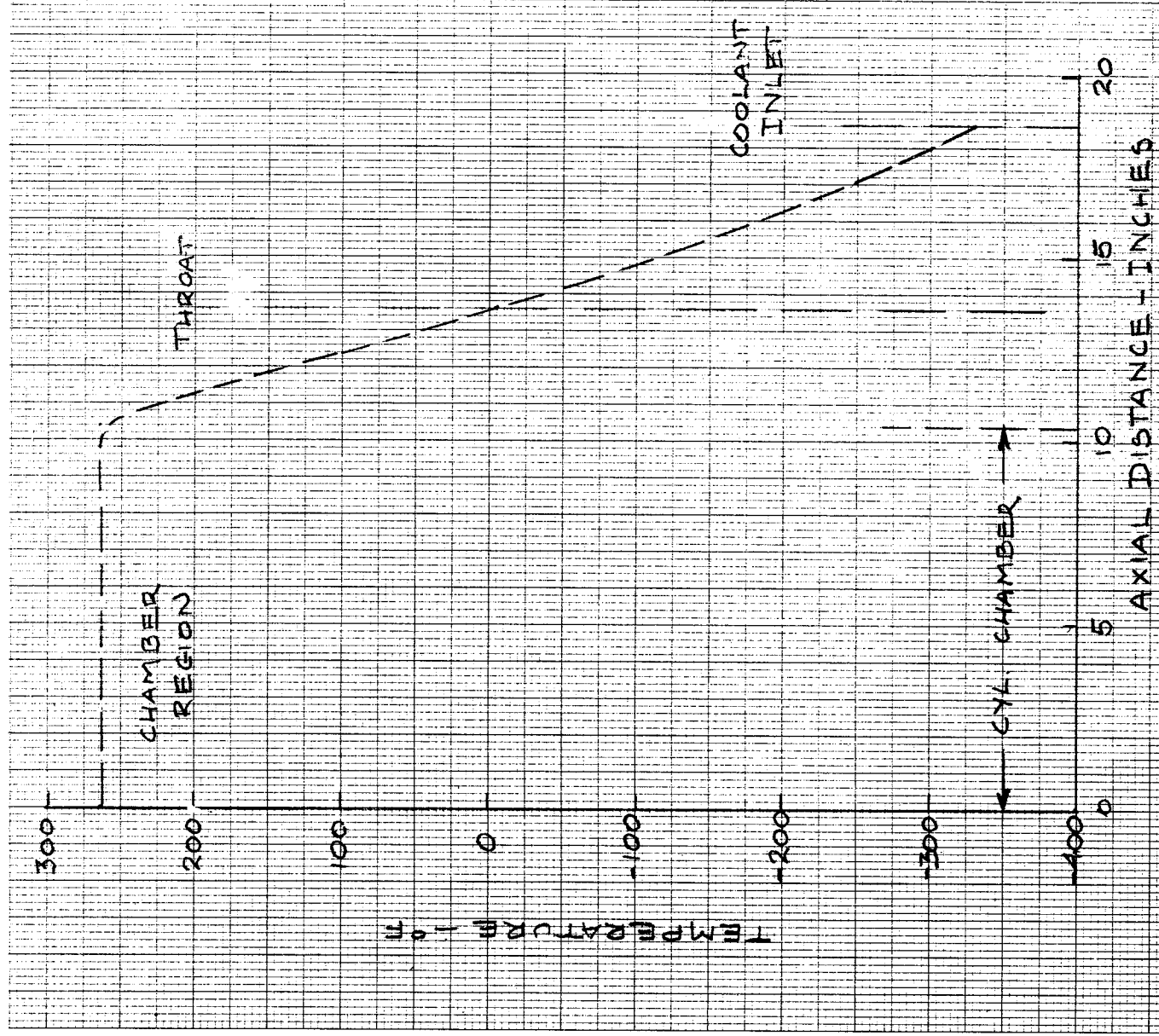
Figure 54. Chamber Wall Temperature Station 9
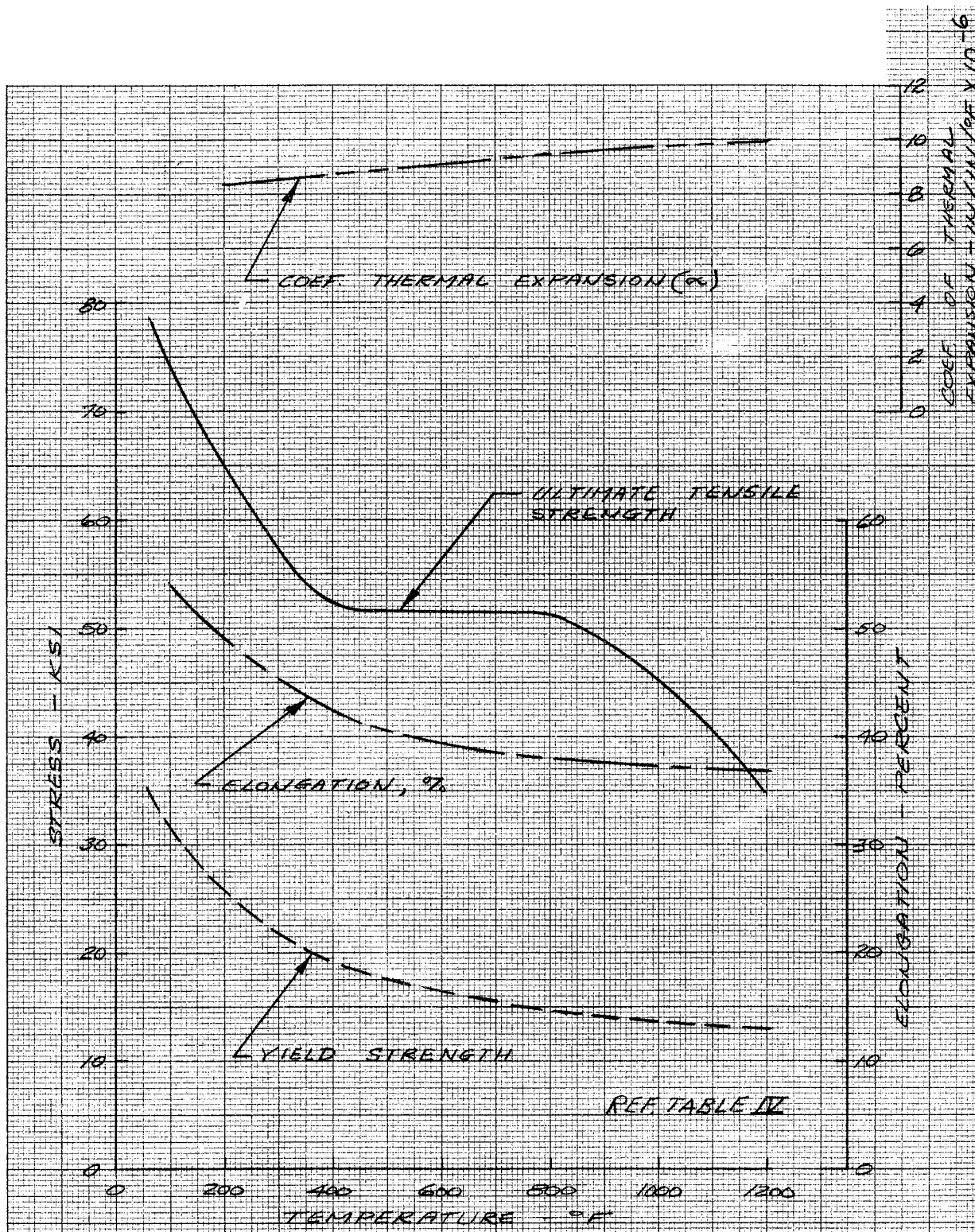
Figure 55. Mechanical Properties of SS 304
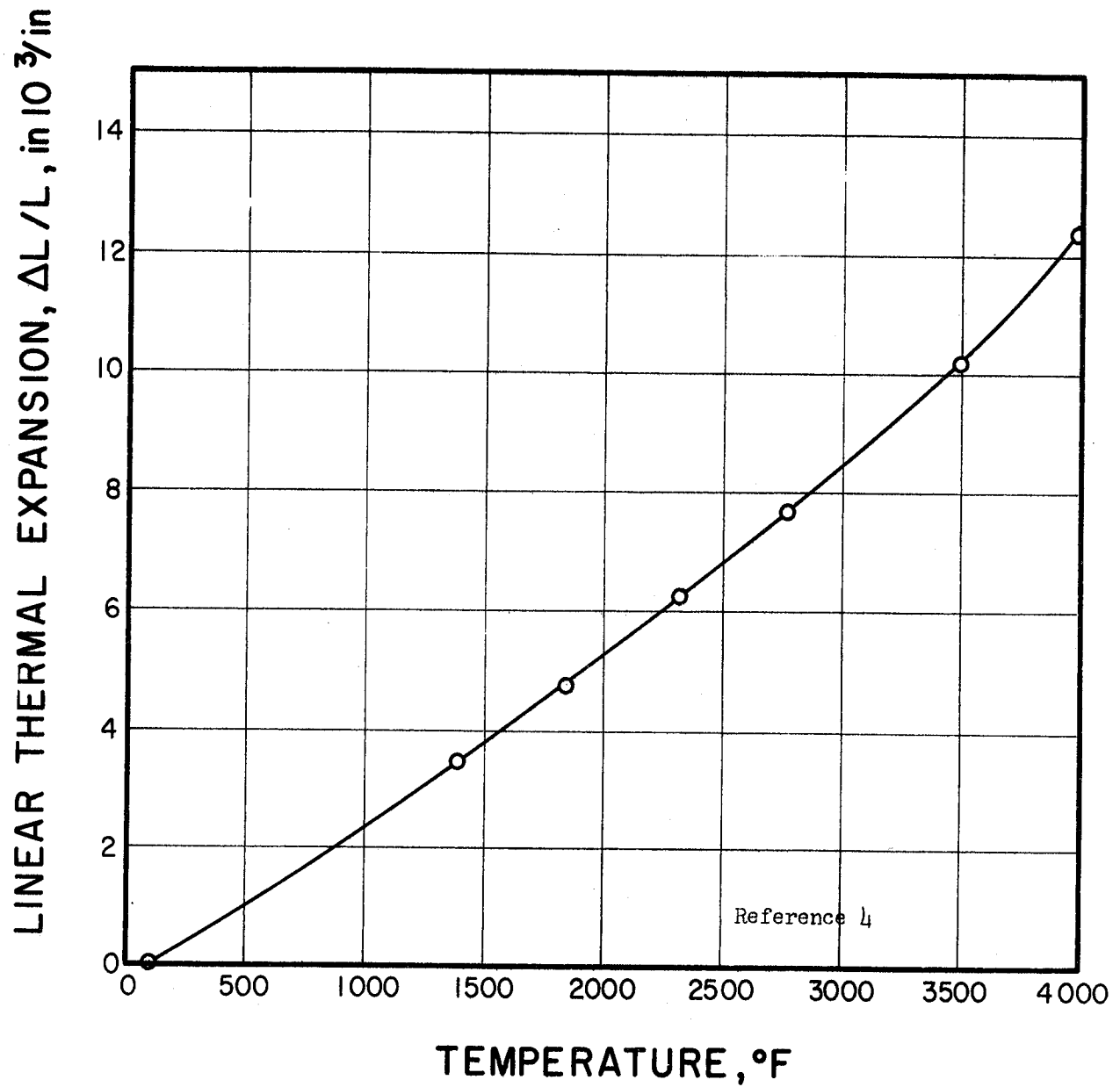
Figure 56. Thermal Expansion of Annealed
Polycrystaline Tungsten
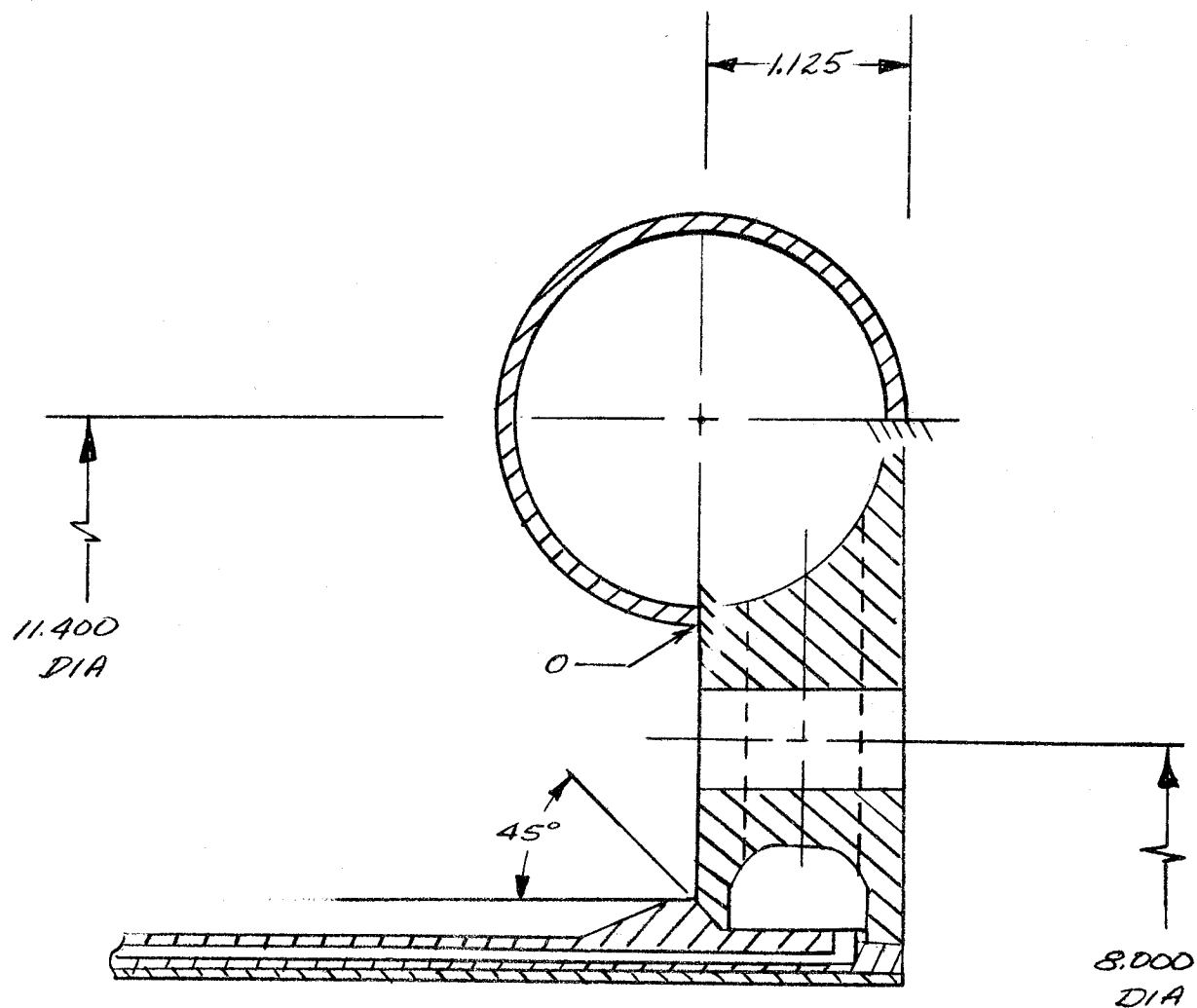
Figure 57. Outlet Manifold
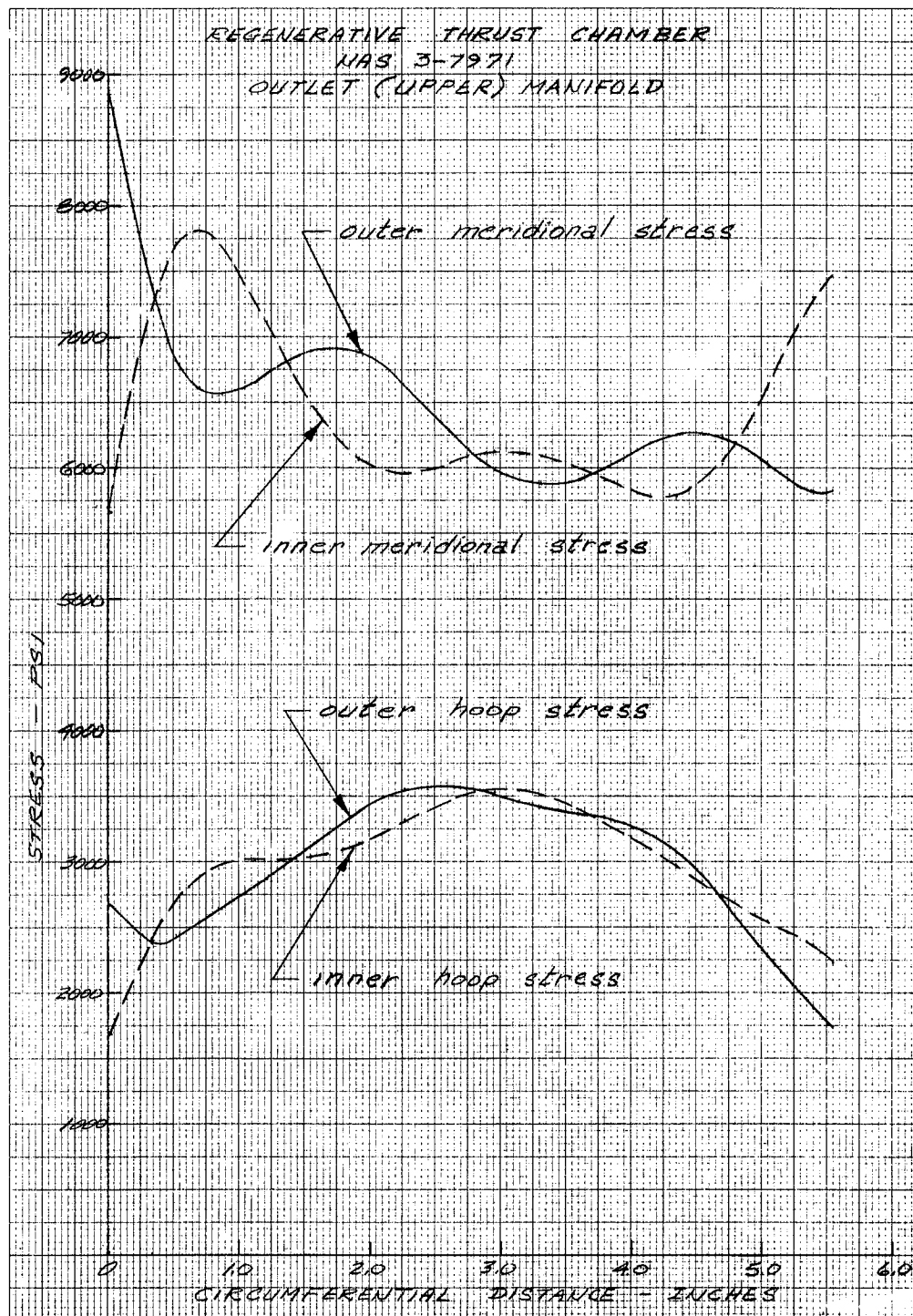
Figure 58. Stresses in the Outlet Manifold

SST TUBING
2.250 O.D × .109 WALL

5.013 TO ℄ THROAT

O

11.580
DIA

95°

11.400
DIA

9.640
DIA
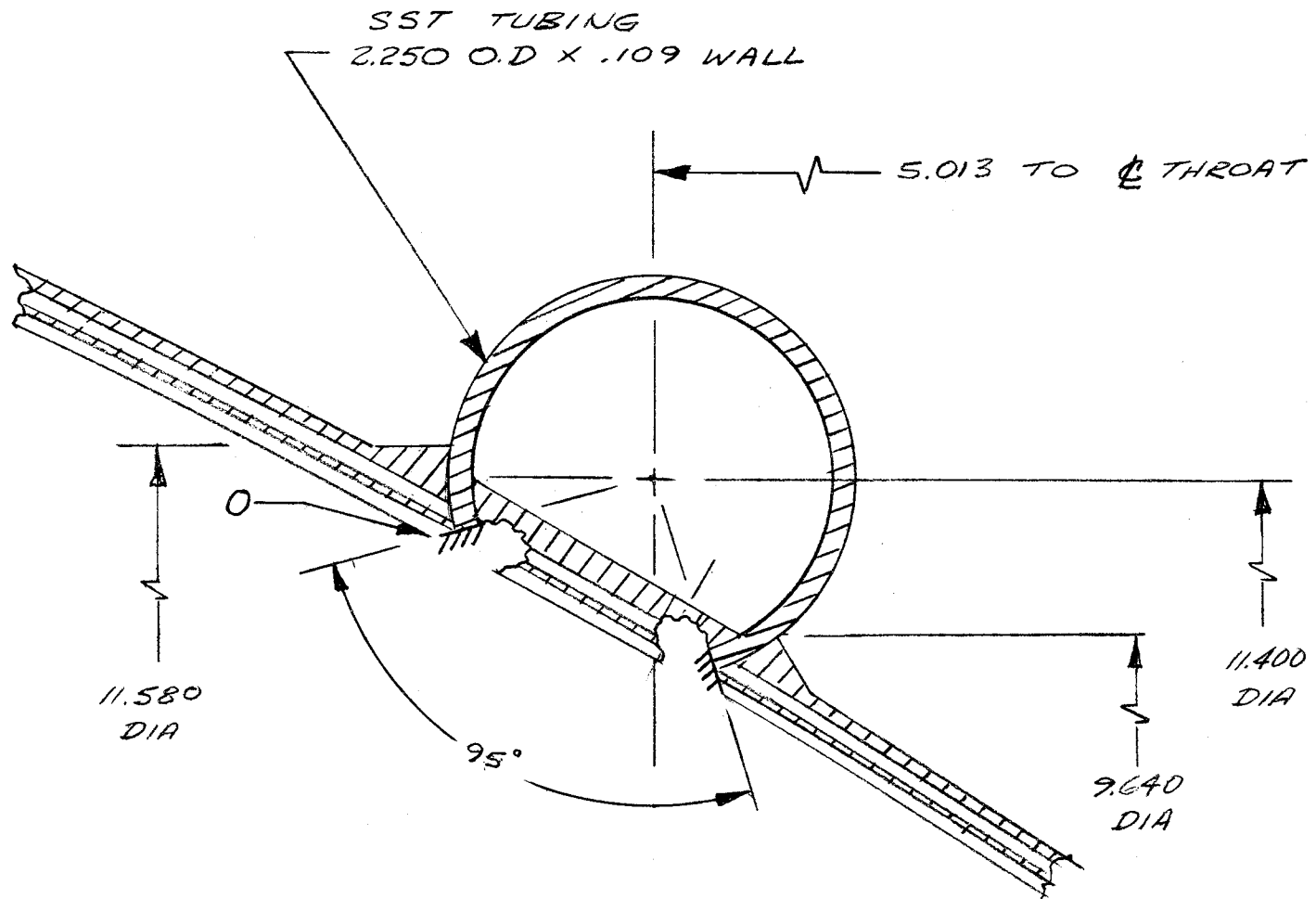
Figure 59.   Inlet Manifold
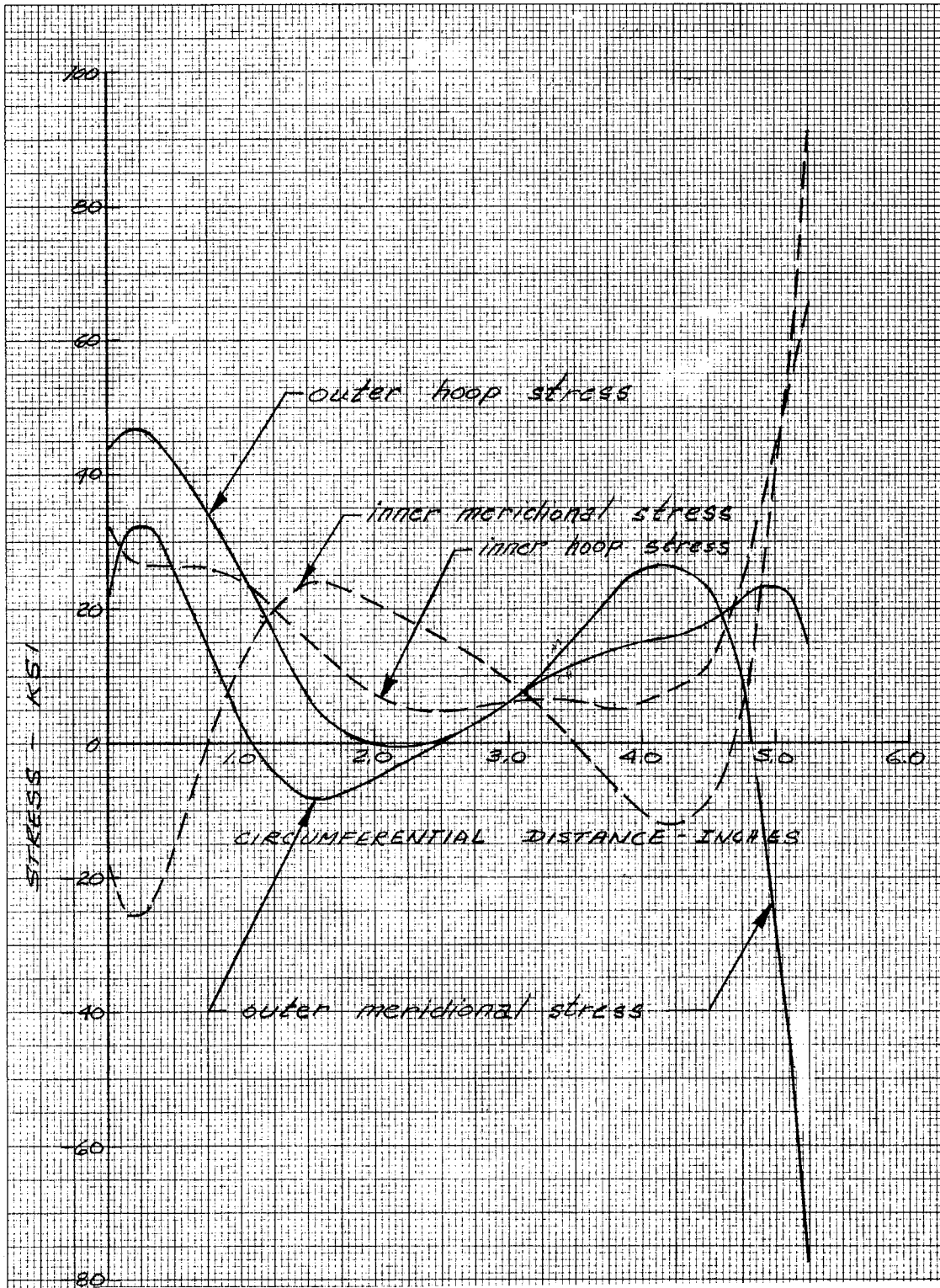
Figure 60. Stresses in the Inlet Manifold

Figure 61. Isostresses in psi in the Flange Chamber Section

Flame Liner
Thermal Barrier
Inner Wall
Channel
Outer Wall
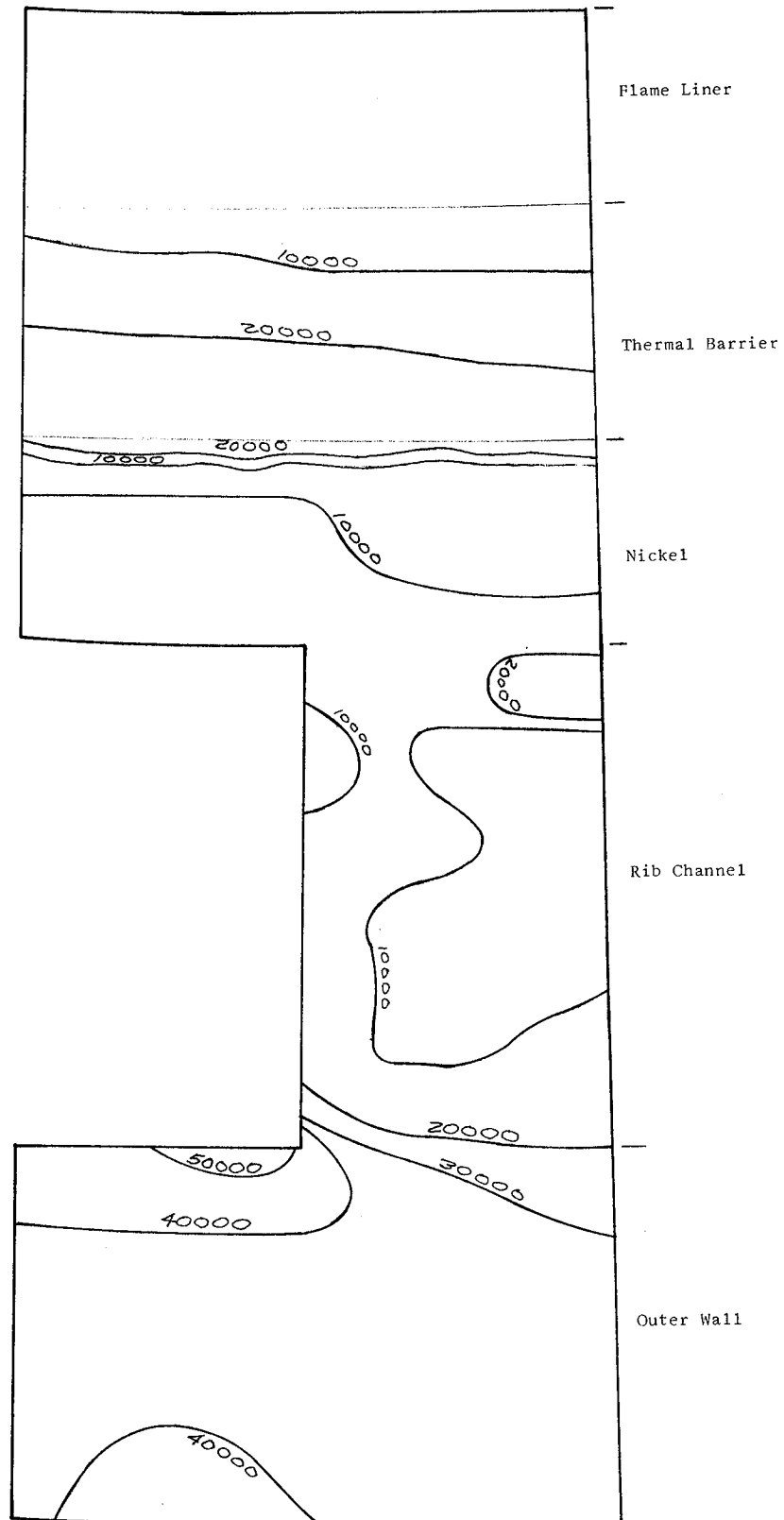
Figure 62. Isostresses in psi in the Chamber Throat Section
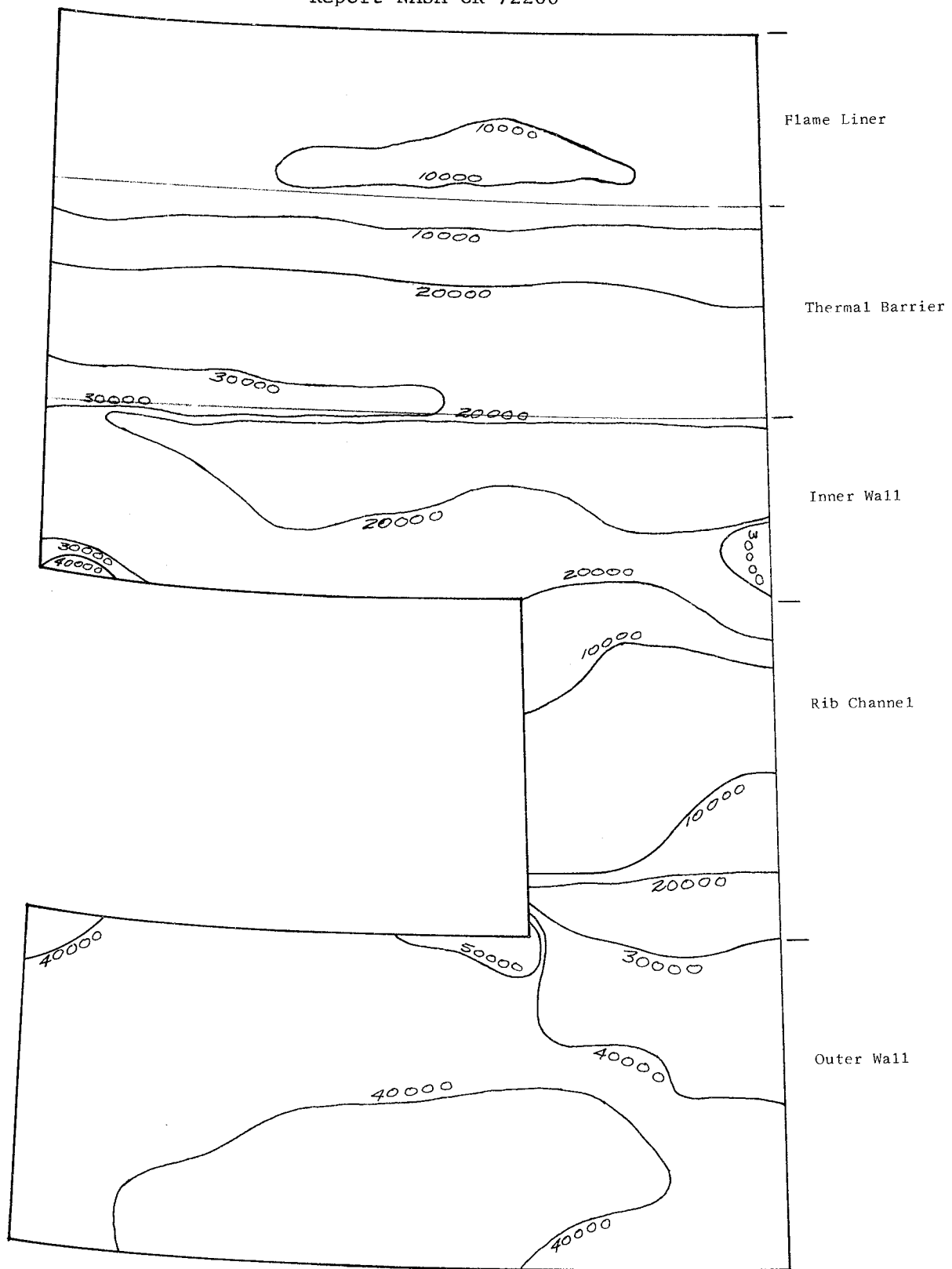
Figure 63. Isostresses in psi in the Chamber Near Flange
           Section

III, D, Stress Analysis (cont.)

The plot of stresses shown in Figure 58 indicates the maximum outer meridional of 9000 psi. The margin of safety, using room temperature yield property of 304 stainless steel, shown in Figure 55, is:

$$M.S. = \frac{35,000}{9,000} - 1 = Excessive \qquad (Ref\ 42)$$

(4) Inlet Manifold

The inlet manifold is shown in Figure 59. The manifold was run on the 1040 computer program with a pressure of 800 psia, and used fixed end boundary conditions. This results in conservative stresses in the discontinuity region of the fixed ends. The stresses are shown in Figure 60 with a maximum of 91,000 psi inner; meriodional at the fixed end.

Utilizing the ultimate material properties at a temperature of -410°F, the margin of safety is as follows:

$$M.S. = \frac{225,000}{(91,000)(1.5)} - 1 = 0.65 \qquad (Ref\ 42)$$

(5) Structural Analysis of Chamber, Forward Flange

An elastic-plastic analysis was performed on the upper section of the chamber, including the flange.

Thermal data indicates the temperature range is from 4456°F at the gas-side tungsten layer to 217°F at the outside nickel wall. Coolant temperature was given 30°F; therefore, the ambient temperature was assumed for the flange. The section was analyzed for the thermal and pressure conditions using the E11401 finite element program. Chamber pressure of 400 psia, coolant passages and manifold pressure of 650 psia were used.

III, D, Stress Analysis (cont.)

The equivalent section through bolt holes and coolant passages were determined and modulus ratio calculated. Axial force due to meridional tension was applied as a pressure to the chamber cross section and forces due to manifold pressure applied to the flange elements at joints. The results indicated that the tungsten layer as well as the composite tungsten-zirconia layers are in the plastic range with a compressive hoop stress of 3960 and 34,900 psi, respectively.

The mechanical properties of tungsten and its composites at the high temperature are not firmly established and only a few widely spread properties are available at this time.

The outside shell of electroformed nickel, 0.100-in.- thick, has substantial margin of safety, based on the elastic properties of nickel at ambient temperature. The flange machined from 304 stainless steel, has low stress values in most locations, with the exception of corners near welds where local stresses approach the yield point. The substantial margin of safety in the bulk of the structure gives promise that the flange and nickel layers will stand the load, where tungsten and its composites may be adversely affected by the repeated loading. The stress and strain values are given in Table XVI. The plot of isostresses through the flange and chamber section is given in Figure 61.

These stresses represent the values of effective stress through the elements based on the equation:

$$\sigma_e = \sqrt{\frac{1}{2}} \; \sqrt{(\sigma_r - \sigma_z)^2 + (\sigma_r - \sigma_\theta)^2 + (\sigma_z - \sigma_\theta)^2 + 6\sigma_{rz}^2}$$

Where σ_e = Effective Stress

r, z and θ = components of stress used in place of the principal stress.

TABLE XVI

STRESS AND STRAIN AT CHAMBER SECTION NEAR FLANGE

	Thickness	Location R	Z	Hoop	Stress (psi) Effective	Condition	% Strain	Temp, °F
Tungsten W	0.030	2.71	.22	3960	3640	Plastic	1.5%	4370
W-Z$_R$O$_2$	0.040	2.76	1.45	37090	31445	Plastic	0.62%	2020
Nickel Inner Wall	0.030	2.78	1.85	16080	13180	Plastic	0.35%	1099
Nickel Sand	0.090	2.87	0.28	41135	36000	Plastic	0.22%	376
Nickel Outer Wall	0.100	2.97	0.90	53356	42590	Elastic	0.14%	261
Flange – 304 SS	0.200	3.08	1.02	27900	28256	Elastic	0.11%	177

III, D, Stress Analysis (cont.)

UPPER FLANGE

Calculation of Equivalent Section Through Bolt Holes
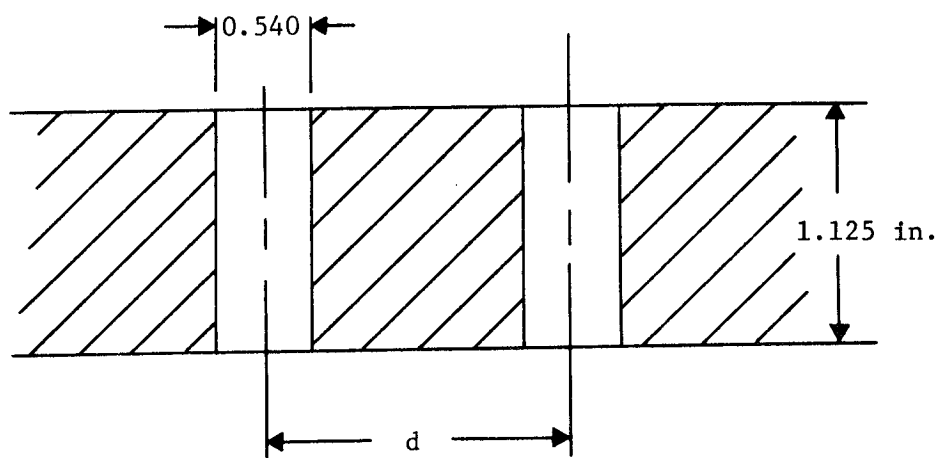
$$d = \frac{\pi D}{N}$$

d

$$d = \frac{\pi 8}{16} \quad \text{For 16 Bolts}$$

$$d = \frac{\pi}{2} = 1.571 \text{ in.} \quad \text{The effective width} = 1.571 - 0.540$$
$$= 1.031 \text{ in.}$$

$$I_c = \frac{1.031 \times 1.125^3}{12} = 0.12233 \text{ in}^4 \quad - \quad \text{Effective inertia} \qquad \text{(Ref 40)}$$

$$A = (1.125)(1.031) = 1.1599 \text{ in}^2 \quad - \quad \text{Effective area}$$

$$E I_c = E_{eq} \frac{dt^3}{12} \quad \text{(Product of Modulus and inertia)} \qquad (1)$$

$$E A_c = E_{eq} dt \quad \text{(Product of Modulus and area)} \qquad (2)$$

$$E = 28.0 \times 10^6 \text{ psi} \qquad \text{(Ref 42)}$$

III, D, Stress Analysis (cont.)

$$E \, I_c \; = \; (28 \times 10^6) \; (.12233) \; = \; 3.42524 \times 10^6$$

$$E \, A_c \; = \; (28 \times 10^6)(1.1599) \; = \; 32.477 \times 10^6$$

$$3.42524 \times 10^6 \; = \; E_{eq} \; \frac{dt^3}{12} \tag{1}$$

$$32.477 \times 10^6 \; = \; E_{eq} \; dt \tag{2}$$

From Eq. 2

$$E_{eq} \; = \; \frac{32.477 \times 10^6}{d \, t}$$

Substituting in (1)

$$3.42524 \times 10^6 \; = \; \frac{32.477 \times 10^6}{dt} \; \times \; \frac{dt^3}{12}$$

$$t^2 \; = \; \frac{(3.42524 \times 10^6)(12)}{32.477 \times 10^6}$$

$$t^2 \; = \; 1.2656$$

$$t \; = \; 1.124 \text{ in.}$$

USE 1.125 - Equivalent t

$$E_{eq} \; = \; \frac{32.477 \times 10^6}{(1.571)(1.125)}$$

$$E_{eq} \; = \; 18.376 \times 10^6 \text{ psi}$$ This value will be used for modulus in the computer input, for the stress through bolt holes section.

III, D, Stress Analysis (cont.)

Calculation of Equivalent Section Through Channel
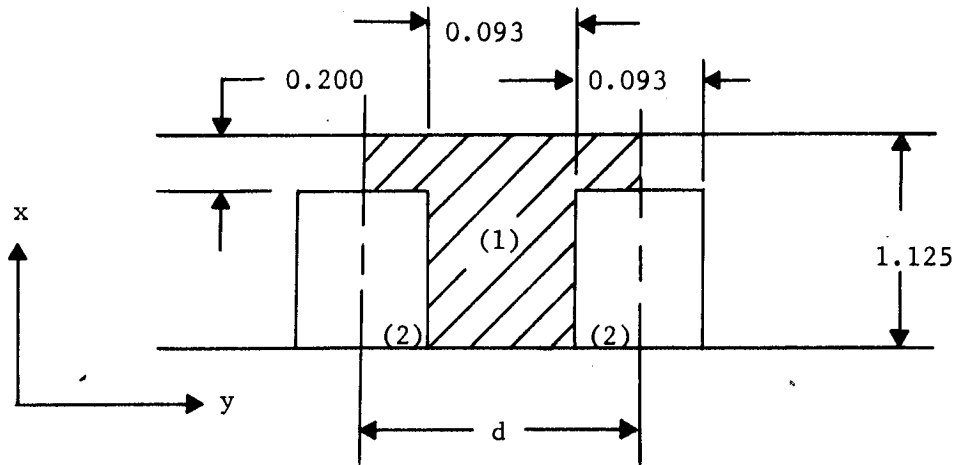
d = 0.1855 in.

h = 1.125 in.

Item	A in.^{2}	Ax in.^{3}	Ax^2 in.^{4}	I in.^{4}
1	0.2272	0.1278	0.0719	0.02201
2	-0.0860	-0.0430	-0.0199	0.00613
Σ	0.1412	0.0848	0.052	0.01588

$$\Sigma Ax / \Sigma A \;=\; \frac{0.0848}{0.1412} \;=\; 0.601 \text{ in.}$$

$$I \;=\; 0.01588 + 0.052 - 0.1412 \, (.601)^2 \qquad\qquad \text{(Ref 40)}$$

$$\;=\; 0.01688 \text{ in.}^4$$

III, D, Stress Analysis (cont.)

$$E I = E_{eq} \frac{dt^3}{12} \qquad E_{575^0} = 27.5 \times 10^6$$

$$EA = E_{eq} \, d \, t_{eq}$$

$$(0.01688) \, 27.5 \times 10^6 = E_{eq} \frac{dt^3}{12} \tag{1}$$

$$(0.1412) \, 27.5 \times 10^6 = E_{eq} \, d \, t_{eq} \tag{2}$$

From (2) $\qquad E_{eq} = \dfrac{3.883 \times 10^6}{d \, t_{eq}}$

Substitute into (1)

$$0.4642 \times 10^6 = \frac{3.883 \times 10^6}{d \, t_{eq}} \times \frac{d \, t_{eq}^3}{12}$$

$$T_{eq}^2 = \frac{0.4642 \times 12}{3.883}$$

$$t_{eq} = 1.196 = 1.2 \text{ in.} = \text{Equivalent } t$$

$$E_{eq} = \frac{3.883 \times 10^6}{(0.1855)(1.2)} = 17.44 \times 10^6 \text{ psi}$$

This value of modulus will be used in the computer program to calculate the stress value through the chamber's channel section.

III, D, Stress Analysis (cont.)

$$P = p A_s - T$$

$$p = \text{chamber pressure} = 400 \text{ psia}$$

$$A_s = \text{Area} = 22.9 \text{ in.}^2$$

$$T = \text{Thrust} = 8000 \text{ lb}$$

$$P = (400)(22.9) - 8000$$

$$P = 9160 - 8000$$

$$P = 1160 \text{ lb}$$

Pressure Input

$$q = \frac{1160}{\pi(r_0{}^2 - r_1{}^2)}$$

$$= \frac{1160}{\pi(2.95^2 - 2.7^2)} = \frac{1160}{\pi(1.4125)} = 261 \text{ lb/in.}^2$$

This load will be used as a negative pressure on the chamber cross section to compute the stress values.

III, D, Stress Analysis (cont.)

n Value Calculation for Program 14064

n = Plastic Modulus/Elastic modulus

Nickel

at 70°F

F_{tu} = 110 ksi   (Ref 10)

F_{ty} = 90 ksi

E = 30 x 10^6 psi

e = 20%

at 1200°F

F_{tu} = 20 ksi   (Ref 10)

F_{ty} = 10 ksi

e = 50%

E = 18 x 10^6 psi

at 70°F

Strain at yield = $\dfrac{90000}{30 \times 10^6}$ = 0.003 in./in.

III, D, Stress Analysis (cont.)

Slope of Plastic Range

$$m = \frac{110000 - 90000}{0.20 - 0.003} = 101500$$

$$n_1 = \frac{101500}{30 \times 10^6} = 0.0034$$

at 1200°F

$$\text{Strain at yield} = \frac{10000}{18 \times 10^6} = 0.000556$$

Slope of Plastic Range

$$m = \frac{20000 - 10000}{0.50 - 0.000556} = 20000$$

$$m_2 = \frac{20000}{18 \times 10^6} = 0.00111$$

$$n = \frac{n_1 + n_2}{2} = \frac{0.0034 + 0.00111}{2} = 0.00226$$

This ratio will be for computer program, to evaluate the stress values in the plastic range.

III, D, Stress Analysis (cont.)

Tungsten

at 4500°F

$$F_{tu} = 2.5 \times 10^3 \text{ psi} \quad \text{Ref Figure 7}$$

$$F_{ty} = 1.67 \times 10^3 \text{ psi}$$

$$E = 2.3 \times 10^6 \text{ psi}$$

$$\text{Strain at yield} = \frac{1670}{2.3 \times 10^6} = 0.000725 \text{ in./in.}$$

Slope

$$m = \frac{2500 - 1670}{0.05 - 0.000725} = \frac{830}{0.04928} = 16800$$

$$n = \frac{16800}{2.3 \times 10^6} = 0.0073$$

Tungsten Zirconia

at 4200°F

$$F_{tu} = 4.1 \times 10^3 \text{ psi}$$

$$F_{ty} = 4.1 \times 10^3 \text{ psi} \quad \text{Ref Figure 7}$$

III, D, Stress Analysis (cont.)

$$E = 2.25 \times 10^6 \text{ psi}$$

$$e = 11\%$$

$$\text{Strain at yield} = \frac{4100}{2.25 \times 10^6} = 0.00182 \text{ in./in.}$$

Slope

$$m' = \frac{4600 - 4100}{0.11 - 0.00182} = 4600$$

$$n = \frac{4600}{2.25 \times 10^6} = 0.002045 = 2.05 \times 10^{-3}$$

for 304L stainless steel at 250°F

$$F_{tu} = 85000 \text{ psi} \qquad \text{(Ref 41)}$$

$$F_{ty} = 35000 \text{ psi}$$

$$e = 50\%$$

$$E = 26.6 \times 10^6 \text{ psi}$$

$$\text{Strain at yield} = \frac{35000}{26.600 \times 10^3} = 0.00132 \text{ in./in.}$$

III, D, Stress Analysis (cont.)

Slope of Plastic Range

$$\frac{85000 - 35000}{0.50 - 0.00132} = \frac{50,000}{0.49868} = 100,000$$

$$m = \frac{100,000}{26.6 \times 10^6} = 0.00376$$

     d.   Structural Analysis, Chamber at
           Various Sections

A plastic-elastic analysis was performed on the cross section of the Advanced Regenerative-Cooled Thrust Chamber at two locations:

    (a) Cross section at the throat inside radius 1.9 in.

    (b) Cross section at a typical chamber section near the flange inside radius 2.695 in.

The sections were analyzed for the combined thermal and pressure conditions using the Finite Element Program E11401. The geometry for the throat section is shown in Figure 62. The pressure at the inside surface of the throat section is 227 psia, and in the channel, 730 psia. The temperature varied from 4216°F at the inside surface to -122°F at the channel. The thermal grid used in the analysis is shown in Figure 39. The analysis indicated that the inner layer of tungsten at the throat section was in the plastic range with a compressive hoop strain of 1.2%.

The outside layer of nickel, 0.060-in.-thick, is still in the elastic range with a maximum tensile stress of 53,100 psi.

$$\text{Margin of Safety } \frac{85,000}{53,100} -1 = +0.60$$

III, D, Stress Analysis (cont.)

This substantial margin of safety assures that the hardware will hold together, even though the tungsten may not stand up under repeated loading conditions. The stress and strain levels at the thrust in the adjacent layers of tungsten composites and nickel are tabulated in Table XVII.

The cross section at the typical chamber section near the flange had a compressive stress on the inside layer of tungsten of 8200 psi and a 1.16% strain. The geometry for this section is shown in Figure 63. The pressure at the inside surface was 400 psia and the channel was 650 psia. The temperature varied from 4456°F on the inside layer of tungsten to 190°F in the channel. The outside layer of nickel was in the elastic range, and had a maximum tensile stress of 51,200 psi.

$$\text{Margin of Safety } \frac{85,000}{51,200} = +0.66$$

From the foregoing margins of safety, it can be determined that the chamber is structurally adequate with respect to gross yielding or resultant rupture. However, because of the plastic strains on the inside surface, the chamber is low cycle fatigue limited.

The plot of isostresses through the throat section and through the chamber section near the flange are shown in Figures 62 and 63, respectively. The stress and strain levels in the adjacent layers of tungsten composites and nickel are tabulated in Table XVIII.

TABLE XVII

STRESS AND STRAIN AT CHAMBER THROAT

Material	Thickness, in.	Location Radii, in.	Stress, psi		Condition	Strain, %	Effective Stress Temp, °F
			Hoop	Effective			
Tungsten (W)	0.030	1.90 – 1.93	−10,270	−10,140	Plastic	1.2	4036
88%W – 12%ZrO$_2$	0.016	1.93 – 1.946	−21,100	−21,100	Plastic	0.87	2713
75%W – 25%ZrO$_2$	0.009	1.946 – 1.955	−25,750	−25,600	Plastic	0.74	1931
50%W – 50%ZrO$_2$	0.012	1.955 – 1.967	−35,200	−34,400	Plastic	0.44	1032
Ni – Alloy	0.002	1.967 – 1.969	−38,300	−37,700	Plastic/ Elastic	0.29	806
Ni	0.030	1.969 – 1.999	−50,200	−47,200	Plastic/ Elastic	0.24	555
Ni	0.060	1.999 – 2.059	+52,800	+53,100	Elastic	0.019	−61

TABLE XVIII

STRESS AND STRAIN AT FLANGE WITH UPPER CHAMBER SECTION

Material	Thickness, in.	Location Radii, in.	Stress, psi Hoop	Effective	Condition	Strain, %	Effective Stress Temp, °F
Tungsten (W)	0.030	2.695 - 2.725	-8,400	-8,200	Plastic	1.16	4308
88%W - 12%ZrO$_2$	0.016	2.725 - 2.741	-16,380	-15,930	Plastic	0.50	3182
75%W - 25%ZrO$_2$	0.009	2.741 - 2.750	-22,100	-21,500	Plastic	0.71	2498
50%W - 50%ZrO$_2$	0.012	2.750 - 2.762	-27,600	-27,200	Plastic	0.63	1584
Ni - Alloy	0.002	2.762 - 2.764	-28,000	-28,000	Plastic	0.59	1456
Ni	0.030	2.764 - 2.794	-16,500	-18,900	Plastic	0.20	965
Ni	0.080	2.794 - 2.874	-25,730	-24,400	Elastic	0.06	857
Ni	0.060	2.874 - 2.934	+51,200	+51,000	Elastic	0.18	243

III, D, Stress Analysis (cont.)

e.   Combustion Chamber to Nozzle
     Extension Flange

Under the mechanical loading conditions experienced by
the nozzle flange, the flange itself remains in compression and no significant
problems arise. The pressure and thrust loads which are compressive, are never
overcome by any start transient or steady-state accelerations. However,
experience on Transtage and Apollo nozzle extension flanges has shown that the
thermal problems associated with different materials and different conduc-
tivities creates significant stress conditions in the flange area. Some of
these are excessive stresses in the flanges due to differential thermal
expansion, permanent elongation of the bolts, and seal leakage.

As a result of low mechanical stress due to pressure and
thrust, and thermal stresses becoming the principal problem area, a meaningful
stress analysis cannot be conducted until a heat transfer analysis has been
completed of the complete flange joint, including nozzle extension.

III, Task I--Design and Analysis (cont.)

E. DESIGN ANALYSIS

1. Thrust Chamber Assembly

The design of the thrust chamber evolved through integration of thermal, structural, and materials and fabrication analyses while adhering to the design specifications established by NASA-LeRC. Table XIX lists the design requirements and gives the actual design data where applicable. As can be seen from this table, all except one of the requirements were satisfied. The one exception is the pressure drop in the coolant channels which is somewhat higher than desired. This was necessary to maintain reasonable tungsten and nickel temperatures.

Three parameters; coolant pressure drop, tungsten temperature and nickel temperature are the major parameters affecting the design; and since they are interdependent, a tradeoff was necessary. A design objective was established of obtaining the lowest coolant pressure drop commensurate with maintaining tungsten and nickel temperatures within upper limits. These limits were set at 4600°F and 1400°F for tungsten and nickel, respectively, and were determined on the basis of strength versus temperature of the materials.

The simplest coolant channel design would encompass a single pass. However, this was not feasible. Since hydrogen is a poor coolant at low temperatures (Ref 23), it became necessary to introduce the coolant in the nozzle region and provide for a turn-around at the aft end of the regeneratively cooled portion of the nozzle. The area ratios that were selected were 6:1 and 16:1 for the coolant inlet and turn-around, respectively. The inlet location was established on the basis of the thermal environments (in a low heat flux region) and to permit preheating of the coolant to a desired value. The turn-around at the aft end location was established on the basis of pressure drop in the coolant channels, while still maintaining acceptable wall temperatures at the transition to the ablative nozzle extension.

III, E, Design Analysis (cont.)

TABLE XIX

DESIGN REQUIREMENTS AND DATA

Item	Required	Design
Thrust	8000 lb	same
Chamber Pressure	400 psia	same
Oxidizer	Fluorine	same
Fuel	Hydrogen	same
Mixture Ratio F_2/H_2	12	same
Nozzle Expansion Ratio	60	same
Characteristic Length	25.0 in. min	25.1 in.
Nozzle Length	(a) 38.910 in. max	38.890 in.
Fuel Inlet Pressure	675 psia	760 psia
Fuel Outlet Pressure	550 psia	547 psia
Fuel Inlet Temperature	50°R	same
Chamber Diameter	(b) 5.390 in.	same
Throat Diameter	(b) 3.843 in.	same
Injector Interface	Per NASA Dwg CD 620831	same
Max tungsten temp	(c) 4600°F	4450°F
Max nickel temp	(c) 1400°F	1300°F
Max carbon-phenolic temp	(c) 4200°F	3875°F
Max silica-phenolic temp	(c) 3000°F	2125°F
Max external temp	(c) 600°F	same

(a) Corresponding to 80% of a 15° conical nozzle length.
(b) Specified by LeRC Project Manager (R. A. Duscha).
(c) These limits were established by Aerojet.

III, E, Design Analysis (cont.)

The thicknesses of the flame liner, thermal barrier, and nickel walls were determined on the basis of keeping thermal and mechanical stresses within acceptable limits at the temperature limits discussed above. The tungsten flame liner, the thermal barrier, and the inner nickel wall will operate in the plastic ranges; the bulk of the nickel, however, will be elastically stressed well within safe operating limits for the material. The plastic deformation (yielding) of the inner layers is not expected to prevent satisfactory operation of the thrust chamber, since the elongation of the materials is considerably higher than the imposed strains.

In addition to the overall design objectives and considerations discussed above, a more detailed design analysis was performed for the individual components, which make up the thrust chamber assembly. For the sake of clarity, the discussion that follows is divided into major groupings, primarily by component.

2. Chamber and Nozzle Configuration

The initial step in designing the thrust chamber involved the establishment of the internal configuration of the chamber and the nozzle that would satisfy the design requirements relative to performance and size.

A gradual transition from the chamber to the throat, incorporating large radii, will result in gradual changes in the combustion gas flow Mach number and in the convective heat transfer coefficient along the converging portion. This is especially important since the combustion products could severely attack the chamber liner if locally high heat fluxes should exist at the combustion gas-chamber wall interface. Such conditions might result if rapidly changing combustion gas flow would disturb the boundary layer. On the basis of extensive experience at Aerojet, an upstream throat blend radius equal to the throat diameter was selected. This will provide the desired gradual change in flow Mach number in the converging region.

III, E, Design Analysis (cont.)

The downstream throat blend radius was selected equal to one half the throat diameter. This selection was also based on extensive experience at Aerojet.

The nozzle contour was established by a computer program, which uses the Rao optimization technique (Ref 37) to calculate the wall contour yielding maximum thrust for a given length nozzle at a given ambient pressure. The thermodynamic properties of the gas throat geometry, and the desired exit mach number, in addition to the ambient pressure, are required as input. Starting conditions are by the Sauer method (Ref 38). The computer program prints the coordinates of the contour as well as the Mach number temperature and pressure at each point. The total axial component of thrust, mass flow, and momentum are also printed.

The Rao optimization technique uses the method of character- istics to compute the contour. The ratio of specific heats (γ) is assumed constant. Figure 64 depicts the selected configuration, which yields optimum performance within the imposed geometric limits.

3. Flame Liner

The tungsten flame liner serves the purpose of protecting the thermal barrier against the corrosive environment of the propellant combustion gases. The liner must be capable of withstanding the thermal shock upon starting, the very high temperature during firing, the shut-down purge, as well as repeated starts and stops. Furthermore, since the liner is restrained by the nickel structure (through the thermal barrier), it must be capable of withstanding the loads imposed due to differential thermal expansion.

Figure 64. Chamber and Nozzle Internal Configuration
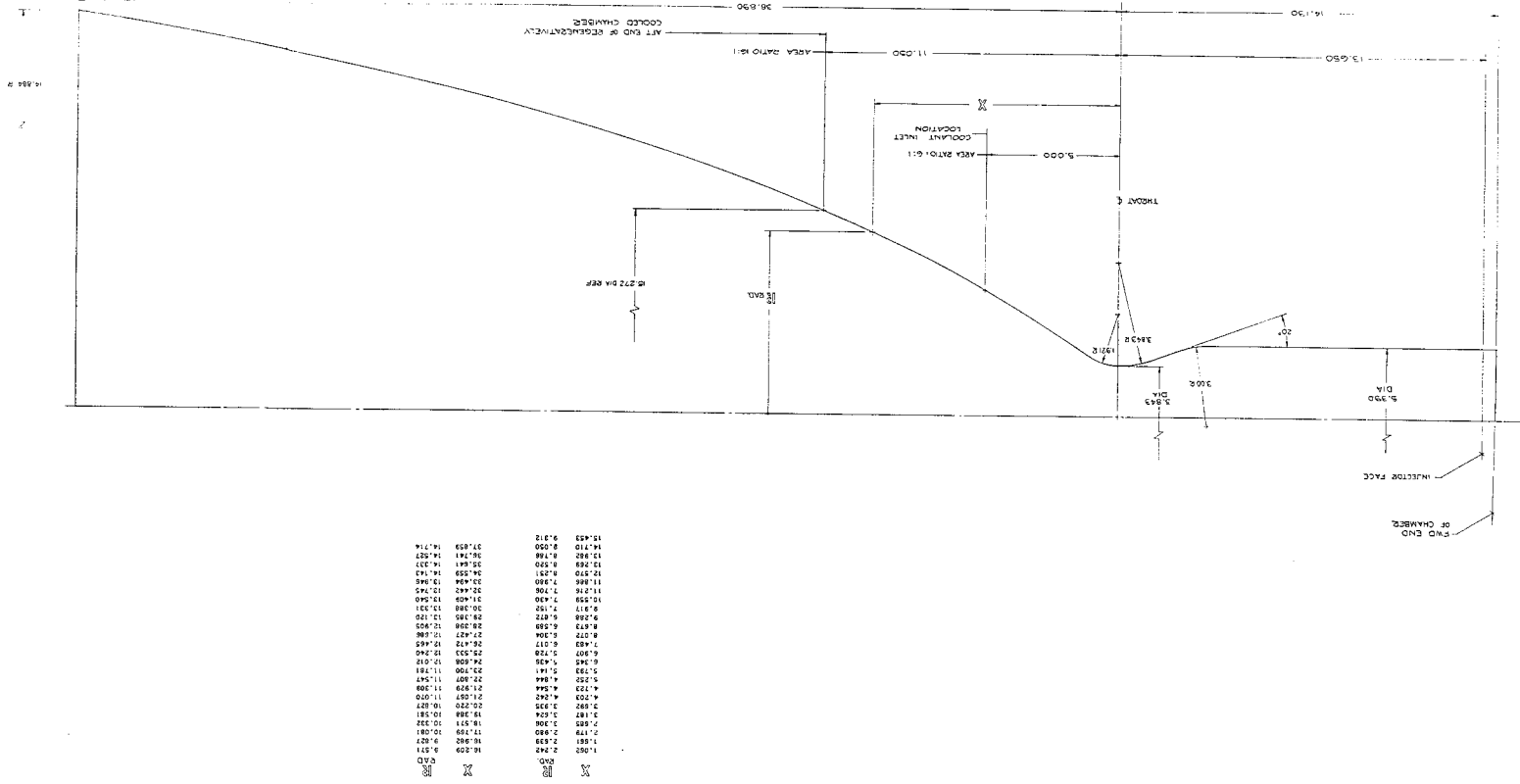
III, E, Design Analysis (cont.)

To diminish the problem of thermal shock during start, and the possibility of cracking, the thermal gradient through the flame liner should be kept as low as possible. For that reason, the thickness of the flame liner was selected as 0.030 in.

Failure, if it occurs, is expected to be due to low cycle fatigue. This cannot be predicted as there is no data on low cycle fatigue of tungsten and must be determined by testing.

4. Thermal Barrier

On the basis of preliminary calculations of heat fluxes, thermal resistance values, and wall temperatures, a tentative selection of a tungsten-zirconia composite coating was made. Two conditions were considered critical, namely (a) the differential thermal expansion at the interfaces within the thermal barrier, and (b) the thermal gradients through the various layers. To minimize differential thermal expansions and thermal gradients, a gradated thermal barrier coating was required. Graphs were made of thermal expansion vs temperature for the materials comprising the chamber wall, temperatures were calculated at the interfaces and were super-imposed on the graphs. Figures 65, 66, and 67 show the conditions for final selection for the chamber region, throat region, and region at the coolant inlet location (area ratio 6:1). It appears that the critical condition is the thermal gradient through the outer-most layer ($50W-50ZrO_2$). Differential thermal expansion values seem to be reasonable and no interlaminar shear failures are anticipated. It is, however, not possible to reduce the thermal gradient by any appreciable amount and still maintain satisfactory temperatures of the tungsten flame liner and nickel wall.
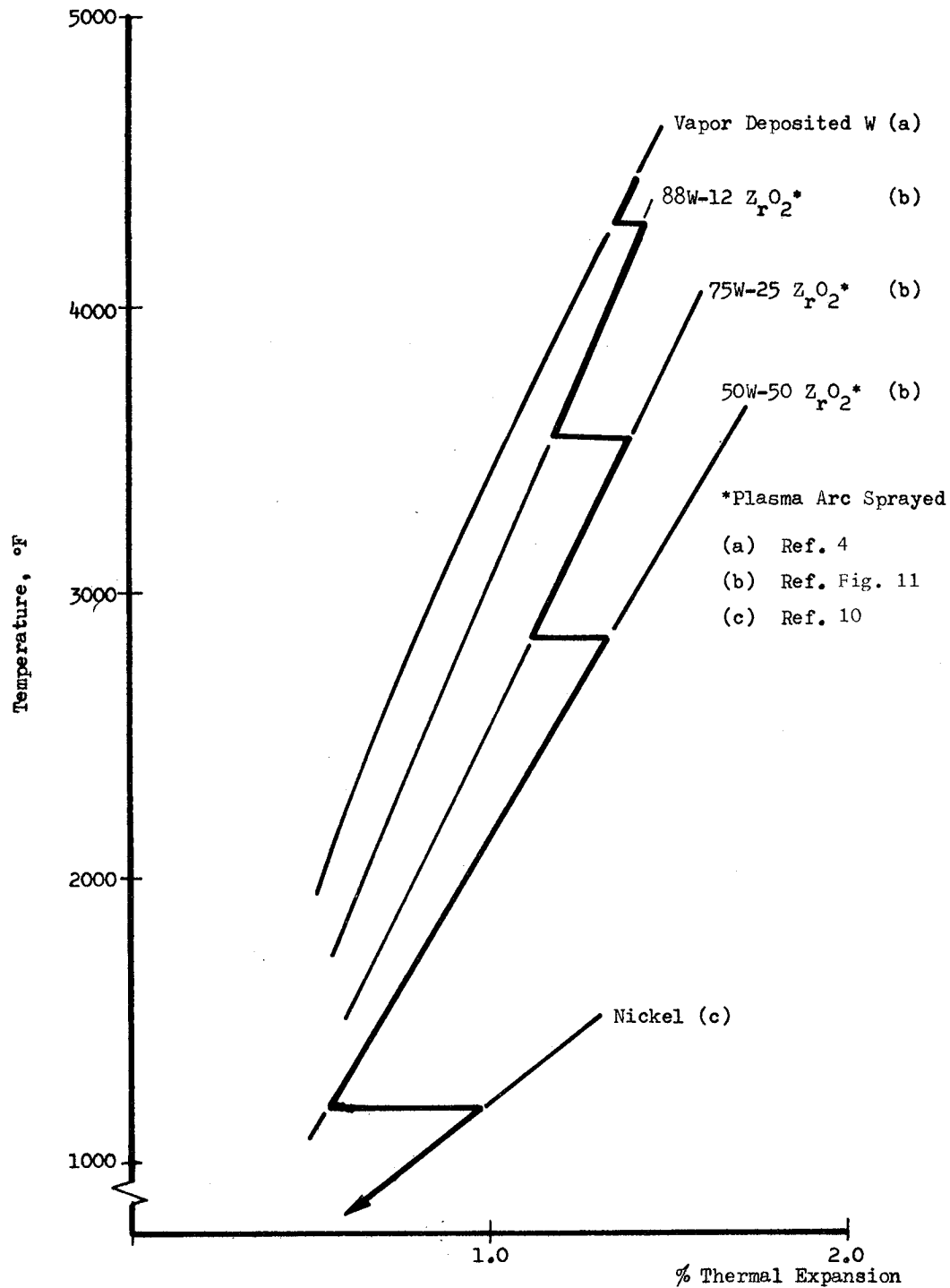
Figure 65. Flame Liner and Thermal Barrier Temperature
Gradients and Differential Thermal Expansion -
Chamber
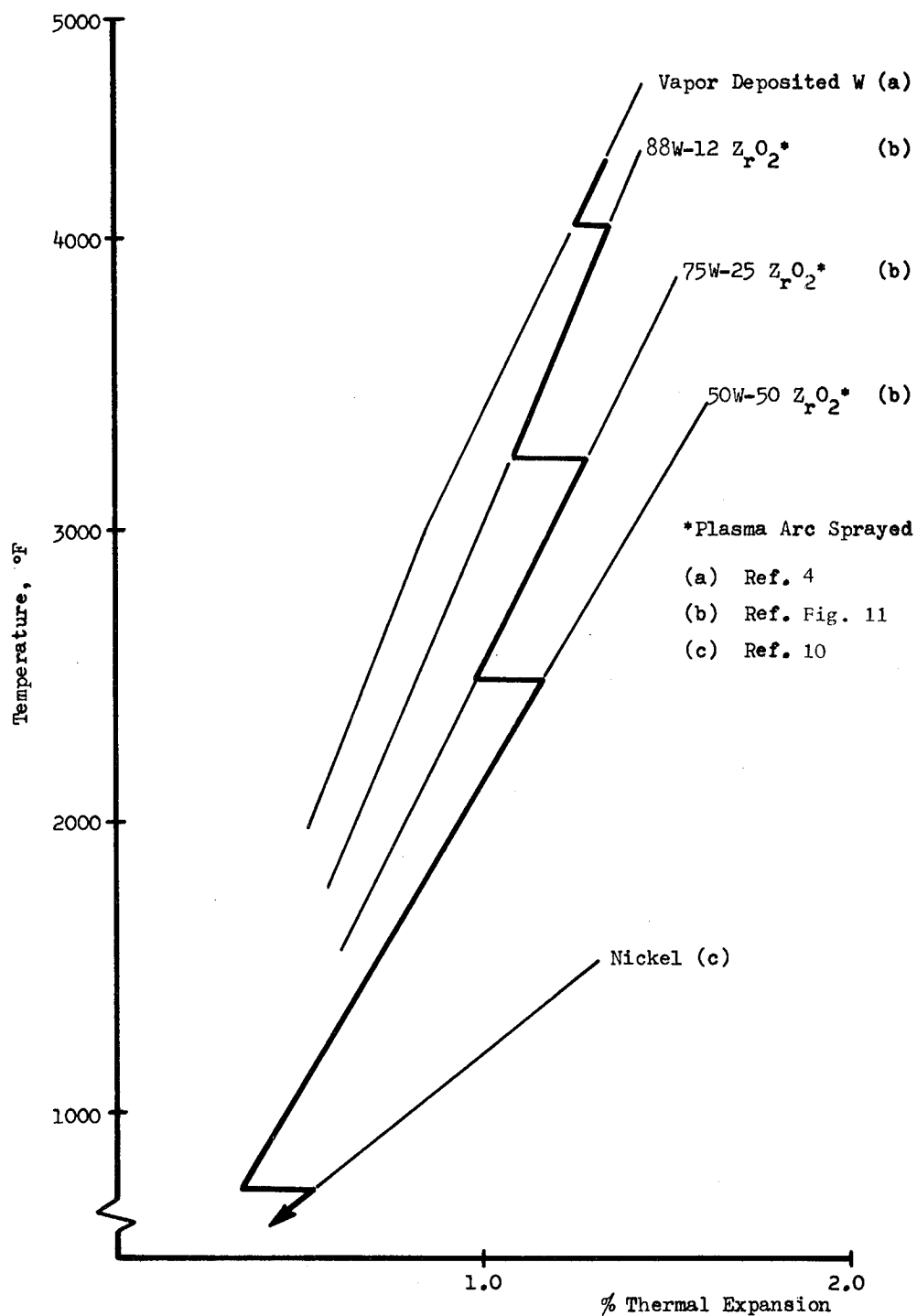
Figure 66. Flame Liner and Thermal Barrier Temperature
Gradients and Differential Thermal Expansion -
Throat
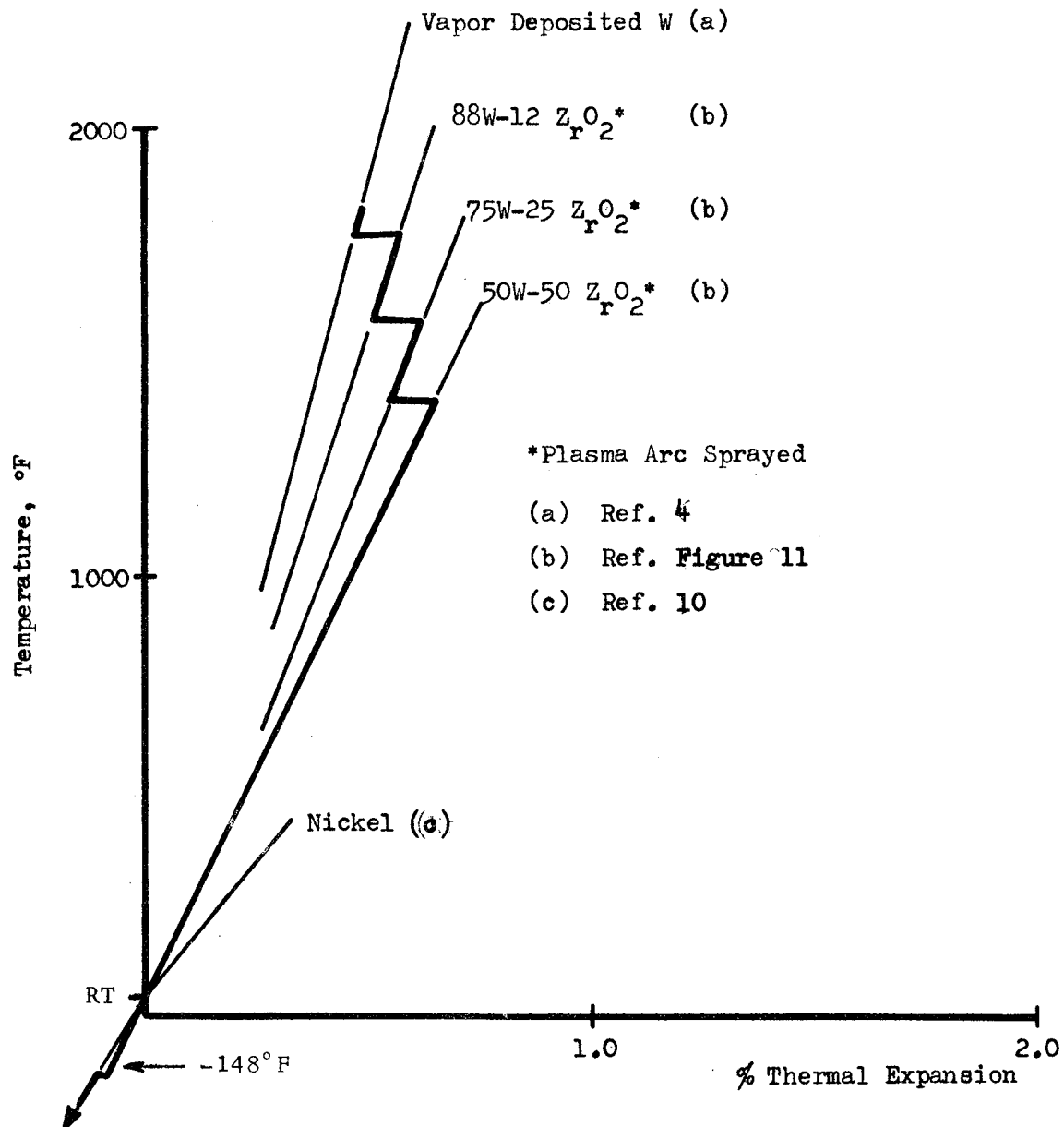
Figure 67. Flame Liner and Thermal Barrier Temperature
Gradients and Differential Thermal Expansion –
Coolant Inlet

III, E, Design Analysis (cont.)

As a consequence of the high thermal gradient through the composite thermal barrier wall, the stresses are rather high and will exceed the allowable. The strains on the other hand are considerably lower than the elongation of the material at the temperatures involved and therefore the material will yield and relieve the high stresses.

The thermal expansion values for the gradated tungsten-zirconia were based on linear interpolation of the values for plasma-arc-sprayed tungsten and plasma-arc-sprayed zirconia, respectively. The percents indicated are weight percents, the thermal expansion values, however, were interpolated on a volume percent basis.

The thicknesses of the thermal barrier layers were determined by adhering to the criteria established above and further considering ease of application. All except one of the layers are of constant thickness and they are as near as possible in thicknesses that are multiples of 0.004 in., since that is the nominal thickness of one pass application. Table XX lists the important parameters of the thermal barrier and also of the vapor deposited tungsten flame liner.

5. Coolant Channel Configuration

The coolant channel design is primarily a function of coolant velocity requirements, which are discussed in detail in the Heat Transfer Analysis Section. The electroforming process imposed some restrictions on the design discussed in the Fabrication Analysis Section and briefly for reference are:

a. Maximum channel height 0.10 in.
b. Maximum rib height to width ratio 2:1.
c. Rib width must be constant (not tapered).
d. Ribs can run axially and radially only.

TABLE XX

FLAME LINER AND THERMAL BARRIER DATA

Coating	Thermal Conduct.(k) Btu/in.sec-°F x 10^{-5} At Operating Temperatures	Chamber and Throat Region		Fuel Inlet Region	
		Thickness(t), in.	Resistance(t/k) in.^{2}-sec-°F Btu	(t) in.	(t/k) in.^{2}-sec-°F Btu
Vapor Deposited W	132.0[a]	0.030	22.7	0.030	22.7
88W-12ZrO$_2$*	16.5[b]	0.016	97.0	0.016	97.0
75W-25ZrO$_2$*	9.7[b]	0.009	92.8	0.009	92.8
50W-50ZrO$_2$*	5.6[b]	0.012	214.1	0.044	786.0
TOTAL		0.067	426.6	0.099	998.5

*Weight Percent

(a) Reference Figure 32
(b) Reference Figure 10

III, E, Design Analysis (cont.)

The "growing in" of inserts, as shown in Figure 23, to facili-
tate attachment of flanges or manifolds was considered impractical, therefore,
a local buildup of nickel was required to provide a weld joint that is accessible.

A result of inability to taper rib width is the abrupt change
in channel flow area immediately upstream of the inlet slots. This is not
serious in this design as the coolant velocity is fairly low at this location;
however, to reduce the turbulence due to the abrupt change in cross section,
the rib width is varied in steps with a thin splitter at the convergent section.

A curved diffuser, as shown in Figure 68, which would result
in approximately 20% of the velocity head being regained was considered but also
proved to be impractical for fabrication. More efficient diffuser passages with
an 80 to 90% potential recovery of the velocity head could be incorporated in
a flight design by integrating the interface between the chamber and injector.

6.   Manifolds and Attachment Flanges

The coolant inlet and outlet manifolds were largely patterned
after the fuel inlet manifold shown on the injector Drawing CD 620597. The
torus diameter for both inlet and outlet manifolds were selected the same as
that of the injector manifold and two supply outlet connections were attached
in the form of tubes with weld joints to be compatible with the injector mani-
fold supply connections. By making the inlet and outlet manifolds of the same
size, tooling costs can be kept low. Only one basic stamping is required. The
manifolds are equipped with welded on bosses for standard AN fittings for
monitoring of pressures and temperatures.
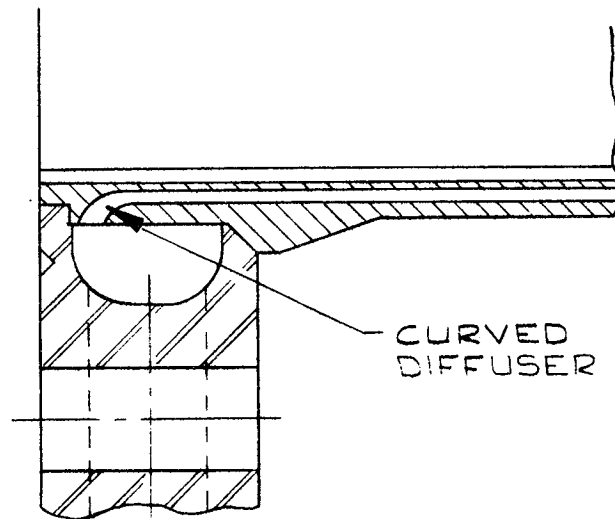
Figure 68. Coolant Outlet Diffuser Configuration

III, E, Design Analysis (cont.)

The outlet manifold is welded to the forward chamber flange which is designed to mate with the injector flange. The coolant flows into the manifold through 16 holes drilled radially between the mounting bolt holes. The aft flange configuration is governed by the nozzle extension design. The selected approach consists of an ablative extension. A step joint is incorporated to prevent hot gas flow in the seal region. The aft face of the chamber and flange in contact with the ablative material is provided with a thermal barrier coating of zirconium oxide. This flange is not required unless a nozzle extension is to be evaluated, and is not planned for fabrication.

To prevent high local heat fluxes to the thermal barrier during fabrication, the forward and aft flanges and the coolant inlet manifold will all be attached to the basic chamber by electron beam welding. This requires special consideration to the joint design. The joints must be accessible to the E.B. equipment and small joint clearances must be maintained. This has been accomplished in that both the forward flange and the inlet manifold can be positioned axially until the desired joint gap is obtained at the mating conical surfaces. The forward flange has extra stock at the forward face for that purpose and also to permit machining the forward face after welding to the chamber, within the required perpendicularity and flatness tolerances. Figure 69 shows the regeneratively cooled thrust chamber assembly. Its calculated weight is 95 lb, including the aft flange. The weight distribution is as follows:

THRUST CHAMBER

Component	Volume, in.^{3}	Weight, lb
Tungsten Flame Liner	18.41	12.90
Thermal Barrier		
a) $88W-12ZrO_2$	9.88	5.25
b) $75W-25ZrO_2$	5.60	2.75
c) $50W-50ZrO_2$	17.88	6.88

RIB WIDTH .065

RIB WIDTH .040

10.800

11.600

12.390

9.40

RIB & CHANNEL DETAIL

THROAT ₵

3.843 DIA

5.390 DIA

8.000 DIA

11.400 DIA

11.400 DIA

16 HOLES EQ SP
(FOR .50 DIA BOLTS)

SST

INJECTOR
(NASA DWG CD620597)

OUTLET

INLET

SST
2.250 O.D. x
2 PLACES

14.130

.250
24
EQ

25.180

176-1

W .030 THICK
88W-12 ZrO₂ .016 THICK
75W-25 ZrO₂ .009 THICK
50W-50 ZrO₂
(A) .012 THICK FROM FORWARD END
TO THROAT.
(B) THICKNESS VARIES UNIFORMLY
FROM .012 THICK AT THROAT
TO .044 THICK AT INLET.
(C) .044 THICK FROM INLET TO AFT END.
PLASMA ARC SPRAYED NICKEL .003 THICK
ELECTRO DEPOSITED NICKEL
CHANNEL HEIGHTS:
(A) .080 FROM FORWARD END TO CYLINDRICAL
TO CONICAL TRANSITION OF CHAMBER.
(B) CONSTANT TAPER HEIGHT FROM .080 TO .060
FROM CYLINDRICAL/CONICAL TRANSITION OF
CHAMBER TO THROAT.
(C) CONSTANT TAPER HEIGHT FROM .060 TO .100
FROM THROAT TO AFT END.

.030
.060
.090

2°30' 48 PLACES
1°30' 48 PLACES
2°30' 48 PLACES
3°45' 48 PLACES

COATING & CHANNEL DETAIL
SCALE NONE

.050 THK
ZrO₂
15.272 DIA
15.850 DIA

CARBON PHENOLIC WB 8217 (TAPER FROM .650 AT FWD END
TO .450 AT EXIT)
WRAP ORIENTATION
PARALLEL TO ₵

29.768
DIA

WALL
).388
DIA
SST

BOLTS
CES
CED

GLASS CLOTH
& ROVING

SILICA-PHENOLIC
(FLAT WRAP)
WB 2230
(.350 THICK)

27.840

Figure 69.   Regeneratively Cooled Thrust Chamber Assembly

III, E, Design Analysis (cont.)

Component	Volume, in.^{3}	Weight, lb
Nickel Structure		
a) Inner wall*	20.67	6.64
b) Outer wall	38.74	12.43
c) Ribs	19.53	6.27
d) Forward end	2.60	0.83
e) Inlet doubler	7.91	2.54
f) Aft end	4.10	1.32
Inlet Manifold	19.75	5.67
Outlet Manifold	22.15	6.35
Forward Flange	40.72	11.70
Aft Flange	44.83	12.87
Total Chamber Weight		94.40

*Includes 0.003-in. thick plasma-arc-sprayed nickel

NOZZLE EXTENSION

Component	Volume, in.^{3}	Weight, lb
Carbon Phenolic	1188.0	61.8
Silica Phenolic	796.0	51.0
Glass Phenolic	28.3	2.0
Steel Flange	31.5	9.0
Total Weight		123.8

7.   Nozzle Extension

a.   Selected Design

The nozzle extension extends from an area ratio of 16:1 to 60:1 as shown in Figure 70. The nozzle extension consists of a
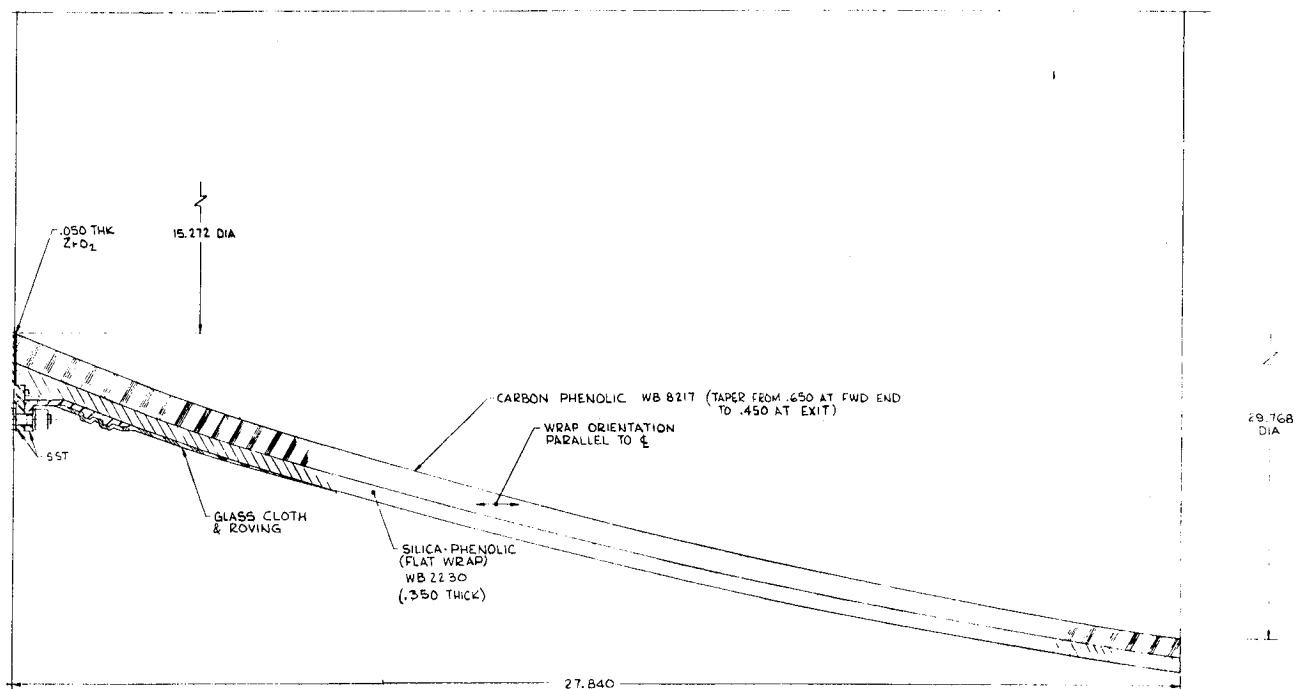
Figure 70. Ablative Nozzle Extension

III, E, Design Analysis (cont.)

carbon-reinforced-phenolic flame liner, a silica-reinforced phenolic insulation, a stainless-steel attachment flange and phenolic-impregnated glass cloth and roving retaining the flange. It was designed to withstand 180 sec of firing duration, under either vacuum or high altitude conditions. The thicknesses of materials were selected such as to be within safe operating limits for each. The temperature histories for the flame surface, interface between liner and insulation, and outside surface are shown in the thermal analysis section.

Because of the variable heat flux along the length of the nozzle, the thickness of the flame liner varies from 0.65 in. at the forward end to 0.45 in. at the aft end. This will result in a uniform temperature at the backside of the liner of about 2100°F. The maximum flame surface temperature is about 3900°F (at the forward end). The flame liner possesses adequate strength even when charred through.

The silica-reinforced phenolic insulation is of a constant thickness of 0.35 in. The thickness was established by imposing a maximum backside temperature of 500°F at the area adjoining the flange. At higher temperatures the adhesive bond between the flange and insulation and the resin at the glass roving – insulation interface will degrade and the structural integrity of the extension would be impaired. The aft end of the extension will experience a maximum external temperature of about 600°F. This condition, however, will not be detrimental, since there is adequate structural strength remaining.

The nozzle extension is bolted to the chamber by means of a stainless-steel flange with a conical sleeve installed around the forward end of the nozzle extension. The sleeve is provided with grooves that will ensure a positive locking in place when the glass cloth and roving is over-wrapped. The glass structure extends five inches downstream of the sleeve.

III, E, Design Analysis (cont.)

A silicone rubber O-ring installed in a relatively cool region will provide a gas-tight seal between the chamber and the nozzle extension. The weight of the ablative nozzle extension is approximately 125 lb.

b. Alternative Design

For durations much longer than 180 sec or for thermally more severe duty cycles, ablative nozzle extensions tend to be excessively heavy and other approaches should be considered. A suitable candidate would be a radiation-cooled nozzle extension made of a fibrous graphite. An example of such a fibrous graphite is AGCarb-101*, which was developed and tested very successfully in a fluorinated oxidizer thrust chamber materials evaluation program under Contract AF 04(611)-10918. The fibrous graphite is not sensitive to thermal shock and can, therefore, be used as a free-standing structure. The most difficult problem associated with a radiation cooled nozzle extension is the attachment to the chamber. The heat flux to the flange must be restricted, and at the same time the insulating medium must be capable of transmitting the imposed loads from the flame liner to the flange. Figure 71 shows a concept of a radiation-cooled fibrous graphite nozzle extension.

8. Fabrication Drawings

The thrust chamber design has progressed to a state where geometry and materials have been finalized. Fabrication drawings have been prepared satisfying the requirements of Specification MIL-D-1000. Preliminary copies are being forwarded to NASA/LeRC under separate cover. Finalized drawings and additional detail drawings are planned for the initial stage of Task II.

---

*AGCarb-101 is an Aerojet-developed fibrous graphite product.

ZIRCONIUM OXIDE

GRAFOIL
LAMINATE

AG CARB-101

29.768
DIA

GLASS ROVING

STAINLESS STEEL
SPLIT FLANGE

STAINLESS STEEL
BACK-UP RING
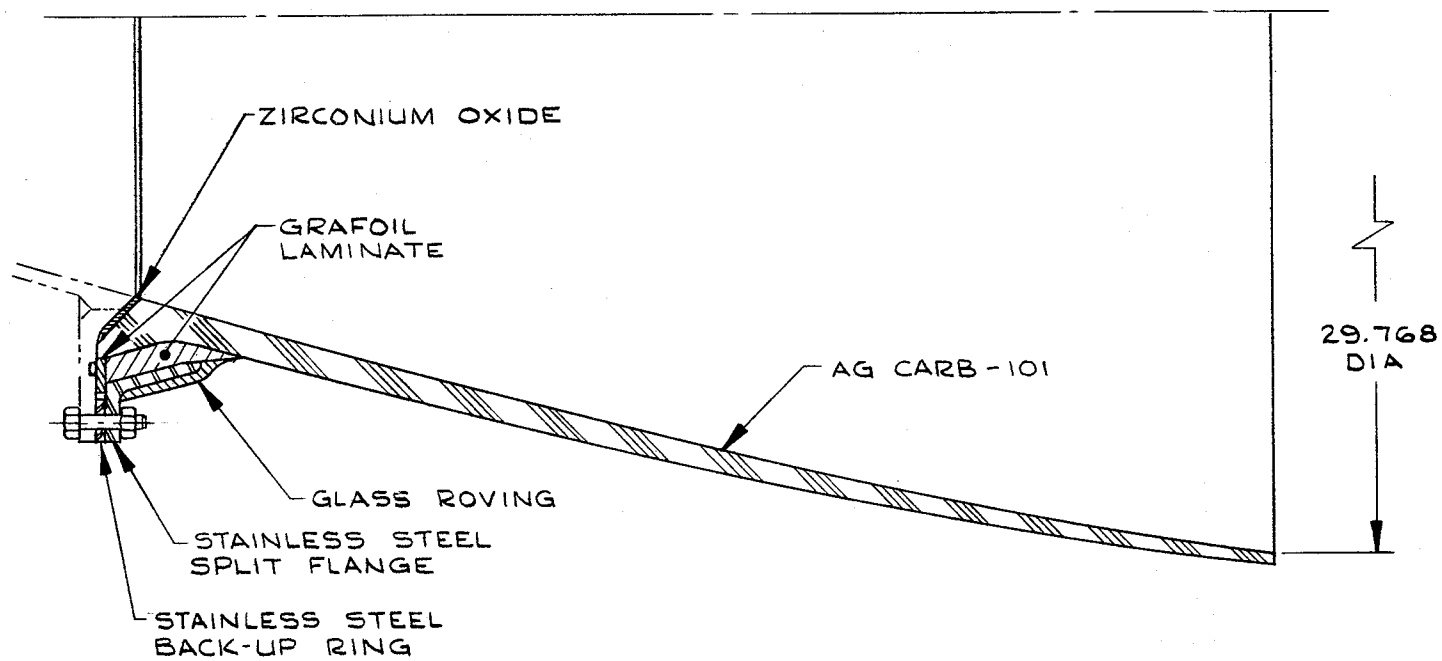
Figure 71.   Nozzle Extension - Alternative Design

IV. CONCLUSIONS AND RECOMMENDATIONS

A regeneratively cooled thrust chamber has been designed to operate with fluorine/hydrogen propellants with a mixture ratio of 12 at a 400 psia chamber pressure and at a thrust level of 8000 lb without requiring film cooling. A demonstration chamber can be built with an independent coolant supply in which the pressure drop between the coolant inlet and outlet will be between 200 and 225 psi. A flight-type design, requiring modification of the chamber to injector interface, can be evolved in which the pressure drop can be lowered to approximately 175 psi.

The materials selected are those most compatible with the operating environments of an LF_2/LH_2 engine. The processes for fabrication are not conventional but are nevertheless within the state of the art and were selected in conjunction with the basic design approach.

The results of heat transfer analyses and of thermal and mechanical stress analyses indicate that a satisfactory performance can be expected. The analyses show that the basic electroformed nickel structure and the stainless-steel manifolds and flanges have high margins of safety. The flame liner and thermal barrier are stressed beyond the elastic limits; however, the imposed strains are much lower than the elongation of the materials and therefore plastic deformation will occur, relieving highly stressed areas.

The start transient is not expected to adversely affect the tungsten flame liner because of the low thermal gradient through it. A possible problem is associated with the shutdown transient. During a chamber purge, the inner surface of the tungsten flame liner will be rapidly cooled and surface tensile cracks may develop. These cracks would, however, not propagate on repeated firings since the outer tungsten is in compression during this transient and the entire tungsten liner is in compression during steady state operation. Repeated cycling might eventually lead to failure.

/ IV, Conclusions and Recommendations (cont.)

Because of the possible adverse condition during shutdown, it is
recommended that NASA carefully review the shutdown procedure and that an
evaluation of the effects on the tungsten flame liner be performed.

The fabrication analysis performed indicates that the design is produc-
ible. As fabrication proceeds, design changes required will be incorporated
and changes in processes or fabrication procedures will be recorded for inclu-
sion in the final report. In addition, a photographic record will be made
of all major fabrication steps.

As previously noted, the physical properties of electroformed nickel
vary over a wide range. For example, the ultimate tensile strength can vary
from 55,000 psi to 215,000 psi depending on the condition of the bath and
many other factors. For any additional thrust chambers to be produced of
electroformed nickel it is recommended that additional testing be performed
to establish short time tensile properties at 1000°F and above. In this
investigation where the electroforming process is considered propriatory, it
is not possible to apply process controls to insure required properties
throughout the entire structure. Also, vapor-deposited tungsten and plasma-
sprayed tungsten-zirconia composites are relatively new material types and
there is little physical and mechanical property data available.

To complete the thrust chamber design, it was necessary to make assump-
tions and to extrapolate data from sililar materials; wrought nickel, wrought
tungsten, and pressed and sintered tungsten. All data used was considered
conservative and it is considered that the proposed thrust chamber should be
fabricable and should operate successfully. However, there is a small possi-
bility of problems arising in unanticipated areas due to the lack of complete
material data.

IV, Conclusions and Recommendations (cont.)

Because of the above possibility, it is recommended that several experimental programs be conducted before the design and fabrication of future thrust chambers. These programs should be designed to determine the properties of electroformed nickel, vapor-deposited tungsten, plasma-sprayed tungsten zirconia thermal barriers, bond strengths and thermal characteristics of the composite. From these programs, material and fabrication specifications should be prepared to control the processes.

It is also recommended that, since there is some uncertainty in the gas-side boundary conditions for fluorine/hydrogen propellants, tests be conducted prior to firing the chamber to resolve these uncertainties. This may be accomplished by instrumented workhorse chamber tests that are designed to obtain data from which the chamber circumferential and axial heat flux variations may be determined. These tests should be performed at the chamber pressures and injector mixture ratios at which coated chamber testing will be conducted, and should use the same injector. In this way, the actual heat fluxes to which the coated chamber will be subjected can be established as well as the effects of the injector on the thermal environment.

The recombination effect is a second area of uncertainty. This effect has been experimentally noted to increase the chamber wall heat flux by the exothermal production of chemical energy in the boundary layer, and is peculiar to hydrogen/fluorine and similar high energy propellant systems. The magnitude of this effect is unknown for LF_2/LH_2 at this time. Because thermo-dynamic considerations indicate that the magnitude of this effect will depend on the chamber wall temperature (i.e., enthalpy potential across the boundary layer), it is further recommended that high wall temperature chamber data be obtained in addition to the workhorse chamber data, which will be obtained at low wall temperatures. This might be accomplished by conducting water-cooled tests with the coated chamber.

IV, Conclusions and Recommendations (cont.)

Water cooling would permit much lower channel temperatures than occur with hydrogen while the coating temperature remains relatively unaffected. Using water cooling will also permit the coolant pressure drop to be determined experimentally independent of the heating environment and will provide more meaningful wall temperature data. The chamber operating parameters for water regenerative cooling with the coated chamber are shown in Table XII. One or two tests should be adequate to establish the magnitude of the recombination effect at high chamber wall temperature.

NOMENCLATURE

A	area
C_G	film coefficient constant
h	convection film coefficient
i	enthalpy
P	pressure
Pr	Prandtl number
Q	heat flux
Re	Reynolds number
St	Stanton number
T	temperature
V	velocity
$\dot{w}_p$	propellant flow rate
α	absorptivity
ρ	density
ε	emissivity
ν	viscosity
γ	ratio of specific heats

SUBSCRIPTS

B	bulk
c	convection
d	chamber diameter
g	gas-side
i	enthalpy potential
Zero	stagnation
r	recovery
RAD	radiation
s	stream
w	wall

Nomenclature (cont.)

1D   one-dimensional

2D   two-dimensional

SUPERSCRIPTS

*   reference enthalpy

References

1. Batchelor, J. D., McCormick, S. W., Scheffee, R. S., and Ólcott, E. S., Gas-Metal Reactions in Rocket Nozzles, Report ASD-TR-62-327, Part I, June 1962.

2. Crandall, W. B. and J. R. Tinklepaugh, Cermets, Reinhold Publishing Corp., 1966.

3. Klapp, William D., Walter R. Witzke, and Peter L. Raffo, "Mechanical Properties of Dilute Tungsten Rhenium Alloys", Lewis Research Center, Cleveland, Ohio, NASA TND-3483.

4. Materials and Fabrication Data Sheets, Aerojet-General Corporation.

5. Harrington, D. G., and Adair, S. E., Coated Metallic Thrust Chambers, Report 652/SA4-2.2-Fl, Vol. 2, Aerojet-General Corporation, June 1963.

6. "The Mechanical Properties of Pressed and Sintered Tungsten of Various Densities", Polaris Propulsion Development Report 475, February 1963.

7. Norton Refractories Division Bulletin CP 14.1, March 1957.

8. Kura, J. G., et al, The Making of Nickel and Nickel-Alloy Shapes by Casting, Powder Metallurgy, Electroforming, Chemical Vapor Deposition, and Metal Spraying, NASA Technical Memorandum NASA TM-X-53430, October 1965.

9. Safranek, W. H., Redstone Scientific Information Center Report 210, "A Survey of Electroforming for Fabricating Structures", Battelle Memorial Institute (August 1964) (RSICO743).

10. International Nickel Company Technical Bulletin T-15, February 1960.

11. Report to Aerojet-General Corp., P.O. No. S-426922-OP, "Compression Properties of Silver-Infiltrated and Pressed-and-Sintered Tungsten at Elevated Temperatures", Southern Research Institute, Birmingham, Ala., 1964.

12. Taylor, J. T. and Boone, D. H., Tensile Properties of Pyrolytic Tungsten from 1370° to 2980°C in Vacuum, Technical Report No. 32-463, Jet Propulsion Laboratory, California Institute of Technology, Pasadena, California, 1964.

13. Bartz, D. R., A Simple Equation for Rapid Estimation of Rocket Nozzle Convective Heat Transfer Coefficients, Jet Propulsion 27, 1957, pp. 49-51.

References (cont.)

14. Ewen, R. L., Block, P., and Van Huff, N. E., A Unified Boundary Layer Approach to Convective Heat Transfer in Thrust Chambers, Aerojet-General Report LR671502N. A Research Suggestion to NASA Lewis Research Center, February 1967.

15. Ziebland, H., "Radiation and Convection in High Energy Liquid Propellant Rocket Engines", International Developments in Heat Transfer: Part I, 1961, pp. 165-173.

16. Arbit, H. A., and Clapp, S. D., "Final Report: Fluorine-Hydrogen Performance Evaluation", Rocketdyne, Report R-6636-1, Contract No. NASw-1229, July 1966.

17. Eckert, E. R. G., and Drake, R. M., "Heat and Mass Transfer", McGraw-Hill, New York, 1959.

18. "Research on a Hydrogen-Fluorine Propulsion System", Pratt and Whitney Aircraft, Report NASA CR-72074, Contract NASw-754, October 1966.

19. "Survey of Thrust Chamber Film Coefficient Correlations", Aerojet-General Unpublished, 1967.

20. Schact, R. L., Quentmeyer, R. J., and Jones, W. L., "Experimental Investigation of Hot Gas-Side Heat Transfer R tes for a Hydrogen-Oxygen Rocket", NASA TN D-2832, June 1965.

21. McAdams, W. H., "Heat Transmission", McGraw-Hill, New York, 1954.

22. Penner, S. S., "Quantitative Molecular Spectroscopy and Gas Emissivities", Addison-Wesley, Reading, Mass., 1959.

23. Thompson, W. R., and Geery, E. L., "Heat Transfer to Hydrogen at Super-critical Pressures", Aerojet-General, Report 1842, 1960.

24. Hess, H. L. and Kunz, H. R., "A Study of Forced Convection Heat Transfer of Supercritical Hydrogen", J. Heat Transfer, v. 87 no. 1, 1965, p. 41.

25. McCarthy, J. R. and Wolf, H., "Heat Transfer Characteristics of Gaseous Hydrogen and Helium", Rocketdyne, Report RR 60-12, December 1960.

26. Taylor, M. F., "Local Heat Transfer Measurements for Forced Convection of Hydrogen and Helium at Surface Temperatures to 5600°F", Proc. 1963 Heat Transfer and Fluid Mechanics Institute, 1963.

27. "Design Equation Analysis for Heat Transfer to Cryogenic Hydrogen from 600 to 1500 psia and Wall-to-Bulk Temperature Ratios of 20", Aerojet-General, Report RN-S-0274, Contr. SNP-1, June 1966.

References (cont.)

28. Thompson, W. R. and Geery, E. L., "An Experimental Investigation of Heat Transfer to Cryogenic Hydrogen Flowing Turbulently in Asymmetrically-Heated Straight and Curved Tubes", Aerojet-General, Report TM 183-63-13, Contr. NAS 8-4014, March 1963.

29. Lundin, R. V., "Supercritical Hydrogen Friction Factor Study", Aerojet-General memo 9650:0514, August 1965.

30. Ito, H., "Friction Factors for Turbulent Flow in Curved Pipes", Trans. ASME, J. Basic Engineering, June 1959, pp. 123-124.

31. Vennard, J. K., "Elementary Fluid Mechanics", Wiley, New York, 1954.

32. Goldsmith, A., Waterman, T. E., and Hirschhorn, H. J., "Handbook of Thermophysical Properties of Solid Materials: Vol. 1 - Elements, Macmillan, New York, 1961.

33. "Thermal Properties Handbook", The Boeing Company.

34. Kobayashi, A. C., "Specific Heat and Thermal Conductivity of Materials Commonly Used in Heat Transfer Calculations", Aerojet-General memo 9650:0406, December 1964.

35. "Cryogenic Materials Data Handbook", Air Force Materials Lab. R&D Div., Report ML-TDR-64-280, August 1964.

36. "Investigation of Cooling Problems at High Chamber Pressures: "Final Report", Rocketdyne, Report R-6529, Contr. No. NAS 8-20225, September 1966.

37. Rao, G. V. R., "Exhaust Nozzle for Optimum Thrust", Jet Propulsion - June 1958, pp. 377-382.

38. Sauer, R., "General Characteristics of the Flow Through Nozzles at Near Critical Speeds", NASA Tech. Memorandum #1147.

39. A Digital Computer Program for the Finite Element Analysis of Solids with Non Linear Material Properties, by E. L. Wilson, T.M. No. 23, July 1965, Aerojet.

40. Formulas for Stress and Strains, Roark

41. Stainless Steel Handbook, Allegheny Ludlum Steel Corporation, 1966.

42. MIL-HDBK-5 - 1962.

TRW Systems, Incorporated
1 Space Park
Redondo Beach, California 90200
Attention: STL Tech. Lib. Doc. Acquisitions   1

TRW, Incorporated
TAPCO Division
23555 Euclid Avenue
Cleveland, Ohio 44117
Attention: P. T. Angell   1

United Aircraft Corporation
Corporation Library
400 Main Street
East Hartford, Connecticut 06118
Attention: Dr. David Rix   1

United Aircraft Corporation
Pratt & Whitney Division
Florida Research & Development Center
P. O. Box 2691
West Palm Beach, Florida 33402
Attention: Library   1

United Aircraft Corporation
United Technology Center
P. O. Box 358
Sunnyvale, California 94088
Attention: Librarian   1

Vought Astronautics
Box 5907
Dallas 22, Texas
Attention: Warren C. Trent   1

Camin Laboratories, Inc.
104-14 South Fourth Street
Brooklyn, N. Y. 11211
Attention: S. Fialkoff   1

Rocket Research Corporation
520 South Portland Street
Seattle, Washington 98108   1

Rocketdyne Division of
North American Aviation, Inc.
6633 Canoga Avenue
Canoga Park, California 91304
Attention: Library, Department 596-306   1

Rohm and Haas Company
Redstone Arsenal Research Division
Huntsville, Alabama 35808
Attention: Librarian   1

Space-General Corporation
777 Flower Street
Glendale, California
Attention: C. E. Roth   1

Texaco Experiment, Incorporated
P. O. Box I-T
Richmond, Virginia 23202
Attention: Librarian   1

Thiokol Chemical Corporation
Alpha Division, Huntsville Plant
Huntsville, Alabama 35800
Attention: Technical Director   1

Thiokol Chemical Corporation
Reaction Motors Division
Danville, New Jersey 0/834
Attention: Librarian   1

Thiokol Chemical Corporation
Redstone Division
Huntsville, Alabama
Attention: John Goodloe   1

Lockheed-California Company
10445 Glen Oaks Blvd.
Pacoima, California
Attention: G. D. Brewer   1

Lockheed Propulsion Company
P. O. Box 111
Redlands, California 92374
Attention: Miss Belle Berland, Librarian   1

Lockheed Missiles & Space Company
Propulsion Engineering Division (D.55-11)
1111 Lockheed Way
Sunnyvale, California 94087   1

Marquardt Corporation
16555 Saticoy Street
Box 2013 - South Annex
Van Nuys, California 91404
Attention: Librarian   1

Martin-Marietta Corporation
Martin Division
Baltimore 3, Maryland
Attention: John Calathes (3214)   1

McDonnell Aircraft Corporation
P. O. Box 6101
Lambert Field, Missouri
Attention: R. A. Herzmark   1

North American Aviation, Inc.
Space & Information Systems Division
12214 Lakewood Boulevard
Downey, California 90242
Attention: Technical Information Center,   1
            D/096-722 (AJ01)

Northrop Space Laboratories
1001 East Broadway
Hawthorne, California
Attention: Dr. William Howard   1

Republic Aviation Corporation
Farmingdale, Long Island
New York
Attention: Dr. William O'Donnell   1

Convair Division
General Dynamics Corporation
P. O. Box 1128
San Diego, California 92112
Attention: Mr. W. Fenning   1
          Centaur Resident Project Office

General Electric Company
Re-Entry Systems Department
P. O. Box 8555
Philadelphia, Pennsylvania 19101
Attention: F. E. Schultz   1

General Electric Company
Flight Propulsion Lab. Department
Cincinnati 15, Ohio
Attention: D. Suichu   1

Grumman Aircraft Engineering Corporation
Bethpage, Long Island,
New York
Attention: Joseph Gavin   1

Hercules Powder Company
Allegheny Ballistics Laboratory
P. O. Box 210
Cumberland, Maryland 21501
Attention: Library   1

IIT Research Institute
Technology Center
Chicago, Illinois 60616
Attention: C. K. Hersh, Chemistry Division   1

Kidde Aero-Space Division
Walter Kidde & Company, Inc.
675 Main Street
Belleville 9, New Jersey
Attention: R. J. Hanville   1
          Director of Research Engineering

Lockheed Missiles & Space Company
P. O. Box 504
Sunnyvale, California
Attention: Technical Information Center   1

Beech Aircraft Corporation
Boulder Facility
Box 631
Boulder, Colorado
Attention: J. H. Rodgers   1

Bell Aerosystems, Inc.
Box 1
Buffalo, New York 14205
Attention: Librarian   1

The Boeing Company
Aero Space Division
P. O. Box 3707
Seattle, Washington 98124
Attention: Ruth E. Peerenboom (1190)   1

Chemical Propulsion Information Agency
Applied Physics Laboratory
8621 Georgia Avenue
Silver Spring, Maryland 20910   1

Chrysler Corporation
Space Division
New Orleans, Louisiani
Attention: Librarian   1

Curtiss-Wright Corporation
Wright Aeronautical Division
Woodridge, New Jersey
Attention: G. Kelley   1

Douglas Aircraft Company, Inc.
Santa Monica Division
3000 Ocean Park Blvd.
Santa Monica, California 90405
Attention: J. L. Waisman   1

General Dynamics/Astronautics
P. O. Box 1128
San Diego, California 92112
Attention: Library & Information Services (128-00)   1

Air Force Aero Propulsion Laboratory
Research & Technology Division
Air Force Systems Command
United States Air Force
Wright-Patterson AFB, Ohio 45433
Attention: APRP (C. M. Donaldson)   1

Aerojet-General Corporation
P. O. Box 296
Azusa, California 91703
Attention: Librarian   1

Aerojet-General Corporation
11711 South Woodruff Avenue
Downey, California 90241
Attention: F. M. West, Chief Librarian   1

Aerojet-General Corporation
P. O. Box 1947
Sacramento, California 95809
Attention: Technical Library 2484-2015A   1

Aeronutronic Division of
Philco Corporation
Ford Road
Newport Beach, California 92600
Attention: Technical Information Department   1

Aeroprojects, Incorporated
310 East Rosedale Avenue
West Chester, Pennsylvania 19380
Attention: C. D. McKinney   1

Aerospace Corporation
P. O. Box 95085
Los Angeles, California 90045
Attention: Library-Documents   1

ARO, Incorporated
Arnold Engineering Development Center
Arnold AF Station, Tennessee 37389
Attention: Dr. H. H. Goethert   1
            Chief Scientist

Battelle Memorial Institute
505 King Avenue
Columbus, Ohio 43201
Attention: Report Library, Room 6A   1

Commanding Officer
U. S. Army Research Office (Durham)
Box CM, Duke Station
Durham, North Carolina 27706   1

U. S. Army Missile Command
Redstone Scientific Information Center
Redstone Arsenal, Alabama 35808
Attention: Chief, Document Section   1

Bureau of Naval Weapons
Department of the Navy
Washington, D. C.
Attention: J. Kay, Code RTMS-41   1

Commander
U. S. Naval Missile Center
Point Mugu, California 93041
Attention: Technical Library   1

Commander
U. S. Naval Ordnance Test Station
China Lake, California 93557
Attention: Technical Library   1

Commanding Officer
Office of Naval Research
1030 E. Green Street
Pasadena, California 91101   1

Director (Code 6180)
U. S. Naval Research Laboratory
Washington, D. C. 20390
Attention: H. W. Carhart   1

Picatinny Arsenal
Dover, New Jersey
Attention: I. Forsten, Chief   1
            Liquid Propulsion Laboratory

U. S. Atomic Energy Commission
Technical Information Services
Box 62
Oak Ridge, Tennessee
Attention: A. P. Huber, Code ORGDP   1
            Box P

Office of the Director of Defense Research & Engineering
Washington, D. C.   20301
Attention: Dr. H. W. Schulz, Office of Asst. Dir.   1
             (Chem. Technology)

RTD(RTNP)
Bolling Air Force Base
Washington, D. C.   20332   1

Arnold Engineering Development Center
Air Force Systems Command
Tullahoma, Tennessee   37389
Attention: AEOIM   1

Advanced Research Projects Agency
Washington, D. C.   20525
Attention: D. E. Mock   1

Wright-Patterson Air Force Base
Dayton, Ohio   45433
Attention: AFML (MAAE)   1

Air Force Systems Command (SCLT/Capt. S. W. Bowen)
Andrews Air Force Base
Washington, D. C.   20332   1

Air Force Rocket Propulsion Laboratory (RPRRE)
Edwards, California   93523
Attention: Roy Silver   1

Air Force Rocket Propulsion Laboratory (RPM)
Edwards, California   93523   1

Air Force FTC (FTAT-2)
Edwards Air Force Base, California   93523
Attention: Col. J. M. Silk   1

Air Force Office of Scientific Research
Washington, D. C.   20333
Attention: SREP, Dr. J. F. Masi   ,   1

U. S. Air Force
Washington 25, D. C.
Attention: Col. C. K. Stambaugh, Code AFRST   1

National Aeronautics and Space Administration
Ames Research Center
Moffett Field, California 94035
Attention: Library   1

National Aeronautics and Space Administration
Flight Research Center
P. O. Box 273
Edwards, California 93523
Attention: Library   1

National Aeronautics and Space Administration
Goddard Space Flight Center
Greenbelt, Maryland 20771
Attention: Library   1

National Aeronautics and Space Administration
John F. Kennedy Space Center
Cocoa Beach, Florida 32931
Attention: Library   1

National Aeronautics and Space Administration
Langley Research Center
Langley Station
Hampton, Virginia 23365
Attention: Library   1

National Aeronautics and Space Administration
Manned Spacecraft Center
Houston, Texas 77001
Attention: Library   1
            J. G. Thibodaux   1

National Aeronautics and Space Administration
George C. Marshall Space Flight Center
Huntsville, Alabama 35812
Attention: Library   1
            Keith Chandler, R P&VE-PA   1

Jet Propulsion Laboratory
4800 Oak Grove Drive
Pasadena, California 91103
Attention: Library   1
            Dave Evans   1

DISTRIBUTION LIST FOR INTERIM REPORT NASA CR-72266

"Investigation of Advanced Regenerative Thrust Chamber
Designs"

Contract NAS3-7971

Aerojet-General Corporation
Sacramento, California

COPIES

National Aeronautics and Space Administration
Lewis Research Center
21000 Brookpark Road
Cleveland, Ohio   44135

Attention: Contracting Officer, MS 500-210   1

            Liquid Rocket Technology Branch, MS 500-209   8

            Technical Report Control Office, MS 5-5   1

            Technology Utilization Office, MS 3-16   1

            AFSC Liaison Office, MS 4-1   2

            Library   2

            Office of Reliability & Quality Assurance, MS 500-203 1

            E. W. Conrad, MS 100-1   1
            E. W. Roberts, MS 3-17   1
            D. L. Nored, MS 500-209   1
            E. Richardson   1

National Aeronautics and Space Administration
Washington, D. C.   20546

Attention: Code MT   1
                 RPX   2
                 RPL   2
                 SV   1

Scientific and Technical Information Facility
P. O. Box 33
College Park, Maryland   20740

Attention: NASA Representative   6
            Code CPT